École Polytechnique Fédérale de Lausanne

ENV-599 : Master Project

Influence of bank roughness and bed structure on riverbed morphology

---

4^{th} February, 2022

Autor :

Lionel Pattaroni

Supervisor :

M.Sc. Christian Mörtl

Director :

Dr. Giovanni De Cesare

Acknowledgements

First of all, I would like to thank Dr Giovanni De Cesare for giving me the opportunity to do this Master thesis. My thanks also go to Christian Mörtl for the quality of his guidance, both in terms of his valuable advice and his kindness, throughout the duration of this work. I would also like to thank Jean-Noël Saugy for his valuable help on the numerical model, and more generally the whole LCH platform for the warm welcome I received during this semester. I am deeply grateful to my entire family for their love and support throughout these years of study at EPFL that this work concludes. Finally, I would like to give a special thanks to my friends Corentin, Gabriel, Sarah and Yoann for their unfailing and invaluable support.

Lausanne, February 2022 Lionel Pattaroni

Abstract

In the natural environment, the hydraulic roughness along riverbanks can largely vary between concrete bank reinforcement and dense vegetation. As an integral part of Manning's equation, the influence of roughness on various hydraulic quantities makes it a key parameter in the study of rivers. The presence of a more or less marked roughness will indeed have various implications, in particular with respect to the velocities and heights of water. The following study looks at the influence of bank roughness and bed structure on riverbed morphology. For this purpose, two models will be studied: a physical - representing certain characteristics of a section of the Sarine located downstream of the Rossens dam - and a numerical one. The use of UVP technology will initially allow to both study the impact of roughness on the measured water velocities and heights, as well as the calibration of various parameters of the numerical model. The numerical model will then address the impact of bank roughness and bed structure, in particular on morphologic changes following sediment augmentation, during flood events, and on certain indicators such as the *hydro-morphological index of diversity* (HMID). The results of the study suggest that high roughness coupled with well-defined bed structure create conditions that favour an improvement of the hydro-morphological state of the river after sediment augmentation. Both parameters also play a major role in the dynamics of the watercourse.

Résumé

Dans l'environnement naturel, la rugosité hydraulique le long des berges peut largement varier, entre renforcement des berges en béton et végétation dense. Partie intégrante de l'équation de Manning, l'influence de la rugosité sur diverses grandeurs hydrauliques en fait un paramètre clé dans l'étude des rivières. La présence d'une rugosité plus ou moins marquée aura en effet de multiples implications, notamment au regard des vitesses et hauteurs d'eau. Ce travail s'attelle à étudier l'influence de la rugosité des berges et de la structure du lit sur la morphologie du lit de la rivière. Pour ce faire, deux modèles seront étudiés : un modèle physique - représentant certaines caractéristiques d'un tronçon de la Sarine situé en aval du barrage de Rossens - et un modèle numérique. L'utilisation de la technologie UVP permettra dans un premier temps d'étudier l'impact de la rugosité sur les vitesses et hauteurs d'eau mesurées, mais également de calibrer différents paramètres du modèle numérique. Le modèle numérique se penchera ensuite sur l'impact de la rugosité des berges et de la structure du lit, relativement aux changements morphologiques consécutifs à des apports en sédiments, lors des épisodes de crue, ainsi que sur certains indicateurs tels que l'*indice hydro-morphologique de diversité* (HMID). Les résultats de l'étude suggèrent qu'une rugosité élevée, associée à une structure de lit bien définie, créent des conditions favorisant une amélioration de l'état hydro-morphologique de la rivière suite à l'apport de sédiments. Ces deux paramètres jouent de surcroît un rôle prépondérant dans la dynamique du cours d'eau.

Contents

List of Figures

List of Tables

Nomenclature

Latin symbols

A_c	$[m^2]$	Catchment area of the Sarine
A_p	$[m^2]$	Cross-sectional area - physical model
b	$[m]$	Ideal width of the physical model
B	[m]	Width of the study area
c	$[m/s]$	Sound speed in the medium
d_{90}	$[mm]$	Grain size diameter of which 90 [%] is smaller
d_m	$[mm]$	Mean grain size diameter
f_0	$[Hz]$	Carrier frequency
f_D	$[Hz]$	Doppler frequency
h	$[m]$	Water height - physical model
h'	$[m]$	Projection of water height - physical model
h_1	$[m]$	Sensor height
h_d	$[m]$	Height of the deposits - physical model
H_d	$[m]$	Height of the deposits
J	$[-]$	Longitudinal slope - physical model
J_r	$[-]$	Longitudinal slope of replenishment reach - Sarine
k_{mn}	$[s/m^{\frac{1}{3}}]$	Bank roughness coefficient (Manning) - no roughness
$k_{st,b}$	$[m^{\frac{1}{3}}/s]$	Bank roughness coefficient (Strickler) - no roughness
$k_{st,b}$	$[m^{\frac{1}{3}}/s]$	Banks roughness coefficient (Strickler)
$k_{st,c}$	$[m^{\frac{1}{3}}/s]$	Bed roughness coefficient (Strickler)
$k_{st,s}$	$[m^{\frac{1}{3}}/s]$	Deposits roughness coefficient (Strickler)
$k_{st,bg}$	$[m^{\frac{1}{3}}/s]$	Roughness coefficient (Strickler) - bank with stones and grasses
$k_{st,bl}$	$[m^{\frac{1}{3}}/s]$	Roughness coefficient (Strickler) - bank with less steeply stones
$k_{st,bs}$	$[m^{\frac{1}{3}}/s]$	Roughness coefficient (Strickler) - bank with stones
$k_{st,cb}$	$[m^{\frac{1}{3}}/s]$	Roughness coefficient (Strickler) - breeze blocs
$k_{st,cr}$	$[m^{\frac{1}{3}}/s]$	Roughness coefficient (Strickler) - rough stones
$k_{st,cs}$	$[m^{\frac{1}{3}}/s]$	Roughness coefficient (Strickler) - smooth stones
$k_{st,cs}$	$[m^{\frac{1}{3}}/s]$	Overall roughness coefficient (Strickler)
l	$[m]$	Length of the physical model
l_d	$[m]$	Length of the deposits - physical model
L	$[m]$	Distance of measurement point from upstream - physical model
L_d	$[m]$	Length of the deposits

L_r	$[m]$	Length of the replenishment reach
L_s	$[km]$	Length of the Basse Sarine
L_w	$[km]$	Length of the Sarine
Q_{cr}	$[m^3/s]$	Critical flow rate for shear stress
Q_{flood}	$[L/s]$	Flood flow rate - physical model
Q_m	$[L/s]$	Residual flow rate - physical model
$Q_{r,s}$	$[m^3/s]$	Residual discharge in summer below Rossens dam
$Q_{r,w}$	$[m^3/s]$	Residual discharge in winter below Rossens dam
Q_{shear}	$[L/s]$	Shear stress flow rate - physical model
R_h	$[m]$	Hydraulic radius
u_*	$[m/s]$	Shear velocity
v_m	$[m/s]$	Mean flow velocity
v_p	$[m/s]$	Velocity projection along the transducer axis - physical model
V	$[m/s]$	Flowing velocity along the horizontal axis
V_d	$[m^3]$	Volume of each sediment deposit
V_p	$[m^3]$	Volume of each sediment deposit - physical model
w_c	$[m]$	Width of the physical model
w_d	$[m]$	Width of the deposits - physical model
w_r	$[m]$	Width of the physical model with bank roughness
w'	$[m]$	Distance between two measurement points
W_d	$[m]$	Width of the deposits
W_v	$[-]$	Width variability of the replenishment reach
W_w	$[m]$	Average wetted width of the replenishment reach

Greek symbols

α	[°]	Angle between the transducer and vertical axes
β	[°]	Angle between the transducer and flow axes
γ	$[N/m^3]$	Specific gravity
γ_s	$[N/m^3]$	Specific weight of sediments
Δh	[m]	Depth of immersion of the transducer
μ_h	$[m]$	Average water height
μ_v	$[m/s]$	Average velocity
ρ_q	$[kg/m^3]$	Density of quartz powder
ρ_w	$[kg/m^3]$	Density of water
σ_h	$[m]$	Standard deviation of water height
σ_v	$[m/s]$	Standard deviation of velocity
τ_*	$[-]$	Adimensional shear stress
$\tau_{*,cr}$	$[-]$	Critical adimensional shear stress
τ_{90}	$[N/m^2]$	Shear strenght stress for diameter d_{90}
τ_d	$[N/m^2]$	Shear strenght stress for diameter d_m

1 Introduction

1.1 Literature review

The development of watercourses to meet human needs has played a major role for several centuries. The first trace of a large-scale project in Switzerland dates back to 1714, when the first river correction was carried out to divert the Kander River, which had previously flowed into the Aare and caused numerous floods, into Lake Thun [1] [2]. Although this correction was preceded in the past by the lowering of Lake Zug and the diversion of the Engelberg Aa, the work on the Kander River is now considered to be a pioneer in hydrological projects [3]. For a long time, the development of watercourses was mainly aimed at flood protection and land use, but this changed at the end of the 19th century with the construction of numerous run-of-river power stations and other storage facilities to exploit hydraulic power [4]. However, although the construction of dams makes it possible to meet many other challenges, such as irrigation, water storage or the supply of drinking water [5], numerous studies have highlighted the negative consequences of dam construction on the environment [6] [7].

While large catchment basins may be viewed as ecosystems in which natural and cultural attributes interact, stream regulation reduces many hydrological and biophysical patterns and attributes, impacting notably on native biodiversity and bioproduction [8]. Furthermore, the fragmentation of rivers caused by the creation of artificial lakes and the construction of dams disrupts the flow and sediment transport regime, which can lead to a succession of various pernicious effects [9] [10]. Downstream of the dam, the natural flow regime can in fact be replaced by a constant residual flow, the residual flow being characterised by a low flow coupled with a profound lack of sediment supply [11]. As a result, the emergence of a gradual accumulation of the incoming sediment load from a river - called reservoir sedimentation - with severe consequences for water management, flood control and production of energy [12], with a worldwide loss in reservoir storage capacity reported to be between 0.5 [%] and 1 [%] per year [13].

The lack of sediment downstream of a dam will result in profound morphological and environmental disturbances, degrading the ecomorphological characteristics of the river [14]. This depreciation may be more pronounced in the case of heavily antropised rivers, as well as for coarse gravel rivers [15]. The deficit of sediment will have multiple negative consequences from an ecological point of view, inducing a loss in the aquatic and riparian habitats, with consequences on water quality [16] [17]. The consequences of sediment supply disruption on morphodynamics will include bank erosion, riverbed incision and coarsening of the bed substrate downstream [18] [19], as well as substrate consolidation by onkoid formation [20] or colmation of the riverbed [21] [22]. As a result of all these effects, river morphology and aquatic habitats for fauna and flora have developed towards a less natural state [23].

Sediment management is an important part of river rehabilitation. In the last decades, the replenishment of sediment technique - involving the artificial addition of bedload-sized sediment around the impoundment to the river channel donstream of the dam [24] - has been applied to supply sediment lacking in downstream reaches [11]. Recent studies have contributed to a better understanding of artificial sediment augmentation [25], notably stating that the added material used should be smaller than the existing material [26] [27], thereby enhacing bed elevations variations and favouring the fine sediment availability for the spawning

habitats [28]. Furthermore, laboratory experiments have been performed to asses the erosion process of replenishment deposits [23], as well as the importance of using a specific grain size to increase morphologic variability [29] [30].

Although the dynamics of a river are governed by many parameters, the roughness of the banks and the morphology of the bed also have a major impact [31] [32]. As an integral part of the roughness, riparian vegetation plays different roles in river environments [33]. Firstly, it alters river flow profiles by contributing to the increase in water depth and in the shear stress near the vegetation, coupled with a decrease in velocity [34]. Secondly, it also influences sediment transport pattern, contributing to the deformation of the riverbed [35]. Finally, the structure of the channel is also strongly affected by vegetation, as it reduces the number of active channels by inducing changes in sediment transport and reinforce the channel bank [36].

Riverbed structure usually form in high flow, before being exposed on the bed surface once the low flow has removed fine sediments [37] [38]. The measured riverbed structure intensity hence reflects an equilibrium state among bedload transport, incoming sediment and flow condition [39]. The structure of the riverbed will have an impact on its flow, with a much greater complexity in the presence of a meandering versus a straight course [40]. As migrating bed forms influence the velocity structure, the structure will be subject to variations depending on the complexity considered [41]. Slope also has a strong influence, in particular due to its importance in how quickly a drainage channel will convey water [42]. This is particularly the case during flood events, where watersheds with steep slopes will rapidly convey incoming rainfall - resulting in a peak flow occurring shortly after the onset precipitation -, while watershed with a flat slope will not be as quick [43] [44].

1.2 Research gap

A study [11] was carried out in 2016 on a section of the Sarine located downstream of the Rossens dam in Switzerland. As a prelude to this study [45], a special configuration - optimised in the laboratory - of four sediment replenishment depots was applied, followed by the passage of an artificial flood with a return period of four years. The analysis then focused on the morphological evolution of the riverbed reconstruction downstream, including the topography before and after the flood. For this purpose, HMID was used to assess the quality of the riparian habitats in the analysed section.

While the study reached a number of conclusions, including that the combination of an artificial flood and sediment replenishment is a robust measure for supplying sediment to rivers and improving sediment dynamics, it allowed only one scenario to be studied. Several result gaps remain, related to the large-scale replication on multiple configurations. These include the response of the river in the case of multiple replenishment of sediments, the influence of a more or less pronounced roughness on the banks on the results obtained, and the consequences on the transit of a flood on various morphology.

1.3 Research questions

This Master thesis aims to examine the influence of bank roughness and bed structure on riverbed morphology studying two models, one physical and one numerical. For this purpose, water velocities will first be measured using UVP technology on a physical model. These measurements will be carried out in two stages : in the absence of added bank roughness and after the artificial addition of a geonet on the banks. The comparison of velocity profiles will allow to observe the first effects caused by a more pronounced bank roughness. The results obtained will then be used to calibrate various parameters required for the numerical model. Using the *digital elevation model* (DEM) obtained from the laboratory scanners, various hydraulic simulations will then be able to be carried out using the *Basement* software. This will allow the simulation of various output parameters for a wide range of different input configurations. With the help of the results obtained, this study will finally aims to reply to the three following research questions :

1. What is the impact scale of bank roughness and longitudinal bed structure on morphologic changes (erosion and deposition) in the context of sediment augmentation ?
2. What are the consequences of variable bank roughness and bed structure during flood events on flood transit ?
3. To what extent do different augmentation measures increase hydro-morphological diversity ?

2 Theoretical background

2.1 Bank roughness

Bank roughness considerably vary in natural rivers. The evolution of the vegetation on the banks plays a key role in this variation. For example, the presence of individual shrubs with leaves will offer less resistance to flow than if they were leafless. This property is due to the ability of the leaves to simplify the flow and bend as the water passes. Similarly, summer vegetation will generally have a higher roughness. Bank roughness can thus take on a wide range of values, from 100 when the banks are very smooth to less than 10 when there is a lot of brush and other obstructions to the flow of water [46].

The evolution of bank roughness has multiple consequences on the dynamics of the river. In particular, it influences the sediment transport pattern and the channel structure, reducing the number of active channels. The presence of very pronounced vegetation will also contribute to the strengthening and stabilisation of the banks [33]. Roughness will also influence measurements of flow velocity and water-surface topography. Because of the effect of bank roughness on the transverse boundary layer, its influence will be particularly pronounced with respect to position of high-velocity core and secondary current strength. Indeed, with a low bank roughness, surface flows approach the outer bank more directly, strengthening the secondary current and enhancing superelevation on the outside bank. On the other side, added roughness tends to produce backwater effects, reducing the approach of outwardly directed surface flow to the outer bank [47].

2.2 Bed structures

Riverbed structures were developed in many very coarse gravel-bed rivers as a result of fluvial morphology [48]. In natural streams, riverbed configurations are shaped by varying flow. This is especially the case on coarse-grained riverbed, where the particles can be moved to certain locations to create structured bed forms [49]. Streambed structures plays two major roles, namely preventing streambed erosion and armouring the riverbed. These structures will also help to reduce the forces acting on the particles, creating multiple clusters that require higher shear stress than the isolated particles to be set in motion. A study [50] highlighted the joint evolution of the slope of a channel with the size of streambed structures. As larger streambed structures usually occur in higher gradient channel, they help protecting the riverbed and sustaining a sharper slope. Moreover, it was also stated that geomorphologies composed of more incisive features will generally promote the development of larger streambed structures.

This joint with the evolution of the slope can be explained by the potential for dissipation of erosive energy by larger streambed structures. Each channel is assigned a stream power, corresponding to a measure of its energy, including that which is related to the ability to transport sediment. If the streambed structures fail to consume all the erosive stream power, the stability of the river will no longer be guaranteed, and the excessive power will scour the bed [50]. Hence, as the long-term adjustment of riverbed and flow approaches equilibrium, riverbed adaptation to scouring results in the development of defined streambed structures.

2.3 Bedload transport processes in gravel bed rivers

A shear stress is a mechanical stress applied tangentially to a face of a material. It develops on each fluid particle when the fluid moves over a fixed surface from the walls or the bottom, due to the velocity gradient that is established within the fluid [51] [52]. A shear stress also applies to any object or particle in the flow, conditioning the solid transport. Bank erosion and bedload transport processes occurs as soon as the shear stress exceeds a reference value, called critical shear stress [53] [54]. This will occur when the flow velocity becomes greater than the shear velocity, allowing the mobilising forces acting on the particles to override stabilising forces exerted by other sediments in contact with the particle [55]. The Yalin-Shields diagram makes it possible to quantify the value of the adimensional critical frictional tension as a function of an adimensional particle diameter [56], making it possible to determine the minimum diameter required by a particle to be set in motion.

Once set in motion, the transport of particles in a river can be divided into three main categories, namely solution transport, suspension transport and bedload transport. The distinction between suspension and bedload transport depends not only on the density and size of the particles, but also on the flow structure. Thus, while the flow velocity required to mobilise the grains increases with their granulometry in the case of medium to coarse particles, fine particles also require a high flow velocity in order to be mobilised, as a consequence of the high cohesive force existing between the finest particles [57] [58]. The behaviour of particles as a function of size and flow velocity is governed by the Hjulström diagram [59].

The dimensionless shear stress allowing the movement of all grains of diameter less than or equal to d is expressed in one of the following two forms :

$$\tau_* = \frac{\rho_w u_*^2}{(\gamma_s - \gamma) \cdot d} \tag{1}$$

$$\tau_* = \frac{\gamma R_h J_f}{(\gamma_s - \gamma) \cdot d} \tag{2}$$

$\rho_w = 1000\ [kg/m^3]$ is the density of water, u_* [m/s] is the shear velocity, $\gamma_s = 26'500\ [N/m^3]$ is the specific weight of the sediments [60], $\gamma = 10'000\ [N/m^3]$ is the specific gravity, R_h [m] is the hydraulic radius and J [-] is the longitudinal slope of the riverbed. Considering the Shields diagram, a critical adimensional shear stress $\tau_{*,cr} = 0.047$ allows the particles to move. By isolating the hydraulic radius R_h in *equation (2)* and assuming $\tau_* = \tau_{*,cr} = 0.047$, it is possible to determine the critical hydraulic radius allowing the setting in motion of grains of diameter d_m and d_{90} for a considered slope J. Once the hydraulic radius has been obtained, the corresponding flow rate Q_{cr} can be determined using the *Manning-Strickler equation for a uniform flow (3)*, where k_{st} corresponds to the bed roughness according to Strickler $[m^{\frac{1}{3}}/s]$, A is the cross-sectional area $[m^2]$, and the other variables are defined as above :

$$Q = k_{st} \cdot A \cdot R_h^{\frac{2}{3}} \cdot J^{\frac{1}{2}} \tag{3}$$

Finally, the shear strength stress τ $[N/m^2]$ for sediment transport of diameter d is calculated according to *equation (4)*, where the different variables are defined as above. When this critical shear strength is exceeded, the stripping of particles with a diameter of up to d can begin.

$$\tau = \tau_{*,cr} \cdot (\gamma_s - \gamma) \cdot d \tag{4}$$

2.4 Ecomorphological assessment strategies

The *Hydro-Morphological Index of Diversity* (HMID) is a tool developed by Walter Gostner, allowing a quantitative statement of habitat heterogeneity enhancement for different project alternatives. It therefore advises which alternatives to prioritize from an ecomorphological perspective [61]. This tool can be used on a range of Swiss rivers [62] [63]. This range includes gravel-bearing alpine rivers, whose reference state may be a wandering, braided or meandering river. As this category of rivers is very common in the Alps, this index has a wide range of applications [61]. The HMID allows a quantitative assessment of the improvement of morphological diversity in the context of water management projects. However, if its calculation gives an idea of the ecological potential for river revitalisation projects, it does not provide an index of habitat quality and biodiversity. This can be done for example by means of the so-called *Rapid Bioassessment Protocols* (RBP), a method based on visual and qualitative criteria such as sediment deposition [64], bank stability and protection, frequency of riffles or width of the vegetation corridor. Although they differ somewhat, the HMID and RBP techniques are still very similar, as evidenced by the correlation of more than 90 [%] obtained when comparing these two methods [65].

To develop the HMID tool, a vast investigation campaign was carried out along several Swiss rivers that are more or less dammed up. This campaign made it possible to highlight two necessary findings for the development of this index [62] [66] :

1. The morphological diversity of a river section can be characterised by the hydraulic values of depth and velocity and their statistical parameters.
2. By combining the statistical parameters of the hydraulic values into one variable, the HMID, it is possible to characterise the morphological diversity of the semi-aquatic and aquatic habitats of a river section.

Although only considering the hydraulic variables water depth and velocity avoids the need for complex hydraulic calculations, these two variables are nonetheless closely linked to other morphological parameters - quality and diversity of the substrate, diversity of the thalweg or diversity of the cross-sections - and hydraulic parameters - Reynolds number, Froude number or shear stress - of the river [64] [65]. The calculation of the HMID is based on the coefficient of variation CV of the different variables. This coefficient corresponds to the ratio of the standard deviation σ of the variable, describing its diversity, to its mean μ, acting as a weighting [61]. By proceeding in this way, the diversity *V(i)* of a hydraulic variable is obtained using *equation (5)* [67] [68] :

$$V(i) = (1 + CV_i)^2 = (1 + \frac{\sigma_i}{\mu_i})^2 \tag{5}$$

To calculate the HMID of a section, the partial diversities of velocity and water height must be multiplied. The equation for the calculation of this index is finally expressed as :

$$HMID = \prod_i V(i) = V(v) \cdot V(h) = (1 + \frac{\sigma_v}{\mu_v})^2 \cdot (1 + \frac{\sigma_h}{\mu_h})^2 \tag{6}$$

σ_v [m/s] is the standard deviation of velocity, μ_v [m/s] is the average of velocity, σ_h [m] is the standard deviation of water height and μ_h [m] is the average of water height. As its calculation is based on averages and standard deviations of water velocities and depths, it makes it varying considerably depending on the structure of the riverbed and the roughness considered [67] [68]. The resulting HMID value is used to classify the river into one of three categories : *channelized*, *partially channelized* or *natural*. A description of these categories is presented below [64] :

1. **Channelized river** ($HMID < 5$) : Morphologically heavily altered sites with uniform cross-sections and longitudinal slopes. An HMID close to five corresponds to a channelized river with minor geomorphic patches as, for example, a thalweg line continuously shifting between the two bank toes.
2. **Partially channelized river** ($5 < HMID < 9$) : Stream sites at the lower end of this range are still showing a limited variability of hydraulic units. Hydromorphological patches typical to intact natural state are not developed yet. At the upper end of this range, sites are approaching natural morphology.
3. **Natural river** ($HMID > 9$) : Morphologically unregulated sites where gravel bed streams fully develop their spatial dynamics, showing the complete range of hydraulic habitats. For river engineering projects, these sites could be classified as reference sites.

3 Project baseline data

3.1 Location

With a length $L_w = 126$ [km] and a catchment area $A_c = 1,892$ $[km^2]$, the Sarine is a Swiss river whose watercourse is mainly located in the canton of Fribourg [69]. Tributary of the Aare and part of the Rhine catchment area, the Sarine rises at the Sanetsch Pass in the commune of Savièse in the Valais, before flowing north towards Gstaad and then west into the Pays d'Enhaut. Once it reaches the Lac de Gruyère, it is fed by the Jogne and Trême rivers and flows to Fribourg and the artificial lake of Schiffenen, before finally flowing into the Aare near Golaten.

The Basse Sarine is a bedrock alluvial river with exposed molasse rock [45] of length $L_s = 28.3$ [km], linking the Rossens dam - completed in 1948 - and the Schiffenen dam - built in 1963 - [70] [71]. It is within this section that the study segment is located. Protected since 1992 and listed as an alluvial zone of national importance [72], the portion is only slightly affected by direct human activity, due to the difficulty of accessing it. Despite this, the morphology of the watercourse has nevertheless been heavily impacted by the Rossens dam upstream, which releases residual flows of $Q_{r,w} = 2.5$ $[m^3/s]$ in winter and $Q_{r,s} = 3.5$ $[m^3/s]$ in summer [73].

The study area is located near the village of Posieux. The replenishment reach, with a length $L_r = 200$ [m], is divided into an intervention section - defined as the upstream 80 [m] long section of the replenishment reach -, followed by a 120 [m] long downstream section. Subsequent to a bend, the planform is straight and consists of alternating riffles, pools and runs, with long rapids section [74]. The average wetted width is $W_w = 24.9$ [m], and the width variability - the ratio of the maximum width to the minimum width - is $W_v = \frac{33.8[m]}{14.9[m]} = 2.3$. The slope has a gradient of $J_r = \frac{0.7[m]}{200[m]} = 0.003$. *Figure 3.1* presents the study section, with the four sediment deposits explicitly highlighted.

FIGURE 3.1 – Study area, where the yellow rectangles correspond to the sediment deposits.

3.2 Hydro-morphological impact of the Rossens dam

The construction of the Rossens dam in 1948 gradually led to a profound modification of both sedimentological and hydrological regimes, which has continued to transform the bed of the Basse Sarine ever since. These morphological disturbances, which have been carried out progressively over the decades, have gradually transformed the 1948 low-flow channel into the present one, with the development of abundant vegetation on the banks [65]. This drop in water level can be explained by the fact that a significant part of the water is now diverted from the channel and conveyed to the hydroelectric power station via a penstock. The section of the river bypassed by the penstock, known as the *residual flow reach* [75], is characterised by a disturbed sediment regime and an abnormally stable low flow regime that does not allow for the generation of solid transport [76]. This observation is reinforced for the Rossens dam, as *Group E* set up a flood forecasting system in 1973 to reduce the level of the Lac de Gruyère, to benefit from its retention basin effect [65]. As a consequence, the flows generated by the floods on the Basse Sarine section are not sufficiently high.

In addition to drastically reduce the downstream flow, the dam also plays a major role in retaining sediments, resulting in a progressive incision from upstream to downstream of the river located downstream of the dam [77]. In fact, despite the large amount of sediment present on this section, the virtual absence of sediment transport prevents their mobilisation and leads to the formation of alluvial banks on which abundant vegetation will then be free to develop. Finally, the imposition of an artificial hydro-morphological regime results in a drastic reduction of environmental disturbances and morphodynamics, leading to an ecomorphological degradation of the habitat palette [78]. The consequences of such degradation are numerous, including the consolidation of the substrate by the formation of oncoids [20] - organisms consisting of a layered micritic cortex and a bio- or lithoclastic nucleus, enhancing and initiating the precipitation of calcium carbonate -, or the formation of armouring layers in the riverbed [75].

Several experiments were carried out to revitalise the watercourse and to renaturalise the Basse Sarine, trying to increase the width of the channel and the morphological variability of the section. To this end, four sediment deposits from the alluvial forest were placed in a section of the Basse Sarine. Once the placement was completed, two artificial floods were triggered, the first on September 14^{th} and 15^{th}, 2016 and the second on October 22^{th}, 2020, to allow the transport and remobilisation of part of these sediments. These artificial floods were unexpectedly supplemented by a naturally occurring flood event in July 2021.

3.3 Morphological changes in the Basse Sarine

To determine to what extent the construction and operation of the Rossens dam have impacted the morphology of the Sarine, it is advisable to study and compare several orthophotos of the section, each corresponding to a different temporal period. *Figure 3.2* presents the orthophotos of 1929 (top left), 1974 (top right), 1993 (bottom left) and 2013 (bottom right).

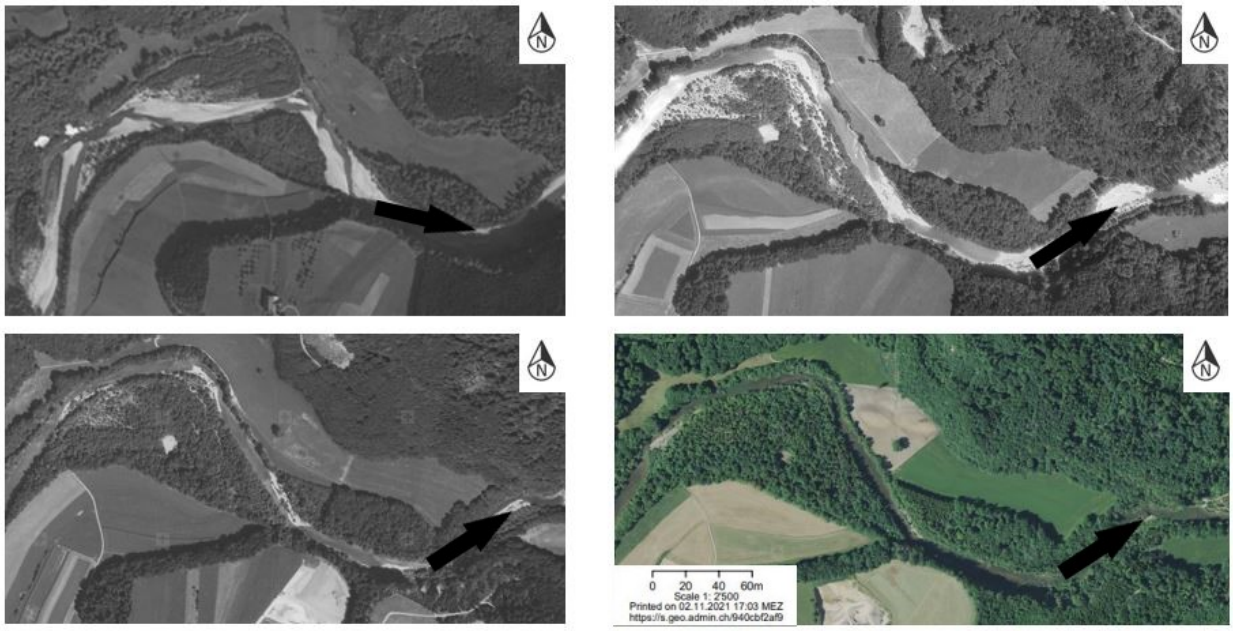

FIGURE 3.2 – Orthophotos of the study area corresponding to years 1929 (top left), 1974 (top right), 1993 (bottom left) and 2013 (bottom right).

The study of the orthophoto corresponding to the situation in 1929 highlights the meandering formation of the river, with wide alternating gravel banks. At that time, prior to the construction of the dam, the study section had relatively little vegetation on its banks, with large gravel banks typical of deposits. The orthophoto of 1974 clearly illustrates the modifications induced by the construction of the Rossens dam thirty years earlier : a vertical erosion of the riverbed caused by the widening of the river. Furthermore, it can be seen that the channel carrying the low water flows at that time corresponds to the channel that currently exists between the vegetation zones. The width of the gravel banks is much greater after the construction of the dam, however decreasing as the concentration of the flow in the main section allows the development of more and more vegetation on the gravel banks. This development is all the more detrimental, as the presence of vegetation will concentrate the flow in the main section during floods, increasing vertical erosion even more.

This fact can be seen even more clearly on the orthophoto of 1993. The gravel banks are becoming less and less visible, sign of the increasing presence of vegetation such as pioneer plant colonies or hardwood and softwood alluvial forests. The course of the river continues to narrow, becoming even more concentrated in its main section. The 2013 orthophoto corresponds almost exactly to the current situation of the section. The inexorable reduction in the width of the watercourse now gives it a more channelized profile than it had in the past, with the flow exclusively centralised in the main section. As a consequence of this lack of flow dynamics, the morphology of the bed is becoming increasingly monotonous. Another proof of this is the absence of morphological modification at the scale of the Sarine, since the watercourse still has a meandering structure. It highlights that the role played by the vegetation during flood events - i.e. concentrating the flow in the main channel - no longer allows flood events to modify the structure of the river. *Figure 3.3* illustrates the above findings, highlighting the evolution of the habitat type of the section of interest.

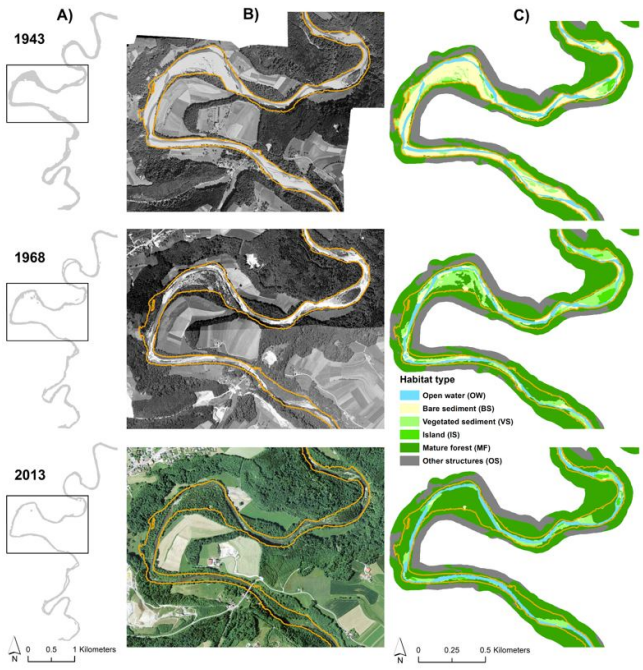

FIGURE 3.3 – Evolution of morphological changes of the study area corresponding to years 1943 (top), 1968 (middle) and 2013 (bottom) [79].

3.4 Sediment supply

To study the effect of a sediment augmentation on the hydro-morphological diversity of the downstream reach, a strategy of replenishing the sediments present under the vegetation has been implemented. This strategy is part of a mitigation measure against the negative effects of the lack of sediment. To this end, a so-called *direct* recharge operation [80] was carried out. The deposits were placed in such a way to create morphological structures such as shoals or sediment banks in ecologically appropriate locations. In the Basse Sarine, four sediment deposits from the alluvial forests on the orographic right side of the river, each with a volume $V_d = 250$ $[m^3]$, were placed in the study section prior to the artificial floods of 2016 and 2020 [45], nine kilometers downstream of the Rossens dam.

The replenishment material had the same characteristic diameters as the riverbed, namely $d_m = 57$ [mm] and $d_{90} = 113$ [mm], distribution obtained using photo sieving and line-sampling [45]. If sediments were not sorted or washed before entering the river, the finest were then washed away by a large extent during installation. The four deposits had a well-defined geometry, with a height $H_d = 1.5$ [m], a width $W_d = 7.5$ [m] and a length $L_d = 22$ [m], totalling no less than 1000 $[m^3]$ of remobilised sediment [65]. This value is however still well below the recommended volumes. To reactivate the alluvial dynamics over a long section and not only over a limited portion downstream of the dam, a regular annual recharge of at least 3000 $[m^3]$ would be required [81], or else the corresponding multiple at more widely spaced intervals. *Figure 3.4* illustrates the installation of sediment deposits using a mechanical shovel, prior to the 2016 artificial flood.

FIGURE 3.4 – Installation of sediment deposits in 2016.

To determine the most suitable geometric arrangement of the four sediment deposits, six different configurations were tested in the laboratory [82]. These tests highlighted that while a parallel configuration produces a larger spread of the eroded material on the entire channel bed, this geometry does not favour the formation of clear defined bed-forms along the channel bed. On the other hand, an alternating configuration increases the complexity of the riverbed morphology, recreating a natural sediment transport along the disturbed reach. The alternating geometry was chosen in the case of the Basse Sarine as it allows for a periodic depositional development, leading to morphological changes of the bed with periodic deposition in the longitudinal direction.

Figure 3.5 presents the chosen deposit configuration. Deposits I and III are located on the left bank, separated from each other by a distance L_d corresponding to the length of one deposit. Deposits II and IV are located on the right bank of the river, each offset by half the length $\frac{L_d}{2}$ of one deposit. Set up in this way, the deposits occupy about two thirds of the total width B of the river. This deposition in clusters is more valuable for in-stream organisms than a homogeneous uniform distribution, as it allows the creation of suitable habitats for aquatic fauna.

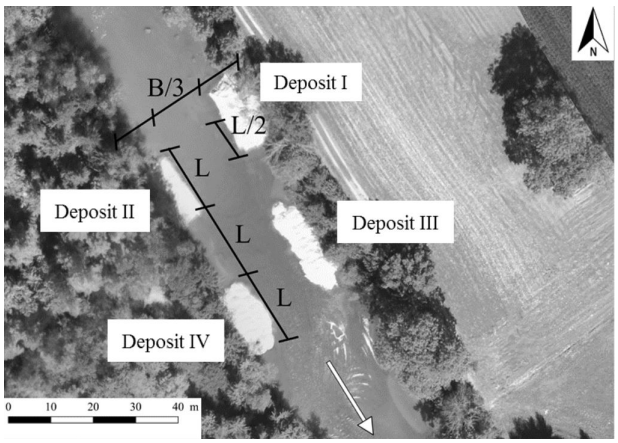

FIGURE 3.5 – Geometric arrangement of the deposits, where L corresponds to the length of one deposit and B to the width of the Sarine [45].

3.5 Bedload transport

Bedloading is the motion of sediments under the influence of water. During a flood event, the materials carried from upstream ensure the renewal of the substrate and gravel banks, replacing those carried away by erosion. Bedload is an important component of the natural river, as it is the main driver of a dynamic river morphology. This dynamic river morphology allows the river to reach a state of equilibrium and to develop its own morphology. By regulating the river bottom, bedload contributes to the proper functioning of the alluvial zones. While bedload is one of the key elements guaranteeing good river morphology, more and more rivers now have a greatly altered solid transport, with respect to their natural state. Biodiversity being closely linked to river dynamics, it results in a profound dysfunction of the aquatic and riparian ecosystems of these rivers. Indeed, an insufficient supply of solids carried from upstream will cause the riverbed to lose its piles of loose gravel, resulting in progressive clogging over the long term.

The section of the Sarine between Rossens and Fribourg is particularly affected by this reduction in bedload, since a report published in 2019 by the FOEN [83] classified it as *severely disturbed or with a deficit of 81 to 100* [%]. This finding echoes the conclusions drawn earlier in *Section 3.3*. Furthermore, a study [81] carried out on the evolution of the transported mass as a function of distance highlighted the impact of the construction of the Rossens dam on the retention of sediments and on the associated bedload reduction : in the sequence of the construction of the dam, high flows caused by spillways contributed to increase erosion of the riverbed due to lack of available sediment. As a result of this increased erosion, the first morphological changes were recorded on the Sarine, including the retreat of the river channel shown at the top right of *Figure 3.2*. From 1973 onwards, the objectives of improving flood control and hydroelectric production contributed to the optimisation of the spillway, favouring both apparition and development of substantial vegetation on the secondary arms and gravel banks. This is illustrated in the bottom left of *Figure 3.2*, where the flow becomes increasingly concentrated in a narrow channel. Nowadays, although a return to a fully natural state appears to be compromise in the case of the Basse Sarine, several measures to restore the bedload regime are both desirable and feasible, making it possible to come back to a more natural morphological state and to limit the lasting damage to the river dynamics.

4 Physical Model

4.1 Experimental setup

4.1.1 Model setups

To be able to carry out a wide range of experiments, an existing morphological channel representing certain characteristics of the study section of the Sarine was used. With a length $l = 34.3$ [m], the initial width of the channel is $w_c = 0.55$ [m], which is reduced to $w_r = 0.52$ [m] once the roughening foam is installed. While the slope of the Sarine $J_r = 0.003$ is assumed to be constant over the section of interest, the slope of the physical model varies, with both ascending and descending sections taking into account the topographical characteristics of the Sarine. *Figure 4.1* presents a longitudinal profile of the section without bank roughness, where the yellow triangles illustrate the *ultrasonic sensors* (USS) and the red rectangles represents the sediment deposits, both of which will be discussed later. *Appendix A.1* presents the longitudinal profile with bank roughness.

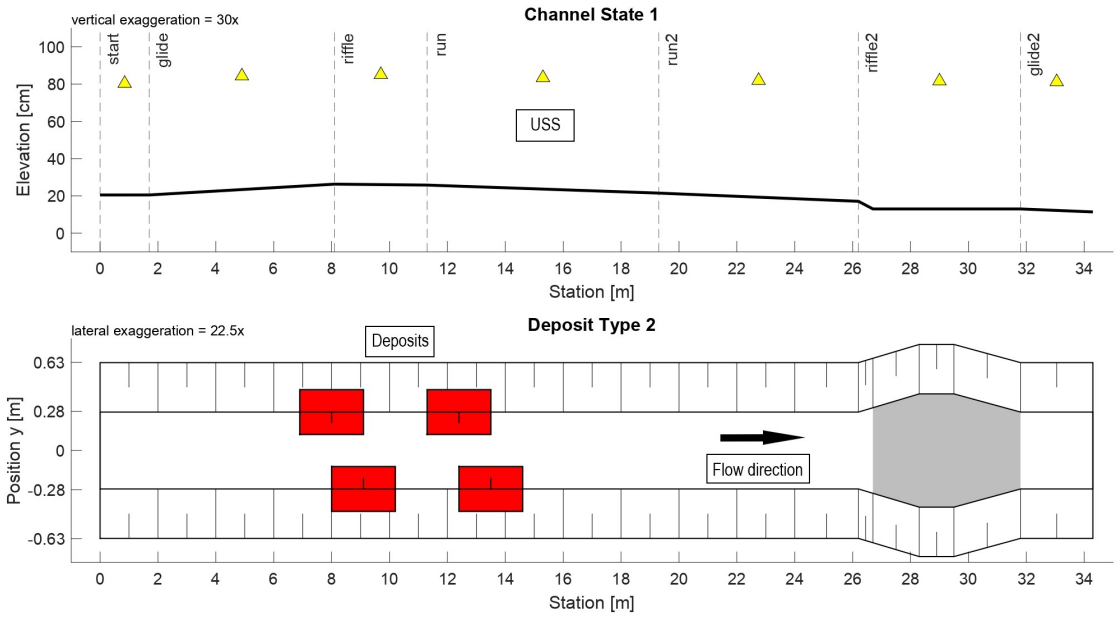

FIGURE 4.1 – Schema of the morphological channel without bank roughness. The longitudinal profile of the morphological channel is presented at the top, where yellow triangles corresponds to the USS. A top view of the channel is presented at the bottom, where the red rectangles corresponds to the sediment deposits. The black arrow shows the flow direction.

As illustrated in *Figure 4.1* (top), the physical model is composed of seven distinct sections. Their main features are described in *Table 4.1*, while information related to the variations of the riverbed along the channel are detailed in *Appendix A.2*. The banks are made of smooth wood, so that their initial roughness is almost negligible, with an average angle of 45 [°] with respect to the riverbed. The riverbed is made of concrete, encrusted with small gravels to increase its roughness. *Figure 4.2* presents an illustration of the *run* section of the channel (left) and of the *run2* and *riffle2* sections (right).

Part	Name	Length [m]	Slope under USS [%]
1	-	1.7	0
2	Glide	6.4	0.91
3	Riffle	3.2	-0.16
4	Run	8	-0.54
5	Run2	6.9	-0.64
6	Riffle2	5.6	0
7	Glide2	2.5	-0.64

TABLE 4.1 – Characteristics of the different sections of the physical model.

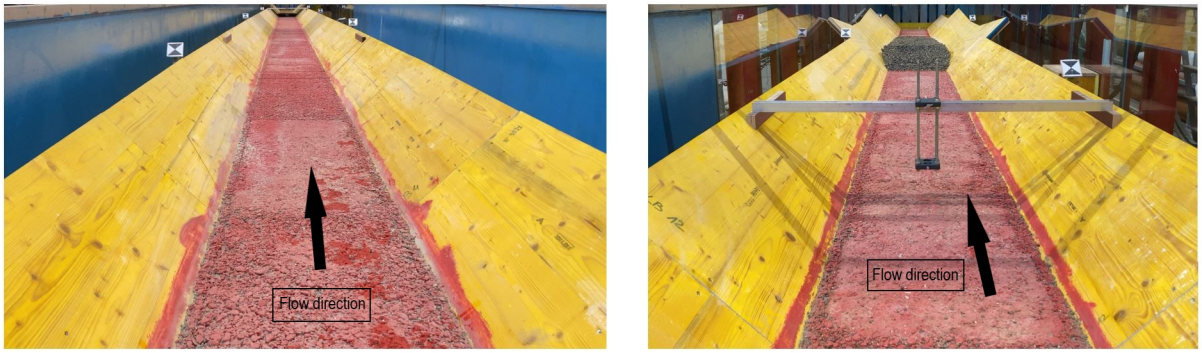

FIGURE 4.2 – *Run* section of the empty channel (left) and *run2* and *riffle2* sections of the empty channel, with the system for UVP measurements (right). Both pictures are taken in the downstream direction. The black arrow shows the flow direction.

The four sediment deposits follow an alternating geometry [82], each with a length $l_d = 2$ [m], a width $w_d = 0.18$ [m] and a height $h_d = 0.16$ [m]. Their exact location is shown in *Figure 4.1* and follows the spacing suggested in *Figure 3.5*, i.e. an offset $\frac{l_d}{2}$ between two deposits and a spacing l_d between two deposits located on the same bank. Each deposit corresponds to a volume $V_p = 0.058$ $[m^3]$, composed of coarse grain of a size ranging from 4 [mm] to 8 [mm]. *Figure 4.3* illustrates the arrangement of the four deposits, prior to an experiment.

FIGURE 4.3 – Arrangement of the four sediment deposits prior to an experiment in the alternating configuration. The picture is taken in the upstream direction. The black arrow shows the flow direction.

4.1.2 UVP

4.1.2.1 Functioning of a UVP

Ultrasonic Velocity Profile (UVP) is a method to obtain instantaneous velocity profiles of a fluid along a measurement line, using ultrasound and signal processing techniques [84]. This method combines detection of the instantaneous Doppler shift frequency, together with pulsed ultrasonic echography [85]. It has many advantages over other means of velocity measurement, including being non-invasive, non-intrusive, and applicable to opaque liquids. Furthermore, this method provides a record of the spatiotemporal velocity field, as well as an efficient flow mapping process [86]. The operation of the UVP technology is described below.

Consider a coordinate system (x,z), where x is the component in the main flow direction and z the component orthogonal to the main flow direction [87]. The technology is based on the use of a transducer oriented at a free angle to the flow axis. The transducer emits a short series of ultrasonic pulses into the liquid, consisting in several periods at the emission frequency within the bandwidth of the selected transducer. As ultrasonic waves concede a part of their energy to the medium by absorption and scattering while propagating, a physical limit to the depth of the exploration is induced by the decrease of the acoustic beam in density. To measure velocities using an ultrasonic wave, the presence of acoustic scatterers - micro-bubbles or particles - in suspension in the fluid is required. Once the ultrasonic pulse has been transmitted, these scatterers dispersed all along de flow will produce a continuous backscattered signal from the medium. Instantaneous profiles can finally be obtained by analysing the so-called backscattered signal. Moreover, to ensure this technology works properly, all echoes must be returned before the next pulse is sent. Using all this information, the projection of the velocity v_p [m/s] along the transducer axis can be obtained according to *equation (7)*, where c [m/s]

is the sound speed in the medium, f_D [Hz] is the Doppler frequency and f_0 [Hz] is the carrier frequency, in other words the frequency of a carrier wave that is modulated to transmit signals [88] :

$$v_p = \frac{c}{2} \cdot \frac{f_D}{f_0} \tag{7}$$

Once the projection of the velocity v_p has been obtained, the flowing velocity V [m/s] along the horizontal axis can finally be calculated as a function of the angle β [°] between the measurement axis and the flow axis. For this purpose, the *trigonometric relation (8)* is used - recall that it is the vector V that is first projected onto the measurement axis to obtain the vector v_p - :

$$cos(\beta) = \frac{v_p}{V} \leftrightarrow V = \frac{v_p}{cos(\beta)} \tag{8}$$

To justify the validity of this result, *Figure 4.4* illustrates the velocity measurement principle. By convention, it has been determined that the velocity is positive when the water flows towards the transducer, and negative when it flows away from it. Finally, it should also be mentioned that although this velocity measurement technique offers high accuracy and very good spatial resolution, the technique is only guaranteed for a given velocity range. Indeed, when the interval between two successive pulses is too large, the limit given by the Nyquist-Shannon theorem - which states that sampling a signal requires a number of samples per unit time greater than twice the difference between the minimum and maximum frequencies it contains [89] - is overstepped, resulting in a velocity jump.

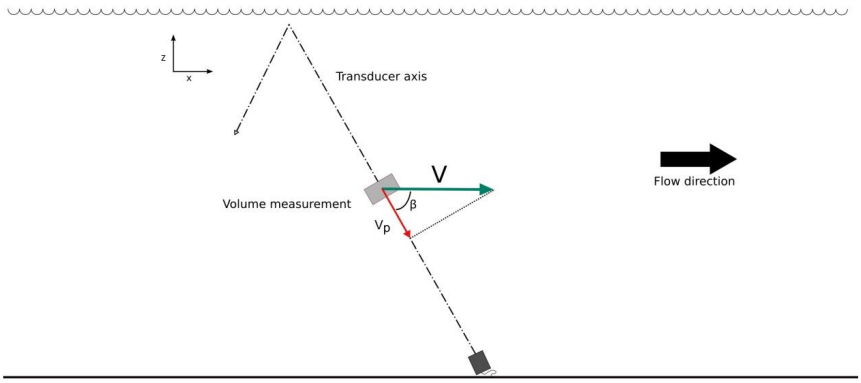

FIGURE 4.4 – Velocity measurement principle, where v_p corresponds to the projection of the velocity in the axis of the transducer, V is the flowing velocity along the horizontal axis x, and β is the angle between the transducer axis and the horizontal flow axis [87].

4.1.2.2 Hydrolysis for UVP tracer analysis

To measure water velocity using UVP technology, it is imperative that the water contains foreign elements, such as tracers, allowing the reflection of the ultrasonic wave. These can be fine elements, such as powder or sand, but with the disadvantage of polluting the water in the main pool. An alternative solution is to generate air bubbles, by means of an electrolysis system. This second method was tested for this study.

Water electrolysis is an electrolytic process in which an electric current is used to break down a water molecule H_2O into dihydrogen gas and oxygen [90]. To this end, two rods of a generally inert metal are immersed in water, powered by an electrical circuit. The first electrode allows electricity flowing through the circuit to reach the water, while the second electrode is used by electricity to leave the water. When electricity comes into contact with the water it disturbs the molecules, breaking the bond and releasing a hydrogen from the rest of the molecule. The appearance of electrically charged particles - called electrons - on the cathode will cause the water molecules to fracture and the hydrogen atoms to break away [91]. Once isolated, the atoms then regroup to form dihydrogen. Conversely, the molecules near the anode will also have their bonds destroyed due to the attraction of electrons by the anode [92]. This reaction also produces a gas, namely the oxygen we breathe. *Figure 4.5* illustrates the process of electrolysis.

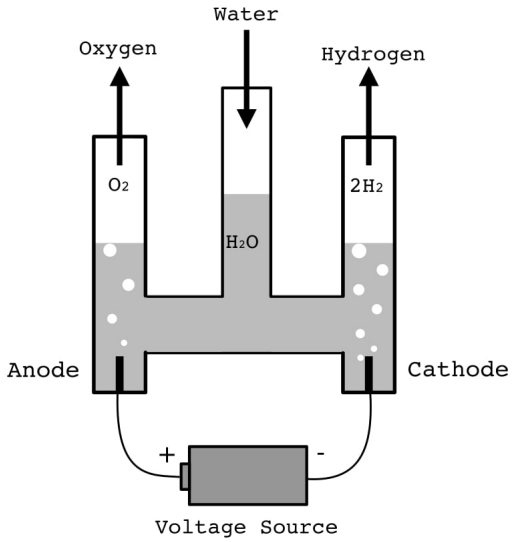

FIGURE 4.5 – Water electrolysis process [93].

The construction used to generate the air bubbles consists of a tension source, four stainless steel threaded bars and a stainless steel wire. The wire is wound in turn around two pairs of two threaded rods, forming two grids. Although the grids are each connected to a voltage pole, there is no wire connecting them to each other. The connection between the two grids is made by water, which is electrolyzed when a voltage is applied. Once completed, the construction was installed upstream of the channel, screwed to a fixed wooden structure to ensure stability. *Figure 4.6* presents the final result (left), while the drawings required to manufacture the various parts of the system are detailed in *Appendix A.3*.

FIGURE 4.6 – Fixed (left) and mobile (right) apparatuses used to perform water hydrolysis. The fixed is located at the top of the channel, while the mobile is located in the *run* section. Both pictures are taken in the upstream direction. The black arrow shows the flow direction.

The optimal settings were not found for this system, resulting in the generation of air bubbles that were too small to produce a backscattered signal large enough at the velocity measurement point. Several modifications were attempted, including increasing the supply voltage or insulating the threaded bars, however without any real impact. Considering that the measurement point was a little more than twenty metres downstream of the air bubbles generator, another portable system was also tested - shown in Figure *4.6* (right) -, again without sufficient impact on the backscattered signal. As the right settings for the hydrolysis apparatus were difficult to find, it was finally decided to use an alternative solution, namely the injection of solid tracers into the water, upstream of the measurement point.

The chosen tracer is a quartz powder, with a diameter lower than 40 $[\mu m]$. In addition to its good dispersibility and low agglomeration potential, this powder also has the advantage of being readily available in large quantities, an important advantage in repeated experiments such as the UVP velocity measurements. The main disadvantage of the use quartz lies in the difference between its calculated density $\rho_q = 2650$ $[kg/m^3]$ and the density of water $\rho_w = 1000$ $[kg/m^3]$. The vertical downwards drift of the particles in the channel may therefore cause an unrepresentative behavior of the flow field during the water velocity measurements, which should be kept in mind when interpreting the results. To minimise the above-mentioned impact, the tracer was injected at a good distance from the measurement point, approximately 5 [m] upstream.

4.1.2.3 Setup

The velocity measurement location was chosen at a distance $L = 23$ [m] from the upstream end of the channel. This choice was guided by the fact that this position corresponds to that of the fifth ultrasonic sensor, making it possible to compare the mean velocity obtained using UVP technology with those derived using the water level values read by means of US sensor and the discharge. *Figure 4.7* presents a top view of the channel, where the location of the measurements is symbolised by a purple line.

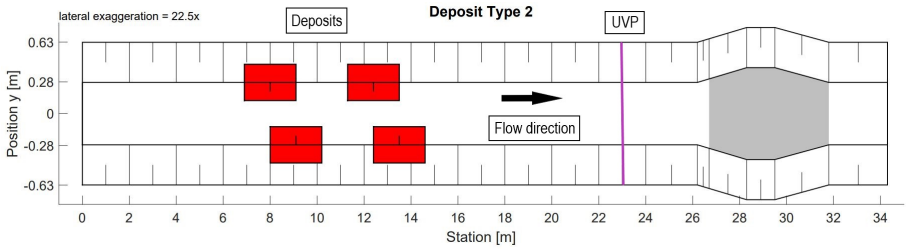

FIGURE 4.7 – Top view of the morphological channel without bank roughness. The red rectangles correspond to the sediment deposits and the purple line to the location of measurements.

To guarantee a constant angle between the transducer's and the flow's axis during the measurements and to allow measurements to be taken at different points along the lateral profile of the physical model, a mount was designed to fix the transducer during the experiments. It consists of a platform held by four rods, which allow the height of the transducer to be modified according to the flow rate - and therefore the height of the water -, guaranteeing that the tip of the transducer is permanently immersed. The platform has two holes in which the transducer can be placed, each with a different inclination, ensuring that the angle considered does not vary between two experiments due to small inaccuracies.

At their upper end, the four rods are attached to another platform that can be moved across the entire width of the channel by means of a rail, allowing to take measurements both in the center and on the banks of the channel. *Figure 4.8* presents the final result without flow (left) and for $Q = 20$ [L/s] (right), while the drawings required to manufacture the various parts are detailed in *Appendix A.4*.

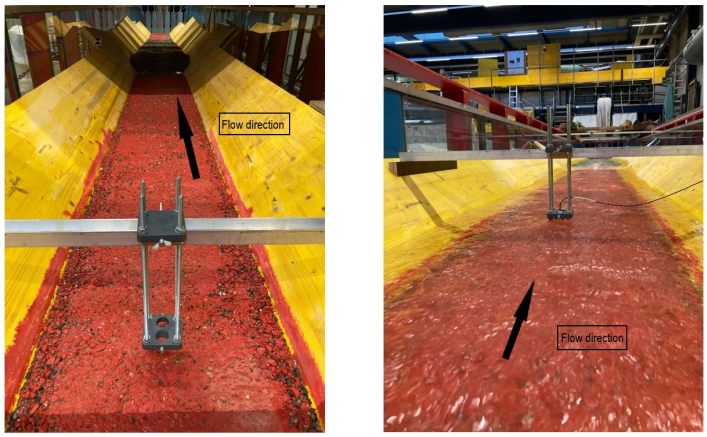

FIGURE 4.8 – Mount holding the UVP transducer at zero flow (left) and $Q = 20$ [L/s] (right). Both pictures are taken in the *run2* section, looking in the downstream direction. The Black arrows show the flow direction.

4.1.3 Ultrasonic sensor (USS)

Seven *ultrasonic sensors* (USS) were used to measure the height of water at various locations in the physical model. *Figure 4.1* presents their positioning by means of small yellow triangles. The water height values obtained from the USS can then be used to derive the mean water velocity. *Figure 4.9* shows the third USS, positioned at the level of the second sediment deposit in the *riffle* section.

FIGURE 4.9 – Third ultrasonic sensor (USS) located in the *riffle* section.

4.1.4 Laser scanner

To get the topographical information used to create the mesh required for the numerical simulations, a three-dimensional point cloud is generated by means of a laser scanner. A *Leica ScanStation P20* was used, which recorded the channel by four overlapping scans. The scans were aligned to each other and to a same reference using *Cyclone* software. The display resolution was *3917 x 8392*, and the average number of points used for a mesh was 200 million. Mesh was created using *3DReshaper* software. For analyses carried out by means of *Basement*, a regular sampling with an average distance between points of 0.05 [m] was used. For the analyses carried out by means of *Matlab*, a regular sampling with an average distance between points of 0.01 [m] was used.

4.1.5 Roughness addition

The artificial addition of roughness to the banks of the physical model was carried out using *StratexMat18*, a three-dimensional geonet with an average thickness of 18 [mm] and a mass per unit area of 500 $[g/m^2]$. For this purpose, a height of 30 [cm] was installed by means of a stapler on the banks of the channel, height ensuring that all the flows up to 80 [L/s] are in contact with the foam. The value of the Strickler coefficient of this geonet, unknown at the beginning of the experiments, will have to be calibrated later by comparing the results obtained on the physical model with those of the numerical model. Furthermore, the average thickness of this roughness reduces the width of the channel to a value $w_r = 0.52$ [m], as mentioned in *Section 4.1.1*. *Figure 4.10* shows the channel before (left) and after (right) the foam installation.

FIGURE 4.10 – Channel in its initial state (left) and after the installation of the geonet (right). Both pictures are taken in the *run* section, looking in the downstream direction. The black arrows show the flow direction.

4.2 Methodology

4.2.1 Data acquisition

The location of the velocity measurements were detailed in *Section 4.1.2.3*. Concerning the orientation of the transducer, an angle $\beta = 65$ [°] inclined vertically against the flow axis was chosen. This value is within the range suggested by Ubertone, which recommends an angle of 75 [°] with respect to the flow axis. Indeed, if an angle closer to the vertical would lead to a smaller component on the axis of the transducer, allowing a gain in terms of measurable velocity interval (Nyquist-Shannon theorem), an angle closer to the horizontal and the larger component which results from it makes it possible to increase the depth of the measurements. The choice of the angle value is therefore intended to balance these two constraints as well as possible.

At first instance, the use of a second transducer downstream of the first, with an angle 97 [°] inclined vertically in the direction of the flow axis, was intended to provide a more accurate picture of the flow. However, this choice was abandoned for two major reasons. Firstly, as explained above, an angle close to the vertical leads to a smaller component on the axis of the transducer, reducing the depth of the measurements. Moreover, by pointing out that the tip of the transducers must be immersed, the presence of the upstream transducer interfered somewhat with the regime of the channel, deteriorating the velocities measured a few centimeters downstream by the second transducer. This lack of precision led to the abandonment of the transducer pointing downstream. *Figure 4.11* presents a longitudinal profile of the velocity measurement section, where h [m] is the water height, h' [m] is the depth in the axis of the transducer, Δh [m] is the depth of immersion of the transducer and h_1 [m] is the distance between the bed and the transducer in the vertical axis.

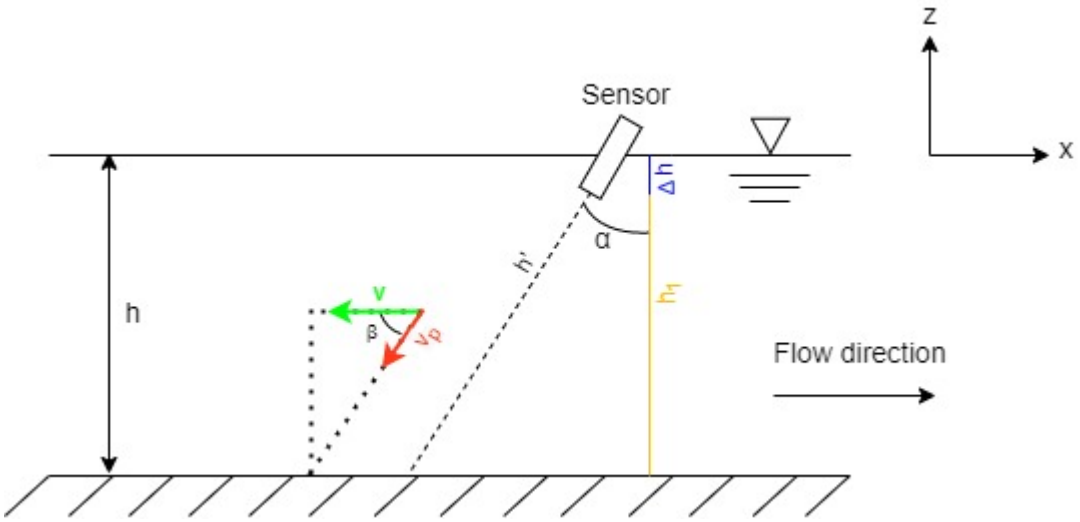

FIGURE 4.11 – Longitudinal profile of the velocity measurement section. V is the velocity in the flow axis, v_p is the projection of the velocity in the axis of the transducer, h is the water height, h' is the depth in the axis of the transducer, Δh is the depth of immersion of the transducer, h_1 is the distance between the bed and the transducer in the vertical axis, α is the angle between the transducer axis and the vertical axis and β is the angle between the transducer axis and the flow axis.

To ensure that the results are accurate enough, it has been decided to measure velocities at ten equidistant points. The points at the ends correspond to the transition between the bed of the physical model and the banks, with a safety margin of 2 [mm]. This margin should ensure that the velocities measured are that of the bed and not of the banks, as well as take into account the subsequent installation of the roughness, which reduces the width of the channel by 1.5 [cm] at each bank. As the initial bed is 55 [cm] wide - 52 [cm] with the added roughness -, the ten measurements were each spaced at 5 [mm] intervals. By convention, the first measurement corresponds to the one on the right bank looking downstream, and so on until the tenth one which corresponds to the one on the left bank looking downstream. A schematic representation of the measurement points is presented in *Appendix A.5*, where $w_c = 0.55$ [m] is the initial channel width, and $w' = 0.05$ [m] is the distance between two measurement points. Furthermore, several parameters have to be set up depending on the desired result before using UVP. The different inputs required and the conditions used for the experiments are presented in *Appendix A.6 (Table A.2)*. These settings remained similar for the four different flow rates tested - which will be specified later -, as well as for the two types of experiments considered, namely with and without added bank roughness.

Using these input parameters, the system is then able to determine the achievable resolution. As it is often the case, the input values are the result of a weighing of interests according to the expected output results. Displays information derived from the setup parameters for both experiments are shown in *Appendix A.6 (Table A.3)*.

To limit the impact of the quartz powder on the velocity measurements as much as possible, the tracer was injected 5 [m] upstream of the measurement location. Four different flow rates were considered, namely 20, 40, 60 and 80 [L/s]. A fifth flow rate of 100 [L/s] was initially planned, but the risks associated with a possible overflow of the physical model and time constraints led to its abandonment. Finally, to ensure that the velocities obtained were representative of the general dynamics and not only of a particular event, each measurement took place during a time step of about 50 [s]. Once the recording on the UB-Lab P has started, the resulting profiles are stored, before being downloaded in a binary data file after stopping the recording [94]. By uploading these files to a processing and visualization tool, it is therefore possible to process the data obtained.

4.2.2 Data processing

Once the file has been uploaded to the cloud, the first step is to determine in which distance range from the transducer the data obtained are usable. Indeed, if the velocities cannot be read in the first few millimeters following the transmission of the signal because of the resolution, it is also important to determine how far away the bottom of the channel is, to not take into account deeper values which have no physical meaning in the context of producing a velocity profile. To achieve this, the evolution of the signal-to-noise ratio (SNR) as a function of the distance to the transducer should be studied. The SNR is a measure to compare the level of a desired signal to the level of background noise. When the SNR is greater than 0 [dB], this indicates that there is more signal than noise, in other words that the signal is satisfactorily legible. In velocity measurements, the signal will be altered in the first few millimeters and when it reaches the bottom of the channel. At these points, the SNR will become negative, allowing their identification. The evolution of the SNR at the eighth measurement point for a flow rate of 20 [L/s] without bank roughness is presented in *Figure 4.12* (down), as a function of distance from the transducer. By applying the above procedure, it is possible to estimate that the bottom of the channel is 5.4 [cm] away from the transducer, while the first usable data is obtained after around 1.5 [cm]. These two boundaries are represented using black lines.

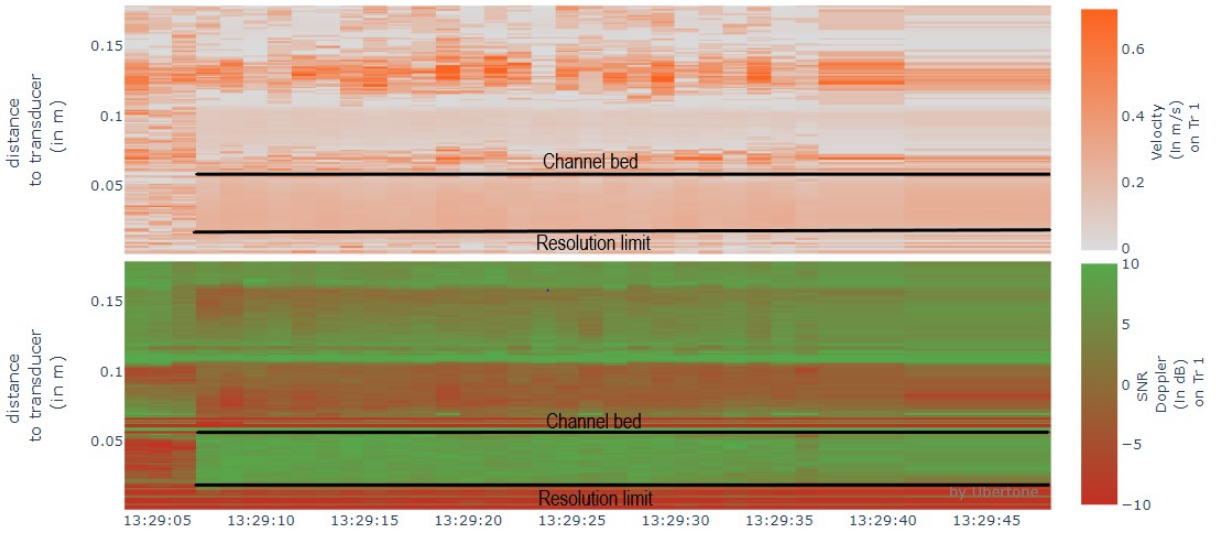

FIGURE 4.12 – Evolution of SNR [dB] (down) and velocity [m/s] (up) with respect to the vertical distance to transducer. The resolution limit and the channel bed are represented using black lines.

To confirm the interval considered, a profile representing the evolution of the velocity as a function of the distance to the transducer is also available. As the flume measurements are assumed to correspond to a stationary flow field, it is expected that they will not change over time within the considered distance interval. This is indeed the case for the range from 1.5 [cm] to 5.4 [cm] previously discussed, as it can be seen in *Figure 4.12* (up), where the two black lines represent the channel bed and the resolution limit. Once these two boundaries have been identified, the velocity data contained in this interval can be exported in readable files, so that the measured velocities can be analysed using software such as *Matlab*.

Recalling that the measured values correspond to a projection on the axis of the transducer, the next step is to extract the flowing velocity V along the horizontal axis. To do this, the *trigonometric relation (8)* presented in *Section 4.1.2.1* and recalled below (9) is applied, considering an angle $\beta = 65$ [°]. In addition, it should be mentioned that the velocities point towards the upstream side of the channel, so they will be positive according to the convention. The second step is to project the measured distances from the transducer onto the vertical axis z. Indeed, as for velocities, the primary objective is to relate the various quantities measured along the transducer axis to the (x,z) axis. This projection of the distance is carried out by means of the *trigonometric relation (10)*, where $\alpha = 90$ [°] $- \beta = 25$ [°]. *Figure 4.11* presents the different components for the calculation of the velocity and of the distance.

$$cos(\beta) = \frac{v_p}{V} \leftrightarrow V = \frac{v_p}{cos(\beta)} \leftrightarrow V = \frac{v_p}{cos(65°)} \leftrightarrow V = \frac{v_p}{0.4226} \tag{9}$$

$$cos(\alpha) = \frac{h}{h'} \leftrightarrow h = h' \cdot cos(\alpha) \leftrightarrow h = h' \cdot cos(25°) \leftrightarrow h = 0.9063h' \tag{10}$$

As the extremity of the transducer is slightly immersed in the water, the measured distances do not really correspond to the distance with respect to the water surface, but rather to a distance h_1 [m] starting at the end of the transducer. To determine the actual depth of the velocities obtained with respect to the water surface, the water height h of the channel is first measured for the different flows. The following assumption is then made, namely that the deepest distance kept during the UVP measurements exactly corresponds to the bottom of the channel. Looking at *Figure 4.11*, it is then possible to determine the depth Δh [m] of immersion of the transducer tip in the water. The corrected depth h of the measurements with respect to the water surface is finally obtained using *equation (11)*. The measured depths for the different flow rates are presented in *Appendix A.7*.

$$h = h_1 + \Delta h \tag{11}$$

To assess the reliability of the velocities obtained with the UVP method, it has been decided to measure the velocities inside the channel by means of a micro-propeller. This method was applied to the scenario without added bank roughness for the four flows considered, at all ten measurement points. Mean flow velocity using the micro-propeller was obtained by measuring the velocity at six-tenths of depth [62]. Finally, recalling the relation $V = \frac{Q}{A}$, where A $[m^2]$ corresponds to the wetted cross-sectional area, a value of velocity for the different flows can also be derived from the water depths measured by means of USS.

The vertical velocity profiles presented in *Section 4.3* are obtained using *equations (9)* and *(10)*. The horizontal velocity profiles presented in *Section 4.3* are obtained by considering the average velocity values at six-tenths of depth obtained from the transducer - both with and without added bank roughness - and the micro-propeller, as well as the values derived from the water depths.

4.3 Results

This section presents the vertical and horizontal profiles obtained for the two scenarios considered. The values measured at any point of the vertical profile correspond to an average over the selected time interval shown in *Figure 4.12*. The vertical velocity profiles obtained for a flow rate of 20 [L/s] are presented below, both in the absence of added bank roughness *(Figure 4.13)* and after the addition of the geonet *(Figure 4.14)*. The six profiles corresponding to flow rates of 40, 60 and 80 [L/s] are presented in *Appendix A.8*.

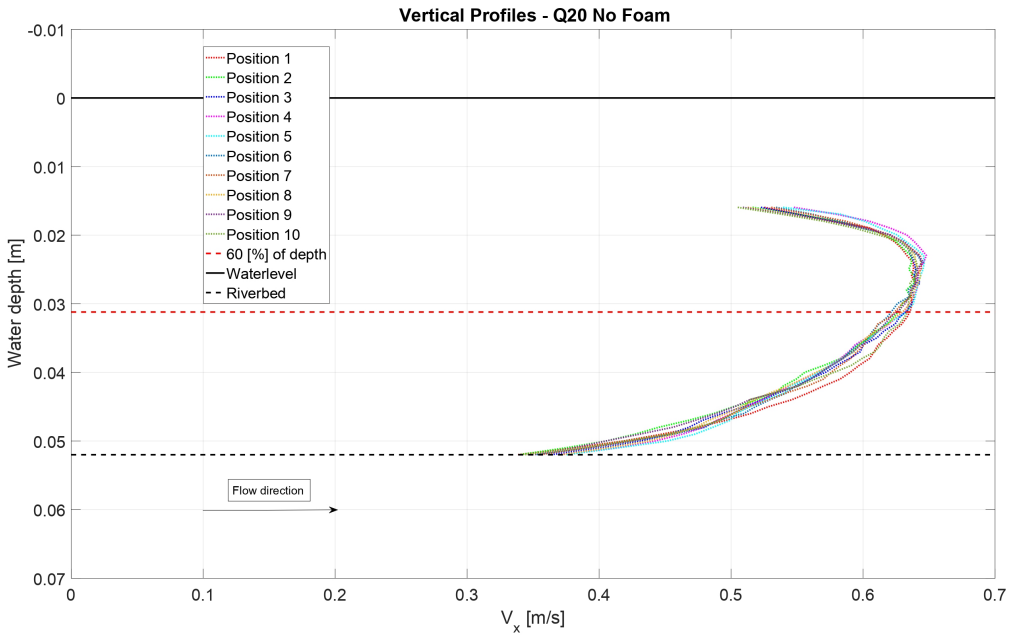

FIGURE 4.13 – Vertical profiles for a flow rate of 20 [L/s] at the ten measurement points without foam.

Table 4.2 summarizes the average velocities obtained at each of the ten measurement points for a flow rate of 20 [L/s]. For this purpose, the values measured using the UVP technology without added bank roughness (1), the values obtained using the micro-propeller without added bank roughness (2), the derived results without added bank roughness (3) and the values measured using the UVP technology with added bank roughness (4) are presented successively. The values obtained for flow rates of 40, 60 and 80 [L/s] are presented in *Appendix A.9*.

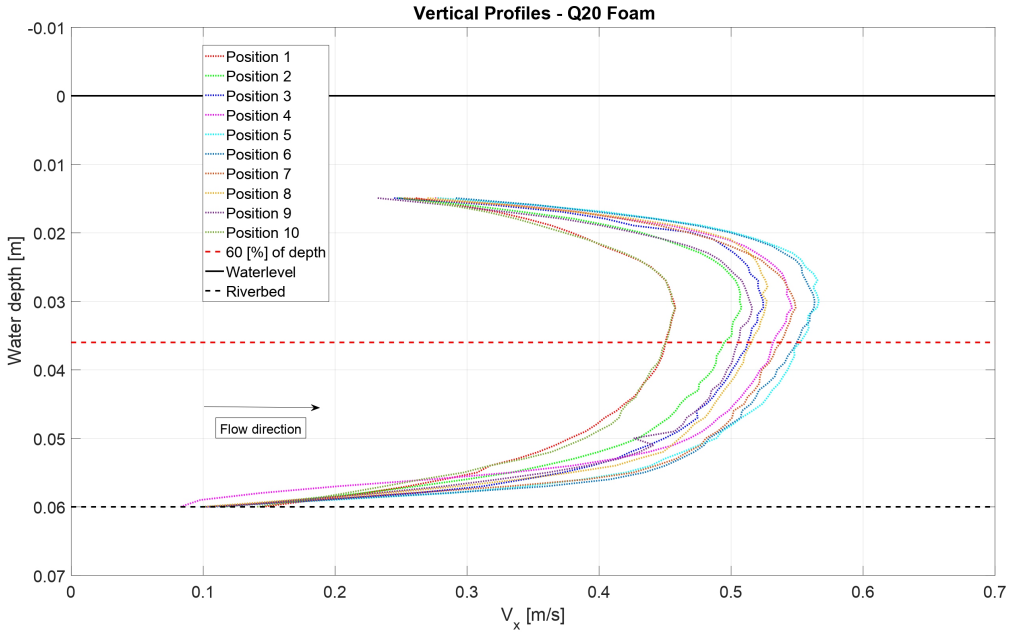

FIGURE 4.14 – Vertical profiles for a flow rate of 20 [L/s] at the ten measurement points with foam.

Position	$\mathbf{V_{UVP,no}}$ **[m/s]**	$\mathbf{V_{micro,no}}$ **[m/s]**	$\mathbf{V_{de,no}}$ **[m/s]**	$\mathbf{V_{UVP,rgh}}$ **[m/s]**
1	0.63	0.61	0.64	0.45
2	0.63	0.62	0.64	0.50
3	0.63	0.61	0.64	0.51
4	0.63	0.61	0.64	0.53
5	0.63	0.63	0.64	0.55
6	0.62	0.60	0.64	0.55
7	0.63	0.61	0.64	0.54
8	0.63	0.62	0.64	0.52
9	0.63	0.63	0.64	0.50
10	0.63	0.62	0.64	0.45

TABLE 4.2 – Average velocities obtained at the ten measurement points using UVP technology without added bank roughness, a micro-propeller without added bank roughness, the derived values without added bank roughness and UVP technology with added bank roughness, for $Q = 20$ [L/s].

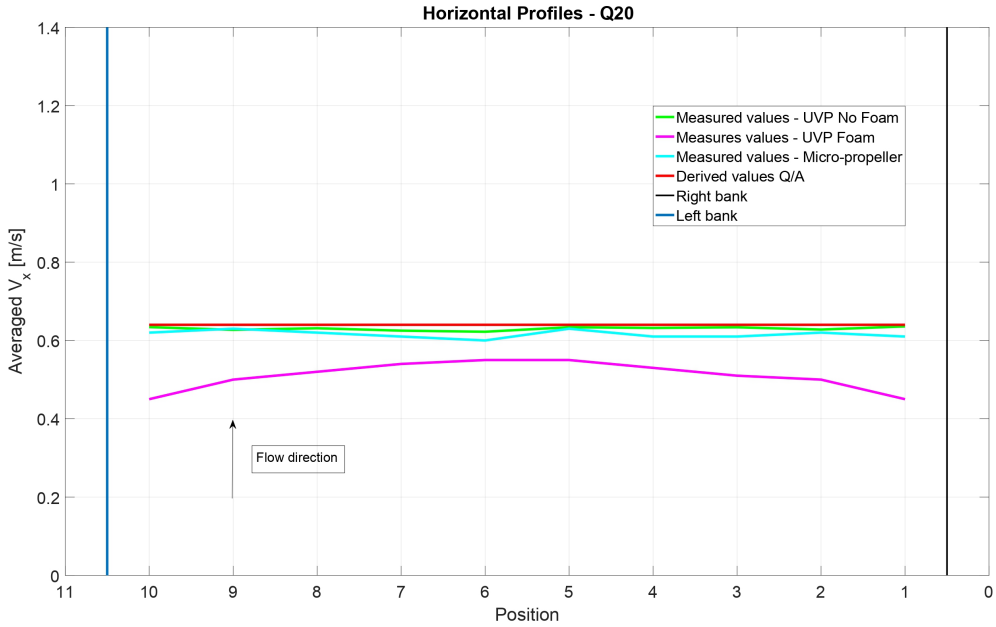

FIGURE 4.15 – Horizontal profiles for a flow rate of 20 [L/s] at the ten measurement points for measured values using UVP technology without added bank roughness (green), measured values using UVP technology with added bank roughness (purple), measured values using micro-propeller (blue) and derived values (red).

The horizontal velocity profiles obtained along the ten measurement points for a flow rate of 20 [L/s] are presented in *Figure 4.15*. The values obtained without bank roughness using the three different methods for a flow rate of 20 [L/s] are very similar. If the velocities measured with the micro-propeller have very slight variations, these do not exceed a 5 [%] threshold. The results obtained using the UVP technology are even more consistent, since only the velocity measured at the sixth point varies by 0.01 [m/s] compared to the others. Moreover, the fact that the velocities measured at the center of the channel are similar to those measured at its banks indicates that the banks only have a very limited influence on the velocity profiles obtained in the absence of the geonet.

The velocities measured by means of the UVP technology with additional roughness on the banks present a different profile. The addition of roughness on the banks results in an overall slowing down of the water velocities, varying between 13 [%] in the center and 29 [%] on the banks with respect to the scenario without the geonet. This result is consistent with the observations made during the physical model measurements, namely that the overall water depth had increased from 5.2 [cm] to 6 [cm] in the center of the channel, and that this increase was even greater on the banks. If these first results tend to indicate that the addition of roughness on the banks modifies the general velocity profile of the channel by slowing it down at all points, *Table 4.2* indicates that the order of magnitude of this reduction will decrease rapidly, away from the banks. If the velocities measured at points one and ten correspond to a decrease of 29 [%] with respect to the initial velocities, those measured at points two and nine are only reduced by 21 [%] compared to the velocities obtained without roughness on the banks. The results observed on the horizontal profiles are confirmed by the reading of the vertical profiles. If the velocities are very similar at the ten measurement points in the

absence of added roughness on the banks *(Figure 4.13)*, the vertical profiles obtained after the addition of geonet on the banks shows an overall decrease in velocities, which is particularly pronounced in the vicinity of the river banks *Figure 4.14*.

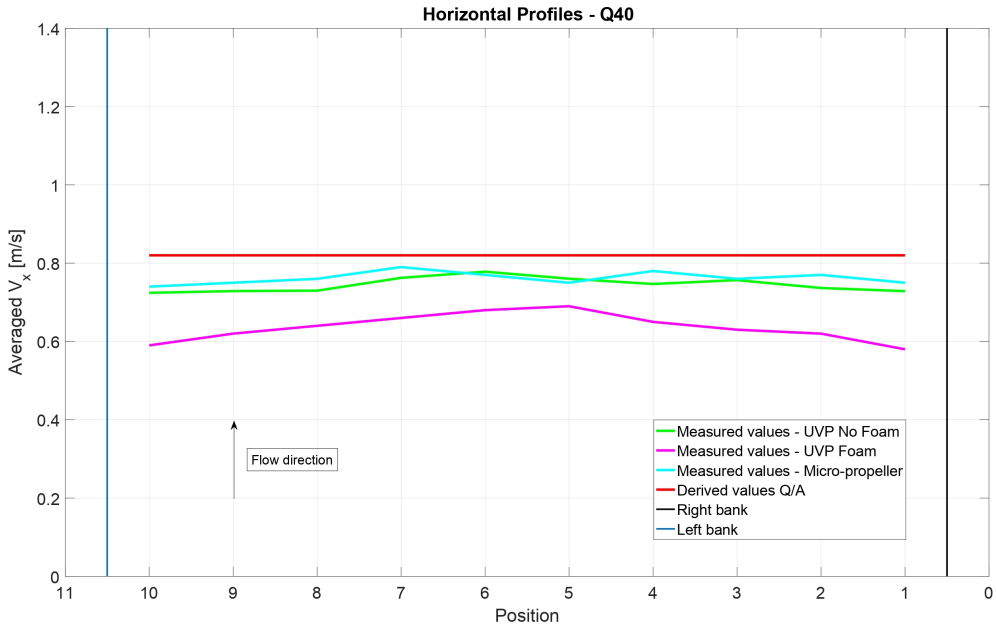

FIGURE 4.16 – Horizontal profiles for a flow rate of 40 [L/s] at the ten measurement points for measured values using UVP technology without added bank roughness (green), measured values using UVP technology with added bank roughness (purple), measured values using micro-propeller (blue) and derived values (red).

The horizontal velocity profiles obtained along the ten measurement points for a flow rate of 40 [L/s] are presented in *Figure 4.16*. It can be observed that they follow a relatively similar dynamic to the one described for a flow rate of 20 [L/s]. Concerning the average velocities measured in the absence of added roughness on the banks *(Appendix A.9, Table A.5)*, the variation is this time smaller using the micro-propeller, as they do not exceed 7 [%] between the different points of measurements. This variation also reaches a maximum of 7 [%] for the velocities measured by means of the UVP technology. Although the values obtained at the center of the channel are slightly higher than those at the banks, the order of magnitude of the variation remains moderate.

Concerning the velocities measured in the presence of added roughness on the banks, these present a similar pattern to the one previously described, with lower values than those obtained in the absence of added roughness. The depth of water in the center of the channel also increases with the addition of the geonet, from 7.8 [cm] to 8.8 [cm]. The reduction in velocity with respect to the scenario without foam is again more pronounced on the banks, where it amounts for 21 [%] versus 10 [%] in the center. By comparing these variations with those presented for a flow rate of 20 [L/s], it can be observed that increasing the flow rate tends to uniformize the impact of bank roughness on the decrease in velocities, with a smaller variation between the banks and the center of the channel. This observation must now be confirmed for higher flows.

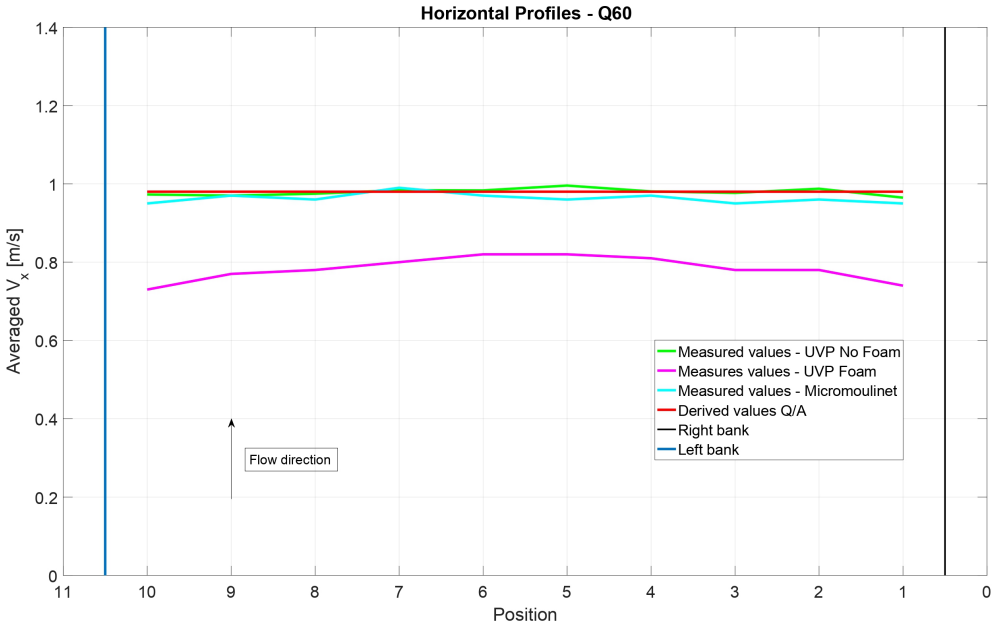

FIGURE 4.17 – Horizontal profiles for a flow rate of 60 [L/s] at the ten measurement points for measured values using UVP technology without added bank roughness (green), measured values using UVP technology with added bank roughness (purple), measured values using micro-propeller (blue) and derived values (red).

The horizontal velocity profiles obtained along the ten measurement points for a flow rate of 60 [L/s] are presented in *Figure 4.17*. The average velocity values obtained without added roughness on the banks remain very similar, whether the measurements are carried out by means of the micro-propeller - 4 [%] variation -, or using the UVP technology - 3 [%] variation - *(Appendix A.9, Table A.6)*. In the presence of the geonet on the banks, the measured velocity values are reduced from 16 [%] in the center of the channel to 23 [%] on the banks, with respect to the scenario without added bank roughness. The reading of this result tends to confirm the observation developed previously, namely that an increase in the flow rate tends to more uniformly decrease the velocities between the banks and the center of the channel. The depth of water in the middle of the channel changes from 9.5 [cm] in the absence of added roughness on the banks to 11.6 [cm] once roughness is added, a variation of approximately 20 [%] corresponding to the order of magnitude of the reduction of the velocities.

Furthermore, the reading of the vertical profiles *(Appendix A.8, Figure A.13)* highlights the fact that the velocities measured near the banks are higher than those in the center, at a depth corresponding to the riverbed. The higher water depth observed near the banks with respect to the water depth at the center of the channel can explain this finding : as a result of this difference of water depths, the bottom of the bed is therefore not reached after 11.6 [cm] on the banks but a few millimetres lower, justifying a somewhat higher velocity.

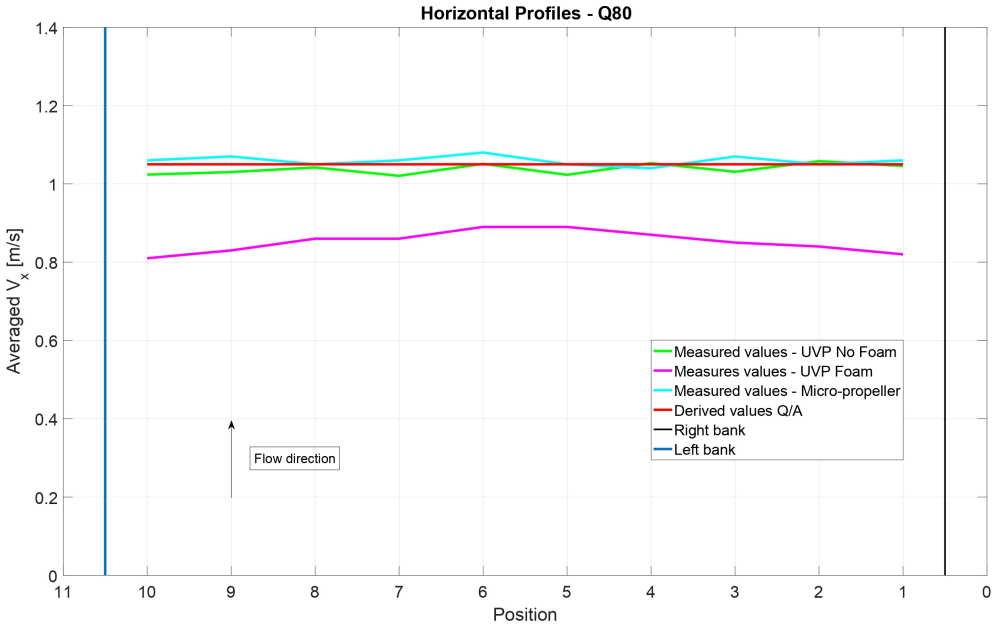

FIGURE 4.18 – Horizontal profiles for a flow rate of 80 [L/s] at the ten measurement points for measured values using UVP technology without added bank roughness (green), measured values using UVP technology with added bank roughness (purple), measured values using micro-propeller (blue) and derived values (red).

The horizontal velocity profiles obtained along the ten measurement points for a flow rate of 80 [L/s] are presented in *Figure 4.18*. In the absence of added bank roughness, the average values obtained at the various measurement points are very constant, with a variation of 3 [%] considering the use of the UVP technology and of 4 [%] by means of the micro-propeller *(Appendix A.9, Table A.7)*. This tends to reinforce the conviction that the velocities obtained at any point of the vertical profile are mostly subject to limited variations *(Appendix A.8, Figure A.14)*. The study of the vertical profiles corresponding to the addition of bank roughness illustrates the homogenisation of the velocities between the banks and the center of the channel *(Appendix A.8, Figure A.15)*. The clear separation, observable for smaller flow rates, between the values corresponding to the measurement points one and ten and the others practically disappeared. This observation is also reflected in the reduction of the velocities with respect to the scenario without roughness on the banks, since the reduction now varies between 16 [%] in the center and 21 [%] on the banks *(Appendix A.9, Table A.7)*, a much narrower interval than the one obtained for a flow rate of 20 [L/s].

4.4 Synthesis

The study of the horizontal and vertical velocity profiles revealed several findings. Concerning the scenario without added roughness on the banks, the average velocity - corresponding to the velocity measured at six tenths of the depth - remains practically constant throughout the ten points of measurements, for all considered flow rates. If the values obtained for a flow rate of 40 [L/s] can suggest a slight increase of the velocities in the center of the channel, the variation - of the order of 7 [%] between the banks and the center - remains very moderate. The study of vertical and horizontal profiles obtained by considering the addition

of roughness on the banks illustrates the impact of increased roughness on channel flow. If the measured velocities are everywhere lower than those obtained without roughness, the reduction differs according to the range of flow rates considered. In the presence of low flow rates - 20 [L/s] in the case of this study - the effect of roughness is particularly noticeable in the areas close to the banks, where the decrease in velocity is of the order of 29 [%] with respect to the velocities measured without the geonet, against 13 [%] in the center of the channel. This important variation leads to a greater depth of water on the banks, according to the flow rate equation $Q = V \cdot A$. On the other side, the more the flow rate increases, the more the range of variability between the banks and the center of the channel tends to decrease, leading to a progressive homogenization of the water depth as well as of the measured velocities. For a flow rate of 80 [L/s] - the largest considered within the framework of this study - calculations showed that the decrease in velocities near the banks amounted to 21 [%] compared to the measurements without added roughness, versus 16 [%] in the center of the channel. This more pronounced increase in water depth on the banks can also be justified by the study of the Manning-Strickler equation (3), presented in *Section 2.3*. The roughness on the banks exerting a stronger influence in their vicinity than in the center of the channel, the roughness near the banks will therefore be higher, meaning the k_{st} value will be lower. Furthermore, since neither the flow rate, nor the area, nor the slope change, this decrease in the value of k_{st} will have to be compensated by an increase in the hydraulic radius, and therefore an increase in depth of water.

Looking at the results obtained, it is important to bear in mind the possible impact of the *riffle2* section three metres downstream on the measurement of velocities, particularly with respect to a possible backwater curve. To reduce this potential influence as much as possible, the bottom of the *riffle2* section was flattened before the experiments. However, if the bottom of the *riffle2* section was not disturbed by low flow rates, the experiments carried out with flow rates of 60 and 80 [L/s] have resulted in some modification of its structure, creating areas of depression and others of sediment accumulation leading to eddy curves. As this modification induced by the transit of high flow rates was not initially observed, the bottom of the *riffle2* section was not flattened prior to the second set of experiments conducted with added roughness on the banks. Consequently, the velocities measured for flow rates of 20 and 40 [L/s] could potentially have been a little distorted by morphological disturbances, the depression created at the entry of the *riffle2* section may have led to an increase in the measured velocities.

Finally, considering a constant water depth - measured at the center - over the whole lateral profile of the physical model in the presence of added roughness on the banks can be seen as a somewhat rough approximation. As the depth of water is greater on the banks, the average velocities measured probably do not correspond to exactly six tenths of the depth, but rather to a few millimeters - or even centimeters - higher. However, as the variation of water depths near the banks remains reasonable, coupled with the reading of the various profiles of vertical velocities indicating no abrupt change of velocities around the six tenths of depths, the assumption of a constant depth throughout the whole lateral profile can be used, which simplify the calculations. If this study of the vertical and horizontal velocity profiles made it possible to highlight the impact of bank roughness on the measured velocities, the results obtained in this section will now be used to properly calibrate the numerical model.

5 Numerical model

The numerical simulations presented in this study are carried out via the program *Basement* : a freeware simulation tool for hydro- and morphodynamic modelling, developed at the *Laboratory of Hydraulics, Hydrology and Glaciology* (VAW) of the ETH Zurich since 2002 [95]. This software allows the simulation of flows, based on the numerical solution of the Barré de Saint-Venant equations for one-dimensional models, and on the shallow water flow equations for the hydrodynamics of two-dimensional models. These equations are based on the following four assumptions : the bottom slope is small enough for the longitudinal coordinate to coincide with the horizontal axis, the vertical acceleration of the water particles are assumed to be small compared to the longitudinal component of the acceleration, the flow regime is turbulent, and the water is assumed to be incompressible [95].

5.1 Scenarios

Table 5.1 presents the eight different scenarios studied using *Basement*. Four of them correspond to a physical model without added roughness on the banks, while the four others conserve the same characteristics, this time considering the addition of bank roughness presented in *Section 4.1.5*. *Figure 5.1* shows the two hydrographs considered, where the *Channel State 1* associated with run 4 corresponds to the physical model without added roughness on the banks, and the *Channel State 2* associated with run 5 corresponds to the physical model once the geonet has been added to the banks. *Appendix B.1* presents a top view of the physical model for each of the different scenarios.

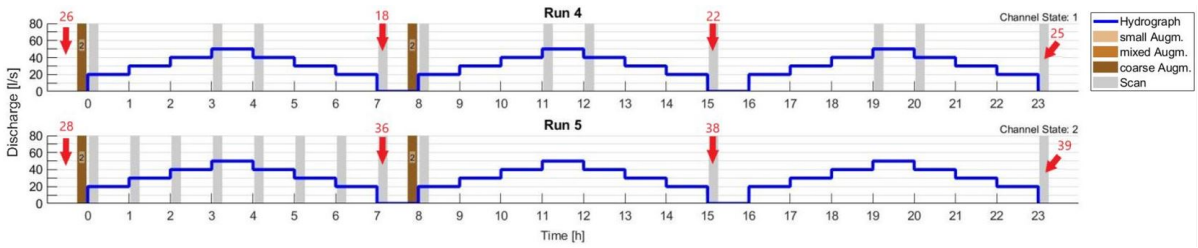

FIGURE 5.1 – The hydrographs considered are shown in blue. Run 4 corresponds to the channel without added bank roughness, while run 5 refers to the channel with added bank roughness. The brown rectangles correspond to coarse sediment augmentation. The grey rectangle corresponds to scans of the channel status. The red arrows represent the eight different scenarios studied using the physical model. The numbers associated with these arrows follow the terminology presented in *Table 5.1*.

Position	Referred as	Additional bank roughness	Characteristics
26	Initial26	No	Initial state without sediment deposits.
18	Initial18	No	Four coarse sediment deposits with a total volume of 0.21 $[m^3]$ were added to the channel. This scenario corresponds to the situation after the first seven-hour hydrograph was completed.
22	Initial22	No	After the first hydrograph was completed, four new coarse sediment deposits were added to the channel. This scenario corresponds to the situation after the completion of the second seven-hour hydrograph.
25	Initial25	No	After the second hydrograph was completed, no new sediment deposit was added to the channel. This scenario corresponds to the situation after the third seven-hour hydrograph has been completed.
28	Foam28	Yes	Initial state without sediment deposits.
36	Foam36	Yes	Four coarse sediment deposits with a total volume of 0.21 $[m^3]$ were added to the channel. This scenario corresponds to the situation after the first seven-hour hydrograph was completed.
38	Foam38	Yes	After the first hydrograph was completed, four new coarse sediment deposits were added to the channel. This scenario corresponds to the situation after the completion of the second seven-hour hydrograph.
39	Foam39	Yes	After the second hydrograph was completed, no new sediment deposit was added to the channel. This scenario corresponds to the situation after the third seven-hour hydrograph has been completed.

TABLE 5.1 – Characteristics of each simulation studied using *Basement*.

5.2 Methodology

The completion of the hydrographs shown in *Figure 5.1* leads to the various morphologies, formed by flooding in the flume, presented in *Appendix B.1*. To simulate the behaviour of a residual flow, or during a flooding event, with the emerged morphology using *Basement*, it is first necessary to develop a mesh that best represents the real topography of the study area. The methodology for the creation of the mesh - generated with the help of the *QGIS* program and its extension *BASEmesh* - required for the numerical simulations is presented below.

5.2.1 Data acquisition

The first step was to import the various physical model topologies into *QGIS*. To do this, scans - shown in grey in *Figure 5.1* - were taken of the physical model, providing a point cloud. In the post processing of the scanner data, the approximate distance between two points has been fixed at 5 [cm] for the mesh creation. This choice is a compromise between ensuring sufficient resolution for the interpretation of the results, while keeping the calculation time acceptable. Indeed, the use of a smaller number of elements and nodes can drastically increase the computational efficiency and reduce the simulation time on *Basement*.

5.2.2 Establishment of the mesh

The numerical methods used in *Basement* are based on a discretization of the domain topography into unstructured triangular elements, which act as control volumes (1st order finite volume) for the calculation of the flow equations [95]. The development of a mesh using *BASEmesh* is carried out in three distinct stages. The *Elevation Meshing* is used to generate a first mesh, based on the coordinates measured on the ground, in the form of a network of irregular triangles. It is also possible to set certain constraints, including one stipulating that each vertices of the triangles must lie on a point of the cloud whose coordinates are known.

Once this first step is completed, the *Quality Meshing* is used to create different zones within the mesh by means of breaklines. Each zone can then be assigned its own characteristics. Areas requiring more precision will thus be able to have a finer mesh. Within the same area, several elements can be enforced, including the maximum area [m^2] of the triangles forming the mesh, or the minimum angle [°] enforced for any mesh elements generated. Finally, a MATID material index is also specified, which allows to apply a specific roughness coefficient to each zone during the numerical simulation. *Table 5.2* presents the characteristics of the different zones delimited, while *Figure 5.2* shows part of the *Initial26* mesh, illustrating the differences in the area of the triangles between the banks and the bed.

Zone	Maximum area	Minimum angle	MATID
Embankment	0.01	28	1
Riverbed	0.001	28	2

TABLE 5.2 – Characteristics used for the creation of the *Quality Meshing*. Maximum area and minimum angle refer to the triangles forming the mesh. MATID is an index allowing, among other things, different roughnesses to be assigned to the areas under consideration.

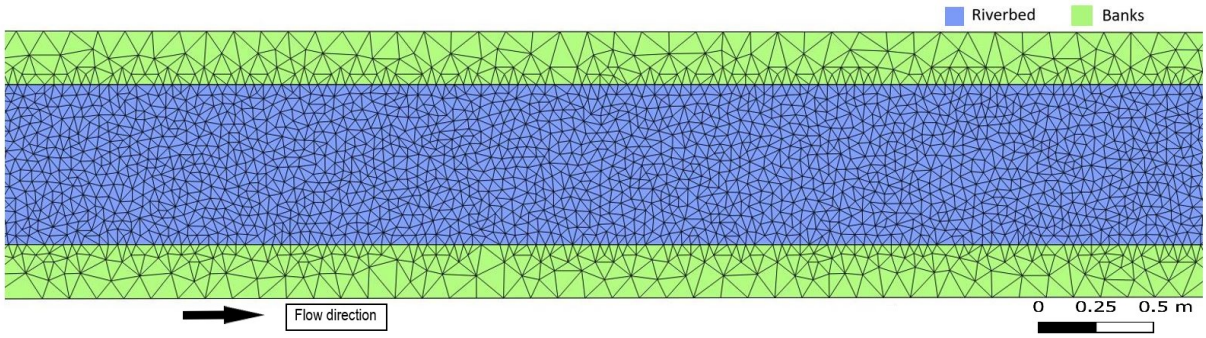

FIGURE 5.2 – Part of the *Initial26* mesh, where the riverbed corresponds to the blue area and the banks to the green areas.

As the points of the *Quality meshing* do not have any elevation value, the *Interpolation* tool is finally used to incorporate the elevation data contained in the *Elevation Meshing* into the nodes of the *Quality Meshing*. The elevation value - equally distributed over the area of the element - is assigned to the center of each triangle, whereas the edges of the element define the boundary of the control volume and the connection between neighbouring elements. The final mesh characteristics for the eight scenarios are presented in *Table 5.3*.

Scenario	**Vertex count**	**Face count**
Initial26	18168	35561
Initial18	18053	35340
Initial22	18052	35316
Initial25	18168	35550
Foam28	17899	35152
Foam36	17784	34912
Foam38	17929	35073
Foam39	17981	35179

TABLE 5.3 – Number of vertices and faces of the final meshes corresponding to the eight different scenarios.

5.2.3 HMID

To calculate the HMID of the simulated channel section for a residual flow, fourteen cross sections were selected, each separated by 2 [m] over a range of seven to thirty-three metres. The lower boundary of the interval was chosen to coincide with the first sediment deposit. In *Basement*, once the steady state was reached, the mean values and corresponding standard deviations of water velocities and depths were extracted along each of the cross-sections using the *Crayfish* tool - an extension providing extra functionalities to work with mesh data -. Using the values extracted, it was possible to calculate the value of the HHMID for each of the different scenarios considered. The cross sections considered for the HMID are presented in *Appendix B.2*.

5.3 Model calibration

To best represent the prevailing flow in the channel, many parameters must be specified on *Basement*prior to the numerical simulation. If a majority of these are known, the additional roughness of the banks as well as the roughness of the bed have to be calibrated using both velocity and water height profiles obtained by means of the UVP technology and presented in *Section 4.3*. The values assigned to the different parameters are detailed in the following sections.

5.3.1 Friction conditions

5.3.1.1 Without bank roughness

In the case of a channel without additional roughness on the banks, a Manning's coefficient $k_{mn} = 0.01\ [s/m^{\frac{1}{3}}]$ was chosen for the banks [46], which corresponds to a roughness according to Strickler of $k_{st,b} = \frac{1}{k_{mn}} = 100\ [m^{\frac{1}{3}}/s]$. This value corresponds to an artificial channel made of wood planks, a configuration very close to that of the physical model. *Appendix B.3* presents different values of the Manning's coefficient, depending on the conditions considered. To determine the roughness of the bed, a calibration based on the water depths and the velocities measured by means of UVP technology in the physical model has been performed. Various simulations were carried out with different roughnesses on *Basement*, to determine which value of roughness best represents the measured values in the physical model. Based on the results presented in *Appendix A.9*, three different scenarios were tested. The first considered a roughness according to Strickler of $k_{st,cr} = 30\ [m^{\frac{1}{3}}/s]$, corresponding to an artificial channel with rough and irregular stones. The second considered a roughness according to Strickler of $k_{st,cs} = 40\ [m^{\frac{1}{3}}/s]$, corresponding to an artificial channel with smooth and uniform stones. The third considered a roughness according to Strickler of $k_{st,cb} = 50\ [m^{\frac{1}{3}}/s]$, corresponding to an artificial channel made of rough breeze blocks.

Appendix B.4 presents in detail the comparison of the water depths and velocities obtained at the ten measurement points for the different flow rates considered, according to the roughness value chosen. To determine which roughness factor is the most appropriate, the mean value is calculated for the different flow rates and parameters considered. Table *5.4* summarizes the results obtained for water depths [m], where μ_{h_i} refers to the average value of water depth for a flow *i*.

	$\mu_{\mathbf{h_{20}}}$	$\mu_{\mathbf{h_{40}}}$	$\mu_{\mathbf{h_{60}}}$	$\mu_{\mathbf{h_{80}}}$
Physical Model	0.052	0.078	0.095	0.115
Numerical Model $\mathbf{k_{30}}$	0.063	0.096	0.122	0.154
Numerical Model $\mathbf{k_{40}}$	0.054	0.079	0.096	0.120
Numerical Model $\mathbf{k_{50}}$	0.047	0.069	0.083	0.102

TABLE 5.4 – Mean values with respect to water depth [m] for the physical model, as well as for the three roughness considered. The mean is given with respect to the four flow rates used in the physical model.

Table 5.5 summarizes the result obtained for velocities [m/s], where μ_{v_i} refers to the average value of velocity for a flow *i*. The reading of these two tables indicates that a roughness $k_{st,c} = 40\ [m^{\frac{1}{3}}/s]$ represents in a suitable way on the numerical model the values measured on the physical model. This bed roughness will therefore be retained for the rest of the study.

	$\mu_{\mathbf{h_{20}}}$	$\mu_{\mathbf{h_{40}}}$	$\mu_{\mathbf{h_{60}}}$	$\mu_{\mathbf{h_{80}}}$
Physical Model	0.629	0.747	0.979	1.039
Numerical Model $\mathbf{k_{30}}$	0.534	0.658	0.764	0.847
Numerical Model $\mathbf{k_{40}}$	0.609	0.786	0.947	1.059
Numerical Model $\mathbf{k_{50}}$	0.688	0.879	1.074	1.218

TABLE 5.5 – Mean values with respect to velocity [m/s] for the physical model, as well as for the three roughness considered. The mean is given with respect to the four flow rates used in the physical model.

5.3.1.2 With additional bank roughness

To determine the roughness of the geonet installed on the banks, a similar approach to that developed in *Section 5.3.1.1* is adopted, using only the velocities measured with the UVP technology. As mentioned in *Section 4.4*, the water depths were only measured at the center of the physical model, while they are higher on the banks. Using water depth values would therefore have only a relatively limited interest. Based on the results presented in *Appendix A.9*, three different scenarios were tested. The first considered a roughness according to Strickler of $k_{st,bs} = 20\ [m^{\frac{1}{3}}/s]$, corresponding to banks with stones on them [46]. The second considered a roughness according to Strickler of $k_{st,ss} = 25\ [m^{\frac{1}{3}}/s]$, corresponding to slightly less steeply sloping banks. The third considered a roughness according to Strickler of $k_{st,bg} = 30\ [m^{\frac{1}{3}}/s]$, corresponding to banks with stones and grasses.

Appendix B.5 presents in detail the comparison of the velocities obtained at the ten measurement points for the different flow rates considered, according to the chosen roughness value. To determine which roughness factor is the most appropriate, the mean value is calculated. *Table 5.6* summarizes the result obtained for velocities [m/s], where μ_{v_i} refers to the average value of velocity of a flow *i*. The reading of this table indicates that a roughness $k_{st,b} = 25\ [m^{\frac{1}{3}}/s]$ represents in a suitable way on the numerical model the parameters measured on the physical model. This value will therefore be retained for the rest of the study. In addition, it should also be mentioned that the roughness of the sediment deposits will be assumed to be equal to the roughness of the bed - i.e. $k_{st,s} = k_{st,c} = 40\ [m^{\frac{1}{3}}/s]$ -, an assumption that will be discussed later.

	$\mu_{\mathbf{h_{20}}}$	$\mu_{\mathbf{h_{40}}}$	$\mu_{\mathbf{h_{60}}}$	$\mu_{\mathbf{h_{80}}}$
Physical Model	0.510	0.636	0.783	0.852
Numerical Model $\mathbf{k_{20}}$	0.464	0.550	0.672	0.725
Numerical Model $\mathbf{k_{25}}$	0.518	0.652	0.796	0.857
Numerical Model $\mathbf{k_{30}}$	0.567	0.707	0.852	0.898

TABLE 5.6 – Mean values with respect to velocity [m/s] for the physical model, as well as for the three roughness studied. The mean is given with respect to the four flow rates used in the physical model.

5.3.2 Boundary and initial conditions

Boundary conditions provide information about what enters and leaves the channel. For the upstream boundary, three pieces of information must be filled in, namely the slope, the type of flow and the flow rate. As discussed in *Section 4.1.1.1*, the slope varies along the length of the physical model to best reproduce the characteristics of the Sarine. However, in the case of this simulation the following assumption was made, namely that the slope at the entrance of the channel had a value of J=0.003, corresponding to the average physical model slope.

For the simulation of a residual flow rate, the residual discharge from the reference reach $Q_{r,s} = 3.5$ $[m^3/s]$ was downscaled to the model dimensions, using Froude similarity. Froude similarity is based on the fact that to ensure that flows at different scales are dynamically similar, the Froude number must be equal between the model and its prototype for each selected experiment [96] [97]. Using the Froude similarity theory, a residual flow rate value $Q_m = 2$ [L/s] can be calculated for the physical model, corresponding to the residual discharge of the Sarine $Q_{r,s} = 3.5$ $[m^3/s]$. The associated water depth is $h = 0.023$ [m]. As this residual flow guarantees a Reynold's number greater than 500, the hypothesis of turbulent flow mentioned earlier is verified. Finally, a slope of 0.003 was retained for the downstream boundary of the model, while the initial state of the channel was defined as dry, meaning there is no water in the channel before the simulation started.

5.3.3 Other parameters

Several parameters are also required prior to the simulation. These include the *Current-Friedrichs-Lewy* (CFL) number [−], a parameter corresponding to the ratio between spatial resolution and time step [54], the density of the fluid $[kg/m^3]$, the maximum allowed timestep [s] for time integration, the minimum water depth [m] and the gravity $[m/s^2]$. The values assigned to these parameters are given in Table 5.7. Finally, a closer look at the simulations showed that a steady state was reached about four minutes after the launch. To study this so-called steady state, the simulations were therefore each carried out over a period of ten minutes, with a time step of one minute.

Parameter	Value	Unit
CFL	0.95	[-]
Density	1000	$[kg/m^3]$
Time step	100	[s]
Minimum water depth	0.001	[m]
Gravity	9.81	$[m/s^2]$

TABLE 5.7 – Input parameters required for simulations using *Basement*.

5.4 Results

This section presents the results obtained from the numerical simulations, for the eight scenarios presented in *Section 5.1*. The influence of bank roughness and bed structure will first be studied in the presence of a residual flow $Q_m = 2$ [L/s], with a special attention given to the HMID value associated to the different scenarios. The influence on bank roughness and bed structure on bedload will then be assessed, considering a flow rate $Q_{shear} = 50$ [L/s] corresponding to the peak value of the flood hydrographs. Finally, to determine the consequences of variable bank roughness and bed structure during flood events on flood transit, the simulations will be repeated for a flow rate $Q_{flood} = 100$ [L/s].

To limit the simulation time and to focus the results on the areas of interest, the first two metres of the physical model and the upper edges of the banks have not been reproduced in the numerical model. Thus, if the entire channel corresponds to the grey surface of *Figure B.3 (Appendix B.6)*, the results presented in this section will only show the part of the riverbed shown in light blue, and the part of the banks shown in brown. Finally, to refine certain parts of the analysis, two *Regions of Interest* (ROI) have been determined, regions on which a more in-depth study will be carried out on certain occasions. These two regions are presented in *Figure B.4 (Appendix B.6)*.

5.4.1 Residual flow

The two initial velocity profiles show a relatively similar behaviour *(Appendix B.7, Figures B.5 & B.8)*. The low velocities observed up to the first sediment deposit are due to the upward slope of the physical model in this section. The velocities then increase gradually, as the slope is now descending. The depression at the entrance of the channel is clearly visible, with velocities higher than 0.4 [m/s]. The fact that the velocities seem to differ a little in the *ROI 2* is mainly related to the intervals considered. Indeed, as the velocities vary around 0.1 [m/s], some are slightly higher than this value - thus presented in green -, whereas others are slightly lower - thus represented in blue -. A similar observation can be made studying the water depths presented in *Appendix B.8*, namely that the upward slope first leads to greater water depths due to the accumulation of water. Thereafter, the water level remains relatively constant, both with no added bank roughness *(Figure B.11)* and with added bank roughness *(Figure B.15)*. The depression near the *ROI 2* is again visible, with lower water depth values recorded. The fact that both initial profiles are practically similar is consistent with the very low impact of bank roughness with respect to bed roughness for a residual flow, as the ratio of wetted perimeter of the bank to wetted perimeter of the bed is $1 : 8$.

The water height profiles obtained after the addition of sediments and the completion of the first seven-hour hydrograph are presented in *Appendix B.8*. Unlike the initial scenarios, where the addition of bank roughness only influenced the results in a limited way, this second comparative study highlights several divergences between the two scenarios considered, especially near the sediment deposits *(ROI 1)*. In the absence of added roughness on the banks (*Figure B.12*), it is possible to observe the appearance of a limited number of dry areas near the deposits. Although the water depths are somewhat more varied with respect to the initial state, these variations remain limited. On the other side, the water heights measured near the sediment deposits show a more varied profile once the geonet has been added to the banks (*Figure B.16*). Many dry areas have appeared, especially near the center of the channel, creating a more sinuous pattern. The measured water heights therefore have a more pronounced variability, especially between the second and third deposits where they vary from 0 [cm] to more than 3 [cm] on the same profile. A few metres downstream of the deposits area, the profiles again adopt a relatively similar shape, up to the *ROI 2*. In this region, it should be noted that although both configurations have an area where the water height decreases, the apparition of a dry zone is observed near the left bank in the absence of added roughness on the banks, and near the center in the presence of the geonet on the banks.

A similar trend can be observed in the velocity profiles presented in *Appendix B.7*. In the absence of added bank roughness *(Figure B.6)*, the velocity evolves gradually in the vicinity of the first two deposits, with maxima at the center of the physical model. If these maxima move towards the left bank at the level of the two downstream deposits, the profile of velocities preserves a relatively constant shape. The addition of bank roughness *(Figure B.9)* breaks this pattern by increasing the variability of the velocities within the *ROI 1*. In this region, velocities now fluctuate in a sinuous manner, with zero values in the dry areas offset by a marked increase on the opposite bank. While the remainder of the model has broadly similar characteristics, it is interesting to note that the depression at the entrance to the channel, clearly visible in *Figures B.5* & *B.8*, no longer stands out. Concerning the *ROI 2*, the apparition of dry areas leads to a sudden increase in speed. Furthermore, by comparing the obtained velocities, it can be seen that they are globally higher in the absence of roughness, meaning the variations induced by the new morphology allowed the roughness on the banks to have a stronger influence than in the initial state

The study of the water depth profiles once the second sediment recharge and the second seven-hour hydrograph have been carried out highlights fairly different behaviour between the two scenarios. In the absence of added bank roughness *(Appendix B.8, Figure B.13)*, the result of the simulation is more homogenized than the result obtained after the first hydrograph. The dry areas are less important, especially in *ROI 1*, and the water depths do not fluctuate by much. The impact of the second sediment supply is way more pronounced in the presence of roughness on the banks *(Appendix B.8, Figure B.17)*. While the downstream portion of the channel near the *riffle2* section shows little change, the *ROI 1* now has a much larger surface area of dry zones. The sinuous patterns previously mentioned deeply increase the complexity of the bed, with the alternating presence of remnants of sediment deposits driving the water towards the other bank. The appearance of more or less complex bed patterns also influences the simulated velocities. In the absence of added roughness on the banks *(Figure 5.3)*, the velocities in the vicinity of the deposition zone are essentially rectilinear and only have limited variability, whereas the *ROI 2* presents a similar pattern to that obtained after a single hydrograph. In the presence of bank roughness *(Figure 5.4)*, the multiple dry areas near the

deposits create a much more varied sinuous profile, consisting of a succession of moderate velocity sections, followed by faster sections.

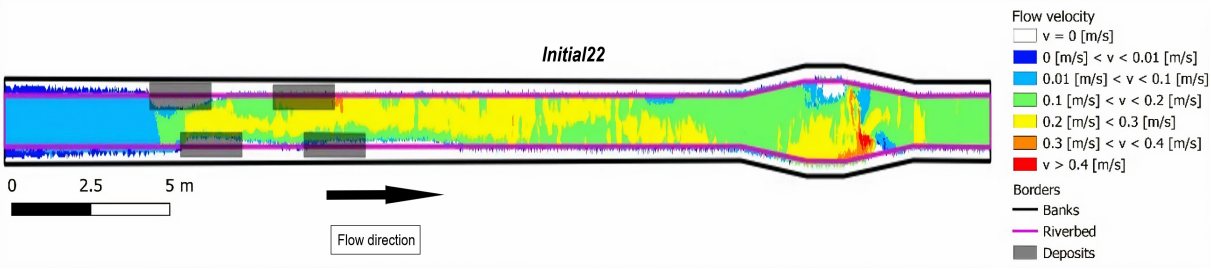

FIGURE 5.3 – Velocities for *Initial22* scenario. The velocity values correspond to the colour code shown. The transparent rectangles represent the initial deposit position. The boundary between the riverbed and the banks is shown as a purple line, while the boundary of the mesh is shown as a black line.

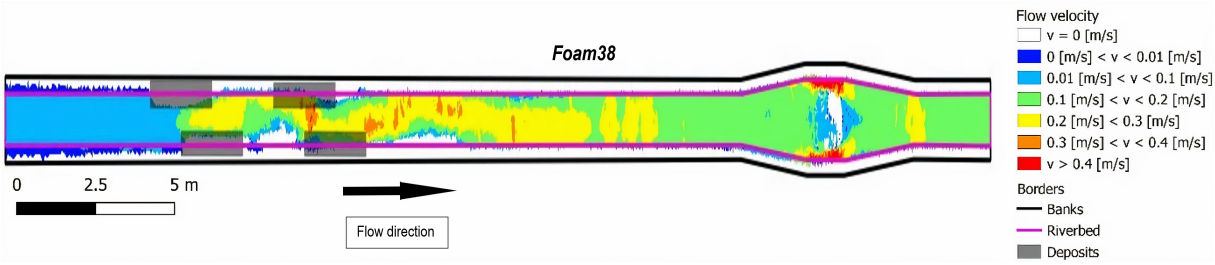

FIGURE 5.4 – Velocities for *Foam38* scenario. The velocity values correspond to the colour code shown. The transparent rectangles represent the initial deposit position. The boundary between the riverbed and the banks is shown as a purple line, while the boundary of the mesh is shown as a black line.

The simulated water heights after a third seven-hour hydrograph are presented in *Appendix B.8*. In the absence of added bank roughness *(Figure B.14)*, the result obtained is relatively similar to that corresponding to the state after the second hydrograph, especially in the *ROI 1*. While the surface corresponding to the most upstream deposit remains dry, the others are progressively wetted. The fact that the area corresponding to the first deposit remains dry is probably due to the low velocity at which the water reaches it, therefore reducing the bedload transport This observation is consistent with the configurations presented in *Appendix B.1*, where it can be seen that the most upstream deposit is more resistant to water than those located downstream. In the *ROI 2*, the dry areas have practically disappeared. The absence of sediment augmentation coupled with the higher bedload transport when no bank roughness is added results in more sediments leaving the physical model, reducing the areas previously made dry by their accumulation. This decrease in dry areas is also observable in the presence of added bank roughness *(Figure B.18)*, where the meandering shapes previously seen in the *ROI 1* have been greatly reduced. While some variability still remains in terms of water heights, a majority of the dry areas shown in *Figure 5.7* are now submerged. The velocity profiles associated with these two scenarios confirm the trend observed for water depths *(Appendix B.7, Figures B.7 & B.10)*.

5.4.2 HMID

The HMID values for the different scenarios were calculated for a residual flow. The surveyed points with a zero water level were not considered. *Table 5.8* presents the HMID values obtained for the different scenarios considered in the absence of added bank roughness, as well as the percentage of variation with respect to the initial state *Initial26*. *Table 5.9* presents the HMID values obtained for the different scenarios considered following the addition of bank roughness, as well as the percentage of variation with respect to the initial state *Foam28*. The HMID results with no added bank roughness are all contained within a range between 3.4 and 4.6. As these values are less than 5, these scenarios can be described as heavily altered. Although the values measured after sediment augmentation remain low, the increase with respect to the initial state is significant, since it ranges from +21 [%] to +36 [%]. The different values of HMID are consistent with the simulations presented in *Section 5.4.1*. As mentioned earlier, the *Initial18* scenario had the most varied range of velocities and water heights, while the *Initial22* and *Initial25* scenarios had relatively similar diversity profiles.

	Initial26	**Initial18**	**Initial22**	**Initial25**
HMID [-]	3.38	4.60	4.10	4.23
Percentage of variation of HMID [%]	-	**+36.1**	**+21.3**	**+25.1**

TABLE 5.8 – HMID results without bank roughness, h > 0 [cm]. The percentage of variation is with respect to the initial state *Intial26*.

The HMID results obtained following the addition of bank roughness are contained within a range of 2.9 to 6.7. If the initial scenario is very altered, the addition of sediments significantly increase the HMID. This large increase is reflected in the rate of change with respect to the initial state, which ranges from +67 [%] to +131 [%]. The comparison of the two configurations - with and without added bank roughness - highlights the increase in the HMID value following the addition of foam on the banks. This is consistent with the results of the numerical simulations presented in *Section 5.4.1*, which show a greater variability of velocities and water depths in the presence of the geonet on the banks. As the *Initial38* scenario had the greatest diversity in velocities and water heights in the numerical simulation, this results in the greatest increase in HMID. Finally, the fact that the *Foam28* scenario has a HMID close to the *Initial26* scenario is related to the low initial water level. As developed previously, low initial water level considerably reduces the impact of the bank roughness with respect to the roughness of the channel bed, minimizing its impact.

	Foam28	**Foam36**	**Foam38**	**Foam39**
HMID [-]	2.94	4.92	6.73	5.62
Percentage of variation of HMID [%]	-	**+67.3**	**+131.0**	**+91.2**

TABLE 5.9 – HMID results with bank roughness, h > 0 [cm]. The percentage of variation is with respect to the initial state *Foam28*.

5.4.3 Shear stress

The flow rate used to study the evolution of the shear stress was set at $Q_{shear} = 50$ [L/s], corresponding to the maximum flow rate in the physical model during the completion of the hydrographs. This choice is also explained by the fact that a residual flow $Q_m = 2$ [L/s] would not have been enough to observe sediment bedload. The results presented in this section were obtained by considering two different sediment diameters, namely $d_m = 6$ [mm] - value corresponding to a diameter greater than or equal to 50 [%] of all diameters counted - and $d_{90} = 7.1$ [mm] - value corresponding to a diameter greater than or equal to 90 [%] of all diameters counted -. The complete particle size curve is presented in *Appendix B.9*, where the blue curve corresponds to the selected particle size. All the numerical simulations performed are presented in *Appendix B.10*. In this regard, it should also be mentioned that the results presented correspond to a simulation time of ten minutes. Although the shear stress values still evolve somewhat at the end of this interval, this time step is the result of a compromise between having sufficiently robust results, while keeping the calculation time acceptable. Finally, as mentioned in *Section 2.3*, it is good to keep in mind that an adimensional shear stress higher than $\tau_* = 0.047$ allows the particles to move.

The reading of the shear stress simulations highlights a first characteristic, namely that the adimensional shear stresses are higher in the case of a diameter d_m compared to a diameter d_{90}. As larger particles are less easily set in motion, this finding is consistent with reality. Furthermore, the comparative reading of the d_m and d_{90} scenarios for the different configurations studied highlights a second fact. If the adimensional shear stresses decrease when considering a diameter d_{90}, these decreases only slightly reduce the proportion of the areas within which the particles will be set in motion. In other words, almost all of the areas in which movement occurred when considering a diameter d_m remain when considering a diameter d_{90}, with the only consequence that the value taken by the adimensionnal shear stress is now closer to the critical value $\tau_{*,cr} = 0.047$.

As a preamble to the analysis, it is worth recalling *equations (1) and (2)* for calculating the shear stress presented in *Section 2.3*. Looking more closely at (1), it can be seen that the shear stress depends on five terms. However, both the diameter considered, the specific weight of the sediments, the specific gravity and the density of the water are constant over the whole channel. The value taken by the dimensionless shear stress therefore only depends on the last parameter, namely the friction velocity. This friction velocity can be related to the flow velocity by means of the *von Karman-Prandtl law of velocity distribution* [98] [99]. Thus, it can be deduced from this observation that the areas within which the flow velocity is higher will have higher frictional velocities, and therefore a higher adimensional shear stress. Similarly, the study of the terms of *equation (2)* indicates that the following parameters are considered in the calculation of τ_* : the diameter d_m or d_{90}, the specific weight of the sediments, the specific gravity, the longitudinal slope of the riverbed and the hydraulic radius. Recalling the slope was assumed to be constant, only the hydraulic radius varies. The adimensional shear stress will therefore vary with the hydraulic radius, meaning that areas of the channel with more wetted surface will have a higher τ_*.

The results modelled with *Basement* are consistent with the predictions developed above. While the different configurations have a relatively similar range within which the adimensional shear stress is greater than the critical value, the value of the shear stress varies in accordance with the results presented in *Section 5.4.1*. Thus, the comparison for a diameter d_m of the initial state *Foam28* presented in *Appendix B.10 (Figure B.28)* with the state *Foam38* presented in *Appendix B.10 (Figure B.32)* illustrates the impact on shear stress of the creation of bed patterns. Indeed, the complexity of the patterns leads to the appearance of areas of more or less rapid velocities in the *ROI 1*, making the value of the adimensional shear stress vary more. As an example, the comparative study of the two above-mentioned figures highlights the appearance of a zone with a τ_* higher than 0.07 (against a value lower than 0.04 in the initial scenario) on the left bank of the *Foam38* scenario at the level of the second deposit, whereas the right bank faces a reduced τ_* value compared to the initial scenario, consequence to lower velocities in this portion. Another interesting fact comes from the comparative study of the results obtained for the initial states *Initial26 (Appendix B.10, Figure B.20)* and *Foam28 (Appendix B.10, Figure B.28)*. While rare variations in water velocities and heights were observed for the initial scenarios in *Section 5.4.1*, the dimensionless shear stress shows some variability, especially on the banks. This observation can be explained by the fact that the flow rate is now 50 [L/s], and not 2 [L/s] as previously, with a consequent greater impact of the bank roughness with respect to the bed roughness.

Looking at the value of the τ_* in the vicinity of the deposits allows to assess the extent to which sediment deposits can be eroded. A first observation is that the two downstream deposits are entirely in a zone where the value of τ_* allows the bedload of sediments, and are thus expected to be eroded. This is confirmed by looking at *Appendix B.1*, where it can be observed that these two deposits have been eroded with respect to the different scenarios. In this regard, it should also be mentioned that although sediments may appear to remain in the presence of added bank roughness, this deception is caused by the fact that some of the sediments remain clinging to the geonet installed on the banks, giving the illusion that some parts of the downstream deposits remain after the hydrograph has passed. On the other hand, only a very small part of the most upstream deposit stands in an erosion zone. This observation is verified in *Appendix B.1* for the different scenarios. An explanation is that, as the deposit is at the end of an upstream section, the water velocity is not sufficient to allow erosion. Finally, concerning the second deposit, its erosion varies significantly according to the configurations studied, going from practically eroded for the scenario *Initial22 (Appendix B.10, Figure B.24)* to a much more moderate erosion for the scenario Foam38 *(Appendix B.10, Figure B.33)*, a finding corroborated by *Appendix B.1*.

Determining the critical flow rate for erosion requires further modelling, which is beyond the scope of this study. Indeed, work carried out on this subject on the Sarine highlighted that an approach based on the hypothesis of a uniform flow is not valid in the presence of sediment replenishment deposits, as this approach does not take the three-dimensional effect of the flow in this zone into account [65]. Finally, the shear strength stress for the transport of sediment of diameter d can be calculated for the two diameters considered. *Using equation (4)* presented in *Section 2.3*, the following values are obtained, namely $\tau_d = 4.65$ $[N/m^2]$ and $\tau_{90} = 5.51$ $[N/m^2]$.

5.4.4 Flood

The discharge chosen for the simulations is $Q_{flood} = 100$ [L/s], this discharge ensuring that the numerical model is not flooded. The results of the simulations for the eight different configurations are presented in *Appendix B.11* (velocities) and in *Appendix B.12* (water heights).

The study of the initial velocity profiles *Initial26* and *Foam28* highlights the influence of the roughness previously developed. In the presence of added roughness *(Appendix B.11, Figure B.40)*, it is possible to note that the roughness will contribute to slow down the water velocity on the banks. Downstream of the *ROI 1*, the velocity measured on the banks can be reduced by more than a half - from 0.62 [m/s] to 0.3 [m/s] - compared to the results obtained without roughness *(Appendix B.11, Figure B.36)*. This decrease in velocities on the banks will contribute to recenter the flow in the channel. The study of the evolution of the water height allows to observe a second impact caused by the presence of added roughness, since it contributes to increase the water height. This finding is particularly visible downstream of the deposits. In this zone where the decrease in velocities can reach a factor of two, the water height can increase by nearly 25 [%] in the presence of added roughness on the banks *(Appendix B.12, Figures B.44 and B.48)*.

These results echo the findings presented in *Section 5.4.1*, namely that the presence of complex bed patterns locally contributes to divert the flow from its usual path. The behaviour in the *ROI 1* describes this dynamic perfectly, with the presence of added roughness on the banks locally creating a sinuous network. This behaviour is also illustrated in the presence of high flow rates as shown in *Figure B.42 (Appendix B.11)*, where the velocity is locally reduced on the right bank after the second deposit, being on the other hand accelerated on the left bank where it increases from 0.23 [m/s] in the initial state to 0.54 [m/s] in this new configuration. These sudden changes in velocities go hand in hand with a great variability in the water height. As the water height remained practically constant between the *ROI 1* and the *ROI 2* in the initial scenario with added bank roughness *(Appendix B.12, Figure B.48)*, the increase in the complexity of the bed disturbs this balance. This pattern can be observed in *Figure B.50 (Appendix B.12)*, with on one hand an overall reduction in water depth symbolised by more green areas, reduction counterbalanced by the appearance of several punctual zones of great water depth. Finally, the absence of added roughness on the banks having created less marked bed structure due to the bedload of more sediments outside of the physical model during hydrographs, the observations presented in the presence of added bank roughness are also found in the absence of added bank roughness, albeit in a less pronounced manner.

5.5 Synthesis

The use of numerical simulation software allowed the exploration of many different scenarios, highlighting the various impacts of bank roughness and bed structure on a wide range of parameters. The study of the velocities and water heights for a residual flow $Q_m = 2$ [L/s] highlighted the influence of the roughness of the banks and the structures of the bed on these two parameters. To this end, particular attention had to be paid to the fact that, due to the low water depth - of the order of 2 [cm] -, the roughness of the banks only had a minimal impact with respect to the roughness of the bed before the first sediment supply. On the other hand, following various sediment inputs and seven-hour hydrographs, the impact of bank roughness and bed structure could be assessed, namely that these two elements allowed a more varied profile of the velocities

and depths of water, in particular by the creation of dry areas and the formation of a sinuous path. According to these observations, the study of the behaviour of velocities as well as water depths in the presence of a simulated flood of $Q_{flood} = 100$ [L/s] offered coherent overall results, making it possible to draw various lessons in terms of flood protection which will be discussed later.

The analysis of the results obtained concerning the evolution of shear stresses for a flow rate of $Q_{shear} = 50$ [L/s] highlighted the erosion and bedload transport areas for the different scenarios. While it was expected that the configuration considering a diameter d_{90} would lead to lower τ_* values than those obtained for a diameter d_m, it could also be observed that the areas within which the erosion and the bedload transport occurred were only minimally impacted. Furthermore, as the slope was assumed to be constant in this study, the calculation of τ_* only depended on the friction velocity - related to the flow velocity by the *Karman-Prandtl law of velocity distribution* - or on the hydraulic radius, according to the equation used. Thus, a strong correlation could be observed between the evolution of water velocities and heights in the physical model and the values of the adimensional shear stresses.

Finally, the HMID calculation gave information about the most favourable conditions from a morphological point of view. Although its value remained relatively low under the different scenarios studied - a coherent observation given the artificial aspect of the physical model - the results obtained once again echoed the conclusions drawn from the study carried out in the presence of a residual flow. Indeed, the formation of bed structures following the supply of sediment to the channel allowed a considerable increase - up to +131 [%] - in the calculated HMID values, particularly in the presence of added roughness on the banks.

6 Discussion

The study [11] carried out in 2016 on a section of the Sarine downstream of the Rossens dam highlighted numerous results relating to the replenishment of watercourses with sediment. Thus, it has been shown that the release of an artificial flood combined with sediment replenishment of the riverbed significantly increase the morphological diversity of a river reach downstream of a storage dam, leading to a significant amelioration in hydraulic habitat suitability [45]. Furthermore, all seemed to indicate that the HMID will be enhanced only in combination with a regularly supply of sediment during the artificial relase of the food. Although very detailed, a research gap was nevertheless mentioned at the end of the study, namely that a long-term field study was still missing, as well as investigations with successive floods releases. Based on this observation and with the help of two models, one physical representing certain characteristics of the Sarine and one numerical, this study set out to answer some of the questions mentioned by *Stähly et al.*.

6.1 Impact of bank roughness and bed structure on morphologic changes

Morphologic changes, like erosion and deposition, vary considerably depending on bank roughness and bed structure in the context of sediment augmentation. This finding was obtained, first by comparing the evolution of the velocity and water depths profile in an existing morphological channel, according to the presence or absence of added roughness on the banks. The analyses carried out on this physical model highlighted the consequences of the installation of a geonet on the banks, with a slowing down of the velocities over the entire lateral profile of the channel - particularly near the banks - coupled with an increase in the water height. This finding is consistent with results already obtained [34], as the added roughness will alter river flow profile, contributing to slowing down the water and resulting in more accumulation as well as in an increase in the measured water depths. Furthermore, although the variation between the velocities measured near the banks and in the center of the channel tends to diminish at high flow rates, this pattern was still apparent in the physical model tests with a flow rate of 80 [L/s], close to the peaks recorded during flood events (100 [L/s]).

The artificial addition of sediments in the physical model revealed a second conclusion regarding the impact of bank roughness, this time relating to deposition. Indeed, considering the scenario where the physical model has no added bank roughness, the top views presented in *Appendix B.1* show that after the first seven-hour hydrograph has been completed, a large majority of the supplied sediments has left the physical model. While the result at the end of the second hydrograph shows that a bit more sediments now remain in the channel, running the third hydrograph again flushes out a significant proportion of sediments. Furthermore, as the water depth study in *Section 5.4.1* indicates, the sediments remaining in the channel are mostly scattered and rarely group into clusters, creating less morphological patterns on the riverbed. The dispersion of sediments follows a different dynamic in the presence of added roughness on the banks of the physical model. Indeed, as the roughness slows down the water velocities, the artificially introduced sediments will be more difficult to transport and will therefore remain in the physical model, with a more varied layout. Another observation is that, while the completion of the second hydrograph following the second sediment replenishment leads to more complex bed patterns, the third hydrograph only moderately disturbs the morphology of the bed, as a large part of the sediments remain in the section studied.

These more complex patterns are illustrated in the simulations presented in *Section 5.4.1*, where the scenarios taking into account the added roughness on the banks present varied water depth profiles, with more dry zones - consequence of clusters created by the accumulation of sediments -, surrounded by areas within which the water depth is higher. Moreover, if the addition of roughness on the banks has at least two different impacts, contributing jointly to influence the hydraulic parameters - velocity and depth of water - and to reduce the transport of sediments, bed structure also plays a key role in the case of sediment augmentation. Indeed, the creation of new patterns on the riverbed also has a strong influence on the profiles of velocity and water depth, as more complex bed patterns will locally decrease the water depth, a decrease compensated by an increase on the other bank of the physical model.

Linking this finding to the previous ones, the first part of this analysis highlighted the close link between velocities, water depths, bed structure and bank roughness in the context of artificial sediment addition. Indeed, the presence of added roughness on the banks will have the consequence of reducing the water velocity and increasing the water depth. As a result, the water flows less quickly and its capacity to transport sediments is reduced, with the consequence that the deposits artificially added to the physical model are less easily mobilised, forming numerous clusters and creating new patterns in the riverbed. Finally, these more complex bed patterns, alternating dry and wet areas, will locally modify water depths and velocities, increasing their variability. Thus, in addition to impacting on the sediment deposition process, bank roughness and bed structure will also impact other processes related to flow velocity and water level, such as erosion.

The study of the evolution of the value of the shear stress showed that the areas of the channel where the water velocity and depth were higher were more prone to erosion. This is particularly illustrated in *Figure B.32 (Appendix B.10)*, where the sinuous patterns created in the vicinity of the deposition area strongly increase the shear stress on the left bank, momentarily reducing it on the right bank, before this process is reversed a few metres downstream. In comparison, *Figure B.24 (Appendix B.10)*, which has a much less sinuous pattern, only presents very small variations in shear stress. This analysis is consistent with the purely mathematical theory of the phenomenon. Indeed, since the shear stress depends on the friction velocity - itself related to the flow velocity by the *Karman-Prandtl law of velocity distribution* - or on the hydraulic radius, an increase in the velocity or in the water depth will impact the value of the shear stress. The values of the shear stress can also be used to assess to assess whether or not the sediment deposits can be eroded. In this study, it was observed that the first deposit was only very superficially eroded *(Appendix B.1)*. As this first deposit is located on the physical model at the end of an ascending section, characterised by lower velocities, this observation corroborates the influence of velocities on the erosion phenomenon.

The observed impact of added bank roughness and bed structure on different morphological processes such as deposition and erosion should allow the development of a strategy to control riverbed changes, such as bed incision or landfill [100]. As a result of progressive or regressive erosion, bed incision refers to a generalized sinking of the river bottom [101]. This sinking will subsequently have numerous consequences, such as the lowering of both the water line and the alluvial water table, with consequences on the supply of drinking water, the drying up of wetlands suddenly disconnected from the water table, the narrowing of the bed increasing the risk of flooding during episodes of high water, or the reduction of the purification capacity of the river [102].

6.2 Effects of bank roughness and bed structure during flood events

The comparative study of the different responses of the physical model during a flood event highlighted the role played by bank roughness and bed structure on flood transit. Indeed, as developed in *Section 6.1*, there is a close link between bank roughness, bed structure, and the two hydraulic parameters of velocity and water height. Hence, the addition of the geonet allows more sediment to be deposited in the physical model, forming better defined bed patterns than without added roughness. This will result in a local reduction in water-carrying capacity, creating areas of varying velocities and water depths. If these variations are limited to the banks in the absence of artificial addition of sediments, the influence is then generalised to a larger portion of the physical model in the presence of sediment deposits.

The impact is particularly visible in the vicinity of the *riffle2* section *(ROI 2)* and in the area of the deposits *(ROI 1)*. Indeed, by comparing the results of *Appendix B.12* obtained with the help of the numerical simulations using *Basement*, it can be seen that the zones of sediment deposition - for example the replenishment sector - will experience a very significant variability in the measured water depths, which can suddenly increase by more than 33 [%] in the presence of marked structures. It should also be noted that the less pronounced bed patterns obtained in the absence of added roughness on the banks locally lead to lower variations, these variations not exceeding 20 [%]. Finally, it should be mentioned that these significant local increases of water depth will have an impact on the overall water levels of the physical model, contributing to its decrease.

The results confirm that the findings developed with respect to the influence of bank roughness and bed structure on the velocity and water depth profiles for a residual flow also apply during the passage of a flood event. Moreover, this influence is also consistent from a theoretical point of view [103]. Indeed, the bigger, smoother and straighter a river, the greater its capacity to carry water and the less prone it is to flooding. On the other side, any process reducing this capacity - in this case the creation of clusters of sediment - contributes to increase flooding. As a component of roughness, vegetation will play a major role during the passage of a flood. By creating zones of obstacles to the flow of water, particularly when vegetation is present within the channel itself, it will slow down the velocity of the flow. As a result, areas of accumulation will be created, increasing the local water depth and the risk of flooding.

Although bank roughness and bed structure have an impact on the behaviour of a flood, they are not the only parameters influencing it. Other characteristics, such as land use or urbanisation, will also play an important role. However, the conclusions of this study open the door to new perspectives in terms of flood protection planning. In the absence of effective flood control structures, such as weirs, it could therefore be possible to take greater advantage of the structure of the watercourse to reduce the risks downstream. Hence, more complex riverbed patterns, which could be obtain by artificially adding sediment deposits, could promote local overflows of the river onto flood-prone land. Discharging part of the flood in pre-determined locations would reduce the volume of water passing through, offering better protection to people and other material assets downstream.

6.3 Effects of different augmentation measures on HMID

Sediment augmentation increases hydro-morphological diversity. If the HMID was initially very low with values close to three, the values obtained after the flood hydrograph following the first supply of sediments show a clear increase, amounting to +36 [%] in the absence of added bank roughness and +67 [%] after the addition of bank roughness. As explained above, the presence of roughness will limit the entrainment of sediments outside the physical model, creating more pronounced bed patterns due to deposition. This will result in more dry areas, balanced by other areas of higher velocity and water height. The increased variability of these two parameters will give them larger standard deviations. Standard deviation - as well as the associated averages - are taken into account in the calculation of the HMID, which will thus see its value increased by the sediment inputs.

The results obtained at the end of the flood hydrograph following the second addition of sediments follow a different pattern, depending on the scenario considered. In the presence of added roughness on the banks, the HMID takes a value 6.73 - corresponding to a partially channelized river -, an increase of +131 [%] compared to the initial state *Foam28* and of +37 [%] compared to the end of the first flood hydrograph. These results illustrate the benefits of a regular supply of sediment on the hydro-morphological diversity of the watercourse. This new supply allows bed patterns to be consolidated, creating a sinuous network in the vicinity of the deposits, which favours the variability of both velocities and water depths. In the absence of added bank roughness, the value of the HMID remains higher than that of the initial state *Initial26* (+21.3 [%]), but is however 11 [%] lower than that calculated at the end of the first hydrograph. To explain this, the simultaneous reading of water depth *(Appendix B.13, Figure B.8)* and velocity *Figure 5.3* values, as well as the *Appendix B.1*, suggests the following hypothesis : if the second sediment replenishment allowed the presence of more sediments in the physical model, the following flood had a strong effect on the bedload transport of the sediments. While the sediments now cover a greater proportion of the physical model, they barely accumulate to form deposits, resulting in less pronounced bed patterns. The relative absence of well-defined patterns reduces the variability of water velocities and depths, as well as the HMID value calculated.

The passage of a third flood hydrograph without sediment augmentation allows to examine the long-term impact of the supply measures. Indeed, the 50 [L/s] injected at the peak of the flood in the physical model correspond to a value largely superior to the residual flow, and are thus associated with relatively rare events. In the absence of bank roughness, the increase compared to the initial state is of the order of 25 [%], a percentage slightly higher than that obtained after the second hydrograph. In the presence of bank roughness, although the calculated value of HMID decreases compared to the previous state (-16 [%]), it is nevertheless established at a threshold that is almost twice as high (+91 [%]) as the initial state.

Although the analysis presented above does not allow for a clear trend to be identified in the absence of added roughness on the banks, it should be remembered that such low roughness is rarely encountered for a river. On the other hand, the results obtained in the presence of added bank roughness show that the supply of sediments to the watercourse allows an improvement - according to the HMID indicator - of the hydro-morphological state of the channel. This finding is consistent with a study of *Stähly et al.* [11]. Moreover, a second sediment augmentation leads to an even more favourable response, highlighting the benefits of multiple augmentation measures on the HMID.

7 Conclusion

The study of the impact of bank roughness and bed structure on a whole range of parameters, including morphological changes (erosion and deposition), diversity index and flood transit during a flood event made it possible to extend some of the conclusions of a study of *Stähly et al.* Two models were used for this purpose, one numerical and one physical. The physical model, an existing morphological channel, firstly provides an initial trend of the impact of added bank roughness on the velocity profile. To this end, two series of measurements were carried out using UVP technology on the physical model. In the first configuration, no roughness was added to the banks, while a geonet was installed on the banks in the second configuration, adding an artificial roughness. Subsequently, the results obtained by means of the physical model were also used to calibrate certain parameters of the numerical model. The numerical model is based on three-dimensional point cloud generated by scans of the physical model, point cloud from which a mesh could then be designed. Finally, the numerical model allowed for the large-scale testing of multiple scenarios, facilitating the comparison of the effects induced by various initial configurations.

The study of the results obtained with the help of numerical simulations firstly highlighted the influence of bank roughness on the deposition of artificial sediment deposits. Indeed, since addition of bank roughness contributes to slow down the flow velocity, the sediments will therefore experience difficulties being bedloaded. As a consequence, they will have a greater tendency to be deposited in the form of small clusters within the physical model, forming more complex patterns on the riverbed. This new situation will create dry zones in several areas of the channel. Moreover, both velocity and water depth profiles will locally encounter significant variations due to the more complex patterns. The creation of more or less rapid zones will therefore have an impact on erosion, increasing the potential for erosion at certain points in the physical model, while greatly reducing it at other points. Furthermore, if the new conditions created by the addition of roughness and the creation of new bed patterns have an influence on various morphological changes, this impact will also be felt in the answer of the physical model during a flood event. Indeed, as the flow is now less homogeneous, several local high water depth areas will appear, opening the door to new perspectives in terms of flood protection planning. Finally, the creation of much more complex patterns due to sediment augmentation induces an improvement of the hydro-morphological state of the watercourse, improvement expressed by increased HMID values.

While the analyses carried out led to a better understanding of the influence of bank roughness and bed structure on various parameters, the results must however be tempered by certain assumptions made, or limitations revealed during the study. Firstly, with respect to the physical model, although the measurements were initially planned using two transducers, only one was finally used, thus depriving the measurements carried out of a self-check. The difficulties encountered in determining the optimal settings for the generation of air bubbles also forced the use of a tracer, namely a quartz powder. Although this tracer was injected 5 [m] upstream of the measurement site, the possible impact of its much higher density than water on the measured values could never been assessed. The exact impact caused by the presence of the *riffle2* section only 3 [m] downstream of the measurement point on the velocities measured could also not be determined. Indeed, the formation of a depression caused by the transport of sediments during the passage of high flow rates could have somewhat distorted the measurements taken subsequently.

The calibration of the roughness of both riverbed and banks must also be assessed with caution. Indeed, although the values obtained with the help of the physical model proved to be of sufficient quality within the framework of this study, they are nonetheless the result of a certain approximation, which it could be interesting to refine in the future to be able to study certain dynamics more closely. Similarly, although the artificially added sediment deposits were given a similar roughness to that of the riverbed, in practice these two values are not equal. Indeed, it is expected that the roughness of the sediments increases with their diameter [104]. The computational limitations encountered during the numerical simulation also constrained certain choices. While the *3DReshaper* software initially provided a three-dimensional point cloud composed of some 280,000 entities, it was finally decided to reduce the number of points to a little less than 20,000 points, to maintain acceptable simulation times. Although this value still represents approximately one coordinate triplet every 5 [cm], this choice has somewhat reduced the accuracy of the elevation model with respect to small elevation variations. Similarly, if the ten-minute results for shear stresses were almost stationary, being able to reproduce these simulations over a longer time interval would have allowed to see if the trend is confirmed over a longer period of time. Finally, although the HMID values obtained suggest a significant improvement in the hydro-morphological state of the river, comparison with other methods, such as *Rapid Bioassessment Protocols*, would allow the improvements obtained to be judged under the prism of other indicators.

8 Bibliography

References

[1] J. Ramirez et al. *Modelling geomorphic responses to human perturbations: Application to the Kander river, Switzerland*. Tech. rep. 2017, pp. 2017–1803.

[2] S. B. Wirth et al. "The sedimentary response to a pioneer geo-engineering project: Tracking the Kander River deviation in the sediments of Lake Thun (Switzerland)". In: *Sedimentology* 58 (2011), pp. 1737–1761.

[3] D. L. Vischer. *Histoire de la protection contre les crues en Suisse*. Tech. rep. Berne: Office fédérale des eaux et de la géologie, 2003.

[4] FOEN. *Hydropower*. 2021. URL: https://www.bfe.admin.ch/bfe/en/home/supply/renewable-energy/hydropower.html.

[5] T. Sayektiningsih and N. Hayati. "Potential impacts of dam construction on environment, society and economy based on community perceptions". In: *IOP Conference Series: Earth and Environmental Science*. 2021.

[6] E. P. Maurer. "Uncertainty in hydrologic impacts of climate change in the Sierra Nevada, California, under two emissions scenarios". In: *Climate Change* 82 (2007), pp. 309–325. DOI: 10.1007/s10584-006-9180-9.

[7] I. Haddeland et al. "Global water resources affected by human interventions and climate change". In: *PNAS* 111.9 (2014), pp. 3251–3256. DOI: 10.1073/pnas.1222475110. URL: www.pnas.org/lookup/suppl/doi:10.1073/pnas.1222475110/-/DCSupplemental.www.pnas.org/cgi/doi/10.1073/pnas.1222475110.

[8] J. A. Stanford et al. "A general protocol for restoration of regulated rivers". In: *Regulated Rivers: Research and Management* 12.4-5 (1996), pp. 391–413.

[9] Y. Yonggui et al. "Effects of dams on water and sediment delivery to the sea by the Huanghe (Yellow River): The special role of Water-Sediment Modulation". In: *Anthropocene* 3 (Nov. 2013), pp. 72–82. ISSN: 2213-3054. DOI: 10.1016/J.ANCENE.2014.03.001.

[10] G. Bussi et al. "Impact of dams and climate change on suspended sediment flux to the Mekong delta". In: *Science of The Total Environment* 755 (Feb. 2021). ISSN: 0048-9697. DOI: 10.1016/J.SCITOTENV.2020.142468.

[11] S. Stähly et al. "Sediment replenishment as a measure to enhance river habitats in a residual flow reach downstream of a dam". In: *Sustainable and Safe Dams Around the World* (2019), pp. 1284–1292.

[12] B. Dargahi. *Encyclopedia of Lakes and Reservoirs*. Ed. by Lars Bengtsson, Reginald W. Herschy and Rhodes W. Fairbridge. 2012.

[13] W. R. White. "Contributing paper flushing of sediments from reservoirs". In: Cape Town, 2000.

[14] J. E. Merz and L. K. Ochikubo Chan. "Effects of gravel augmentation on macroinvertebrate assemblages in a regulated california river". In: *River Research and Applications* 21 (2005), pp. 61–74. DOI: 10.1002/rra.819. URL: www.interscience.wiley.com.

[15] A. J. Rollet et al. “Assessment of consequences of sediment deficit on a gravel river bed downstream of dams in restoration perspectives: application of a multicriteria, hierarchical and spatially explicit diagnosis”. In: *River Rsearch and Applications* 30 (2014), pp. 939–953. DOI: 10.1002/rra.2689.

[16] J. E. Merz et al. “Predicting benefits of spawning-habitat rehabilitation to salmonid (Oncorhynchus spp.) fry production in a regulated California river”. In: *https://doi.org/10.1139/f04-077* 61.8 (Aug. 2004), pp. 1433–1446. ISSN: 0706652X. DOI: 10.1139/F04-077. URL: https://cdnsciencepub.com/doi/abs/10.1139/f04-077.

[17] J. N. N. Egish, M. Inoue and M. N. Unokawa. “Effects of channelisation on stream habitat in relation to a spate and flow refugia for macroinvertebrates in northern Japan”. In: *Freshwater Biology* 47 (2002), pp. 1515–1529.

[18] J. P. L. Johnson and K. X. Whipple. “Evaluating the controls of shear stress, sediment supply, alluvial cover, and channel morphology on experimental bedrock incision rate”. In: *Journal of Geophysical Research Earth Surface* 115.F2 (2010).

[19] L. Vonwiller. “Numerical Modeling of Morphological Response of Gravel-Bed Rivers to Sediment Supply”. PhD thesis. ETH Zurich, 2017.

[20] C. M. Soja and R. Riding. “Silurian Microbial Associations from the Alexander Terrane, Alaska ”. In: *Journal of Paleontology* 67 (1993), pp. 728–738. URL: https://www.jstor.org/stable/1306039?seq=1#metadata_info_tab_contents.

[21] U. Pulg et al. “Restoration of spawning habitats of brown trout (Salmo Trutta) in a regulated chalk stream”. In: *River Research and Applications* 29.2 (2011), pp. 172–182.

[22] B. Jones. “Biogenicity of terrestrial oncoids formed in soil pockets, Cayman Brac, British West Indies”. In: *Sedimentary Geology* 236.1-2 (Apr. 2011), pp. 95–108. ISSN: 00370738. DOI: 10.1016/J.SEDGEO.2010.12.009. URL: https://www.researchgate.net/publication/229293920_Biogenicity_of_terrestrial_oncoids_formed_in_soil_pockets_Cayman_Brac_British_West_Indies.

[23] S. Kantoush et al. “Impacts of sediment flushing on channel evolution and morphological processes: Case study of the Kurobe River, Japan”. In: *River Flow* (2010), pp. 1165–1176. URL: http://henry.baw.de/handle/20.500.11970/99765.

[24] I. Katano et al. “Effects of sediment replenishment on riverbed environments and macroinvertebrate assemblages downstream of a dam”. In: *Scientific Reports* 11 (2021). DOI: 10.1038/s41598-021-86278-z.

[25] C. Mörtl and G. De Cesare. “Sediment Augmentation for River Rehabilitation and Management—A Review”. In: *Land* 10.1309 (2021).

[26] G. Ock, T. Sumi and Y. Takemon. “Sediment replenishment to downstream reaches below dams: implementation perspectives”. In: *Hydrological Research Letters* 7.3 (2013), pp. 54–59. ISSN: 1882-3416. DOI: 10.3178/HRL.7.54. URL: www.jstage.jst.go.jp/browse/hrl.

[27] J. G. Venditti et al. “Effect of sediment pulse grain size on sediment transport rates and bed mobility in gravel bed rivers”. In: *Journal of Geophysical Research Earth Surface* 115.3 (Sept. 2010). ISSN: 21699011. DOI: 10.1029/2009JF001418.

[28] C. Juez et al. “Assessment of the performance of numerical modeling in reproducing a replenishment of sediments in a water-worked channel”. In: *Advances in Water Resources* 92 (June 2016), pp. 10–22. ISSN: 0309-1708. DOI: 10.1016/J.ADVWATRES.2016.03.010.

[29] D. Gaeuman. “Mitigating Downstream Effects of Dams”. In: *Gravel-Bed Rivers: Processes, Tools, Environments* (Feb. 2012), pp. 182–189. DOI: 10.1002/9781119952497.CH16. URL: https://onlinelibrary.wiley.com/doi/full/10.1002/9781119952497.ch16%20https://onlinelibrary.wiley.com/doi/abs/10.1002/9781119952497.ch16%20https://onlinelibrary.wiley.com/doi/10.1002/9781119952497.ch16.

[30] F. Arnaud et al. “Monitoring gravel augmentation in a large regulated river and implications for process-based restoration”. In: *Earth Surface Processes and Landforms* 42.13 (Oct. 2017), pp. 2147–2166. ISSN: 1096-9837. DOI: 10.1002/ESP.4161. URL: https://onlinelibrary.wiley.com/doi/full/10.1002/esp.4161%20https://onlinelibrary.wiley.com/doi/abs/10.1002/esp.4161%20https://onlinelibrary.wiley.com/doi/10.1002/esp.4161.

[31] T. Kang, I. Kimura and Y. Shimizu. “Responses of Bed Morphology to Vegetation Growth and Flood Discharge at a Sharp River Bend”. In: *Water 2018, Vol. 10, Page 223* 10.2 (Feb. 2018), p. 223. ISSN: 20734441. DOI: 10.3390/W10020223. URL: https://www.mdpi.com/2073-4441/10/2/223/htm%20https://www.mdpi.com/2073-4441/10/2/223.

[32] T. Meile. “Influence of macro-roughness of walls on steady and unsteady flow in a channel”. PhD thesis. Lausanne: EPFL, 2007.

[33] C. Noss and A. Lorke. “Roughness, resistance, and dispersion: Relationships in small streams”. In: *Advancing Earth and Space Science* (2016). DOI: https://doi.org/10.1002/2015WR017449.

[34] C. Camporeale et al. “Modeling the Interactions Between River Morphodynamics and Riparian Vegetation”. In: *Reviews of Geophysics* 51.3 (Sept. 2013), pp. 379–414. ISSN: 8755-1209. DOI: 10.1002/ROG.20014. URL: https://ui.adsabs.harvard.edu/abs/2013RvGeo..51..379C/abstract.

[35] A. Vargas-Luna, Al. Crosato and W. S. J. Uijttewaal. “Effects of vegetation on flow and sediment transport: comparative analyses and validation of predicting models”. In: *Earth Surface Processes and Landforms* 40.2 (Feb. 2015), pp. 157–176. ISSN: 1096-9837. DOI: 10.1002/ESP.3633. URL: https://onlinelibrary.wiley.com/doi/full/10.1002/esp.3633%20https://onlinelibrary.wiley.com/doi/abs/10.1002/esp.3633%20https://onlinelibrary.wiley.com/doi/10.1002/esp.3633.

[36] K. Gran and C. Paola. “Riparian vegetation controls on braided stream dynamics”. In: *Water Resources Research* 37.12 (2001), pp. 3275–3283. ISSN: 0043-1397. DOI: 10.1029/2000WR000203. URL: https://experts.umn.edu/en/publications/riparian-vegetation-controls-on-braided-stream-dynamics.

[37] G. E. Grant, F. J. Swanson and M. G. Wolman. “Pattern and origin of stepped-bed morphology in high-gradient streams, Western Cascades, Oregon”. In: *Geological Society of America Bulletin* 102 (1990), pp. 340–352.

[38] J. G. Whittaker and M. N. R. Jaeggi. “Origin of step-pool system in mountain stream”. In: *Journal of Hydraulic Division* 111 (1982), pp. 612–624.

[39] K. Zhang, Z.-Y. Wang and L. Liu. *The effect of riverbed structure on bed load transport in mountain streams*. Tech. rep. Beijing, 2010, pp. 863–870.

[40] T. Zhou and T. Endreny. "The Straightening of a River Meander Leads to Extensive Losses in Flow Complexity and Ecosystem Services". In: *Water* 12.6 (2020).

[41] C. J. Keylock, A. L. Singh and E. Foufoula-Georgiou. "The influence of migrating bed forms on the velocity-intermittency structure of turbulent flow over a gravel bed". In: *Geophysical Research Letters* 40.7 (2013), pp. 1351–1355.

[42] M. Gusman, A. Nazki and R. R. Putra. "The modelling influence of water content to mechanical parameter of soil in analysis of slope stability". In: *Journal of Physics: Conf. Series 1008*. Vol. 1008. 2018. DOI: 10.1088/1742-6596/1008/1/012022.

[43] N. B. Dung et al. "The Role Of Relative Slope Length In Flood Hazard Mapping Using Ahp And Gis (Case Study: Lam River Basin, Vietnam)". In: *GEOGRAPHY, ENVIRONMENT, SUSTAINABILITY* 13.2 (June 2020), pp. 115–123. ISSN: 2542-1565. DOI: 10.24057/2071-9388-2020-48. URL: https://ges.rgo.ru/jour/article/view/1164.

[44] A. M. Elmoustafa. "Weighted normalized risk factor for floods risk assessment". In: *Ain Shams Engineering Journal* 3.4 (Dec. 2012), pp. 327–332. ISSN: 2090-4479. DOI: 10.1016/J.ASEJ.2012.04.001.

[45] S. Stähly et al. "Experiments with sediment replenishment in a residual flow reach: Comparison of field data with laboratory experiments". In: *EDP Sciences* 40 (2018).

[46] *Tableau des rugosités de Manning*. URL: https://sites.uclouvain.be/didacticiel-hydraulique/Lecons/Lecon_II_1/Tableau_n.htm.

[47] S. D. Thorne and D. J. Furbish. "Influences of courase bank roughness on flow within a sharply curved river bend". In: *Geomorphology* 3.12 (1995), pp. 241–257. ISSN: 0169-555X. URL: https://www.infona.pl//resource/bwmeta1.element.elsevier-6e9a2470-eafa-319b-b01f-995f062c22db.

[48] Z.-Y. Wang, J. H. W. Lee and C. S. Melching. "Integrated River Management". In: *River Dynamics and Integrated River Management* (2015), pp. 725–800. DOI: 10.1007/978-3-642-25652-3{_}12. URL: https://www.researchgate.net/publication/312791812_Integrated_River_Management.

[49] P. Wilcock, J. Pitlick and Y. Cui. *Sediment transport primer: estimating bed-material transport in gravel-bed rivers*. Tech. rep. Fort Collins: Department of Agriculture, Forest Service, Rocky Mountain, 2009. URL: http://www.stream.fs.fed.us/publications/software.html..

[50] H. Liu and Y. Lu. *Study of structure formation on riverbed and its relationship with geomorphology*. Tech. rep. Nanjing: Nanjing Hydraulic Research Institute, 2013, pp. 2260–2263. DOI: 10.4028/www.scientific.net/AMM.405-408.2260. URL: www.scientific.net..

[51] T. Ghilardi. *La dynamique des cours d'eau - Formes du lit et résistance à l'écoulement*. Tech. rep. Lausanne: EPFL, 2019.

[52] L. W. McKeen. "Introduction to Fatigue and Tribology of Plastics and Elastomers". In: *Fatigue and Tribological Properties of Plastics and Elastomers* (2010), pp. 1–23. DOI: 10.1016/B978-0-08-096450-8.00001-6.

[53] G. Masselink, M.G. Hughes and J. Knight. *Introduction to Coastal Processes and Geomorphology*. 2nd ed. Hodder Education, 2011, p. 432. ISBN: 1444122401, 9781444122404.

[54] G. Caminha. *The CFL Condition and How to Choose Your Timestep Size — SimScale*. 2019. URL: https://www.simscale.com/blog/2017/08/cfl-condition/.

[55] L. C. Van Rijn. "Unified View of Sediment Transport by Currents and Waves. I: Initiation of Motion, Bed Roughness, and Bed-Load Transport". In: *Journal of Hydraulic Engineering* 133 (2007), pp. 649–667. DOI: 10.1061/ASCE0733-94292007133:6649.

[56] J. Jiang. "Theoretical Model for Shields Diagram and Its Application". In: . *Environmental Engineering Theses and Graduate Student Research* 18 (2019). URL: https://digitalcommons.unl.edu/envengdiss.

[57] B. Gomez. "Bedload transport". In: *Earth-Science Reviews* 31 (1991), pp. 89–132.

[58] M. Cassel et al. "Bedload transport in rivers, size matters but so does shape". In: *Scientific Reports 2021 11:1* 11.1 (Jan. 2021), pp. 1–11. ISSN: 2045-2322. DOI: 10.1038/s41598-020-79930-7. URL: https://www.nature.com/articles/s41598-020-79930-7.

[59] J. Trabucho-Alexandre. "More gaps than shale: erosion of mud and its effect on preserved geochemical and palaeobiological signals". In: *Geological Society* 404 (2015), pp. 251–270. DOI: 10.1144/SP404.10. URL: http://dx.doi.org/10.1144/SP404.10.

[60] K. Holliger. *Hydrogeophysics*. Tech. rep. Lausanne: EPFL, 2020.

[61] W. Gostner and A. J. Schleiss. "Indice hydromorphologique de la diversité". In: *Fiches sur l'aménagement et l'écologie des cours d'eau* 3 (2012).

[62] W. Gostner et al. "The hydro-morphological index of diversity: a tool for describing habitat heterogeneity in river engineering projects". In: *Hydrobiologia* 712 (2013), pp. 43–60. DOI: 10.1007/s10750-012-1288-5.

[63] S. Stähly et al. "Sampling sufficiency for determining hydraulic habitat diversity". In: *Journal of Ecohydraulics* (2018), pp. 130–144. ISSN: 2470-5365. DOI: 10.1080/24705357.2019.1576021. URL: https://www.tandfonline.com/action/journalInformation?journalCode=tjoe20.

[64] W. Gostner. *Classification des cours d'eau naturels - Appréciation de l'état écologique d'un cours d'eau*. Tech. rep. Lausanne: EPFL, 2019.

[65] A. Maître. *Evaluation de l'effet d'une crue artificielle et de l'augmentation de sédiments sur la morphologie dans une rivière avec débit résiduel*. Tech. rep. Lausanne: EPFL, 2017.

[66] W. Gostner and A. J. Schleiss. "Der hydromorphologische Index der Diversität – « eine Messlatte für das ökologische Potenzial von Hochwasserschutzprojekten »". In: *Eau énergie air* 4 (2011), pp. 327–336.

[67] A.J. Schleiss. "Flussbauliche Hochwasserschutzmassnahmen und Verbesserung der Gewässerökologie – Vorschlag eines hydraulischmorphologischen Vielfältigkeitsindexes." In: *Eau énergie air* 7/8 (2005), pp. 195–198.

[68] S. Stähly et al. "Analysis of the sensitivity of the hydromorphological index of diversity, HMID". In: *Proceedings of the 8th International Symposium on Environmental Hydraulics* (2018), pp. 95–98.

[69] Service de l'Environnement de l'Etat de Fribourg. *La Sarine au fil de l'histoire-Guide destiné aux enseignant/es*. 2018.

[70] *Barrage de Rossens — Wikipédia*. URL: https://fr.wikipedia.org/wiki/Barrage_de_Rossens.

[71] *Lac de Schiffenen — Wikipédia*. URL: https://fr.wikipedia.org/wiki/Lac_de_Schiffenen.

[72] Conseil Fédéral. *Ordonnance sur la protection des zones alluviales d'importance nationale (Ordonnance sur les zones alluviales) - Status on 1st November 2017*. Tech. rep. 2017. URL: www.ofev.admin.ch.

[73] Conseil Fédéral. *Loi fédérale sur l'aménagement des cours d'eau - Status on 1st January 2011*. Tech. rep. 2011.

[74] R. Schroff. *Eco-Morphological Evaluation of a Residual Flow Reach Restoration Measure*. Tech. rep. Lausanne: EPFL, 2020.

[75] C. Hauer et al. "The Role of Sediment and Sediment Dynamics in the Aquatic Environment". In: *Riverine Ecosystem Management* (2018), pp. 151–169. DOI: 10.1007/978-3-319-73250-3{_}8. URL: https://link.springer.com/chapter/10.1007/978-3-319-73250-3_8.

[76] D. Felix et al. "Optimization of hydropower plants with respect to fine sediment focusing on turbine switch-offs during floods". In: *IOP Conference Series: Earth and Environmental Science* 49.12 (Nov. 2016). ISSN: 1755-1315. DOI: 10.1088/1755-1315/49/12/122011. URL: https://iopscience.iop.org/article/10.1088/1755-1315/49/12/122011%20https://iopscience.iop.org/article/10.1088/1755-1315/49/12/122011/meta.

[77] G. Schellenberg et al. *Dealing with Sediment: Effects on Dams and Hydropower Generation*. 2017. URL: https://www.hydroreview.com/world-regions/dealing-with-sediment-effects-on-dams-and-hydropower-generation/#gref.

[78] R. A. Brown and G. B. Pasternack. "Engineered channel controls limiting spawning habitat rehabilitation success on regulated gravel-bed rivers". In: *Geomorphology* 97.3-4 (May 2008), pp. 631–654. ISSN: 0169555X. DOI: 10.1016/J.GEOMORPH.2007.09.012. URL: https://escholarship.org/uc/item/90g5t0dr.

[79] D. Tonolla, M. Geilhausen and M. Doering. "Seven decades of hydrogeomorphological changes in a near-natural (Sense River) and a hydropower-regulated (Sarine River) pre-Alpine river floodplain in Western Switzerland". In: *Earth Surface Processes and Landforms* 46.1 (Oct. 2020), pp. 252–266. ISSN: 0197-9337. DOI: 10.1002/ESP.5017. URL: https://digitalcollection.zhaw.ch/handle/11475/20966.

[80] FOEN. *Recharge sédimentaire et érosion maîtrisée des berges*. Tech. rep. 2017, Fiche 7. URL: file:///C:/Users/lpattaro/Downloads/fiche-7-recharge-sedimentaire-et-erosion-maitrisee-des-berges%20.pdf.

[81] M. Jaeggi. *Etude sur l'incidence du barrage de Rossens sur la morphologie fluviale, le charriage et l'évolution future de cette zone alluviale*. Tech. rep. 2002.

[82] E. Battisacco. "Replenishment of sediment downstream of dams: erosion and transport processes". PhD thesis. EPFL, 2016.

[83] E. Hanus et al. *Besoins de valorisation des zones alluviales d'importance nationale - Assainissement du charriage, des débits résiduels, des éclusées. Revitalisation*. Tech. rep. 2018.

[84] W. Wongsaroj et al. “Ultrasonic Measurement of Velocity Profile on Bubbly Flow Using a Single Resonant Frequency”. In: *Proceedings 2018, Vol. 2, Page 549* 2.8 (July 2018), p. 549. ISSN: 2504-3900. DOI: 10.3390/ICEM18-05445. URL: https://www.mdpi.com/2504-3900/2/8/549.

[85] H. Kikura et al. “Development of ultrasonic velocity profile method for two-phase flow measurement”. In: *6th Japanese - European Two-Phase Flow Group Meeting*. 2012.

[86] Y. Takeda. “Velocity profile measurement by ultrasonic doppler method”. In: *Experimental Thermal and Fluid Science* 10.4 (May 1995), pp. 444–453. ISSN: 0894-1777. DOI: 10.1016/0894-1777(94)00124-Q.

[87] Ubertone. *UVP Measurement Principle - User Manual*. Tech. rep. 2021.

[88] *Definition of Carrier Frequency - Gartner Information Technology Glossary*. URL: https://www.gartner.com/en/information-technology/glossary/carrier-frequency.

[89] L. Tan and J. Jiang. “Signal Sampling and Quantization”. In: *Digital Signal Processing (Third Edition)* 2 (2019), pp. 13–58.

[90] Y. Naimi and A. Antar. “Hydrogen Generation by Water Electrolysis”. In: *Advances In Hydrogen Generation Technologies* (Aug. 2018). DOI: 10.5772/INTECHOPEN.76814. URL: https://www.intechopen.com/chapters/60944.

[91] E. Santos, R. Nazmutdinov and W. Schmickler. “Electron transfer at different electrode materials: Metals, semiconductors, and graphene”. In: *Current Opinion in Electrochemistry* 19 (Feb. 2020), pp. 106–112. ISSN: 2451-9103. DOI: 10.1016/J.COELEC.2019.11.003.

[92] D. Kasherman and M. Skyllas-Kazacos. “Effects of anode-cathode distance on the cell potential and electrical bath resistivity in an aluminium electrolysis cell with a sloping TiB2 composite cathode”. In: *Journal of Applied Electrochemistry* 18.6 (Nov. 1988), pp. 863–868. ISSN: 0021891X. DOI: 10.1007/BF01016043.

[93] *Hofmann-voltameter - Openclipart*. URL: https://openclipart.org/detail/17885/hofmannvoltameter.

[94] M. Burckbuchler and S. Fischer. “Towards handheld UVP”. In: *13th International Symposium on Ultrasonic Doppler Methods for Fluid Mechanics and Fluid Engineering*. 2021.

[95] D. Vetsch et al. *System Manuals of BASEMENT*. Tech. rep. Laboratory of Hydraulics, Glaciology and Hydrology (VAW), ETH Zurich, 2021.

[96] R. Van Mol. *Plunge pool rehabilitation with prismatic concrete elements - case study and physical model of Ilarion dam in Greece*. Tech. rep. Lausanne: EPFL, 2021.

[97] V. Heller. “Development of Wave Devices from Initial Conception to Commercial Demonstration”. In: *Comprehensive Renewable Energy* 8 (Jan. 2012), pp. 79–110. DOI: 10.1016/B978-0-08-087872-0.00804-0.

[98] C. Guo, C. Zhang and M. P. Païdoussis. “Modification of Equation of Motion of Fluid-Conveying Pipe for Laminar and Turbulent Flow Profiles”. In: *Seismic Safety Evaluation of Concrete Dams* (Jan. 2013), pp. 221–237. DOI: 10.1016/B978-0-12-408083-6.00010-6.

[99] A. D. Abrahams and N. E. Bergeron. “Estimating shear velocity and roughness length from velocity profiles”. In: *Water Resources Research* 28 (1992), pp. 2155–2158.

[100] L. Schmidt, J. J. Bravard and F. Rey. “Maîtriser les évolutions du lit des cours d’eau (incision, atterrissement, . . .) et mieux gérer les formes fluviales”. In: *Ingénierie écologique appliquée aux milieux aquatiques : Pourquoi ? Comment ?* (2013), pp. 84–93. URL: https://hal.archives-ouvertes.fr/hal-00942298.

[101] J.-P. Bravard. “L’incision des lits fluviaux : du phénomène morphodynamique naturel et réversible aux impacts irréversibles / The incision of river beds : from a natural and reversible morphodynamic phenomenon to irreversible impacts”. In: *Géocarrefour* 69.1 (1994), pp. 5–10. ISSN: 0035-113X. DOI: 10.3406/GEOCA.1994.4231.

[102] N. Landon. *Du constat d’enfoncement du lit fluvial aux actions de recharge sédimentaire : quelles solutions pour une gestion raisonnée de nos cours d’eau ?* Tech. rep. 2007, pp. 28–39. URL: https://halshs.archives-ouvertes.fr/halshs-00279895.

[103] P. Bohorquez and J. D. Del Moral-Erencia. “100 Years of Competition between Reduction in Channel Capacity and Streamflow during Floods in the Guadalquivir River (Southern Spain)”. In: *Remote Sensing* (2017).

[104] J. Allard and P. Chee. “Modélisation du charriage en écoulement fluvial”. In: *La Houille Blanche* 3 (1989). DOI: 10.1051/lhb/1989030. URL: http://www.shf-lhb.orgorhttp://dx.doi.org/10.1051/lhb/1989030.

A Appendix : Experimental Setup

A.1 Longitudinal profile with bank roughness

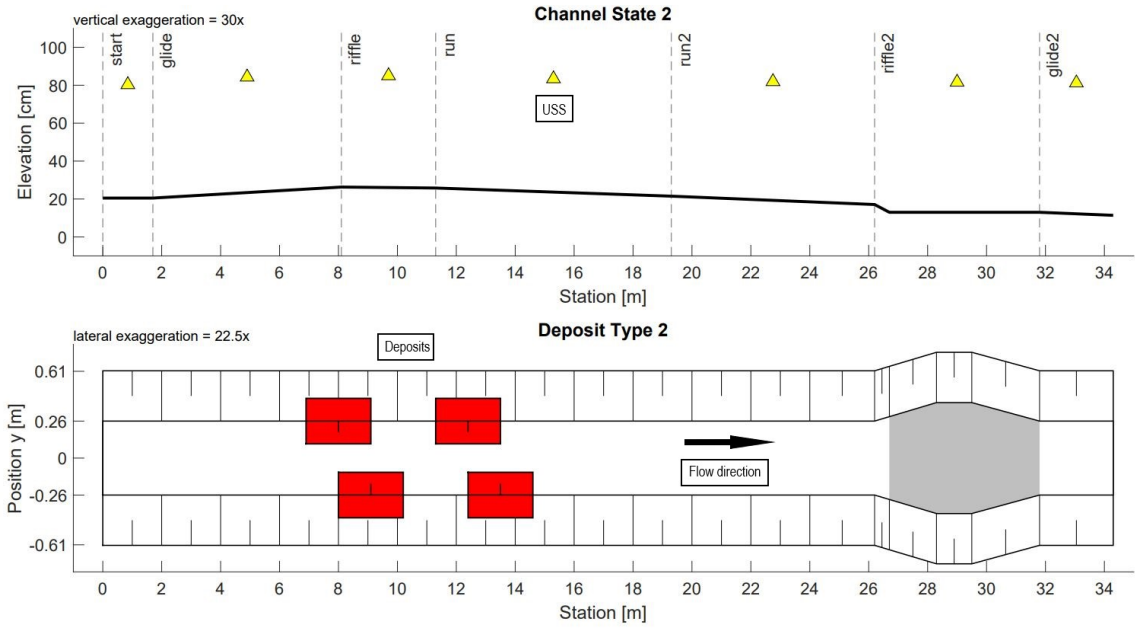

FIGURE A.1 – Schema of the morphological channel with bank roughness. The longitudinal profile of the morphological channel is presented at the top, where yellow triangles corresponds to the USS. A top view of the channel is presented at the bottom, where the red rectangles corresponds to the sediment deposits. The black arrow shows the flow direction.

A.2 Variations of the riverbed along the channel

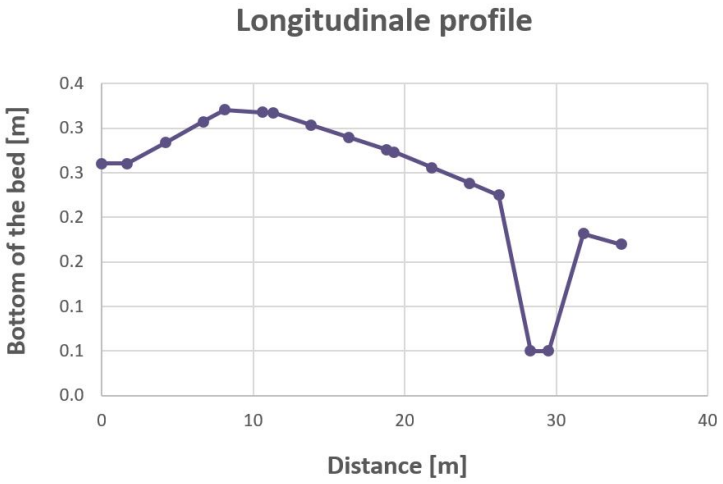

FIGURE A.2 – Longitudinal profile of the morphological channel.

Distance [m]	**Riverbed [m]**
0	0.26
1.70	0.26
4.20	0.28
6.70	0.31
8.10	0.32
10.60	0.32
11.30	0.32
13.80	0.30
16.30	0.29
18.80	0.28
19.30	0.27
21.80	0.26
24.30	0.24
26.20	0.22
28.30	0.05
29.50	0.05
31.80	0.18
34.30	0.17

TABLE A.1 – Variations of the riverbed in the physical model.

A.3 Hydrolysis apparatus

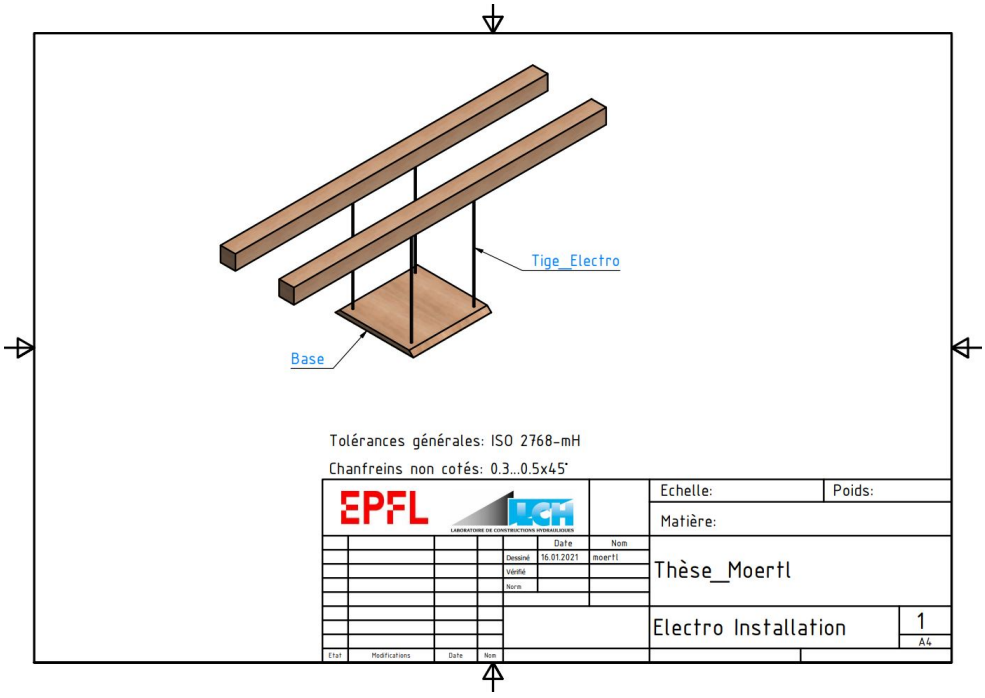

FIGURE A.3 – Hydrolysis apparatus drawings (1).

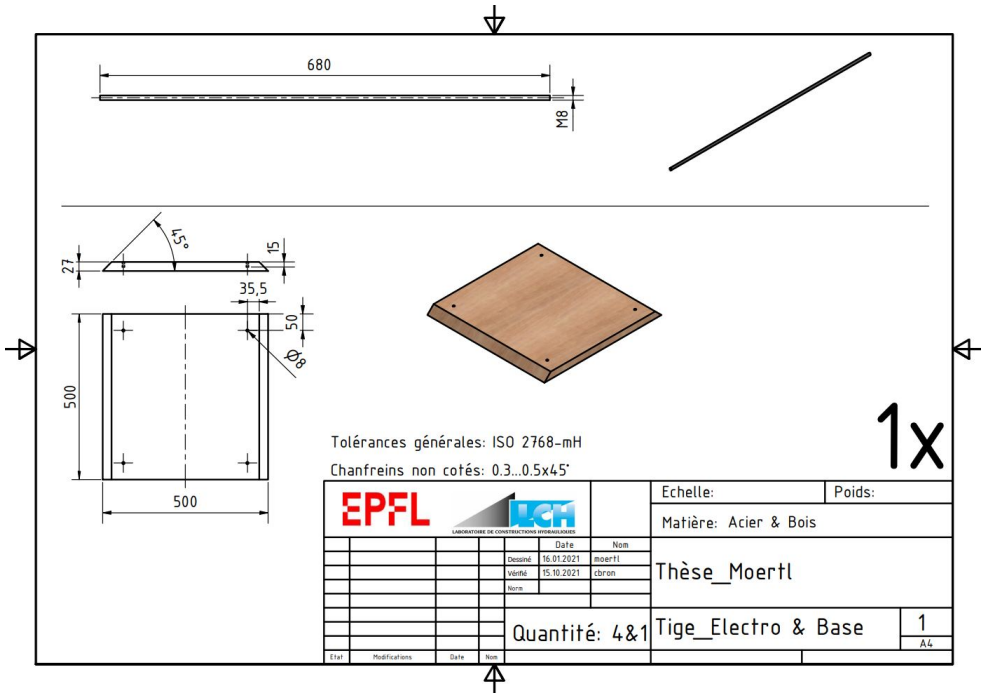

FIGURE A.4 – Hydrolysis apparatus drawings (2).

A.4 UVP

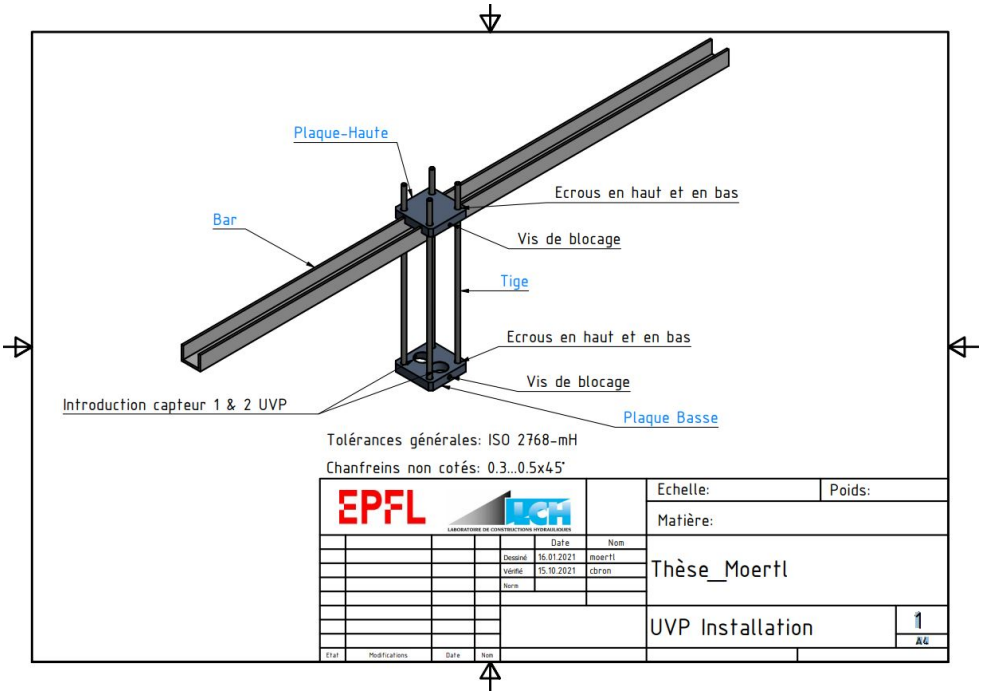

FIGURE A.5 – UVP drawings (1).

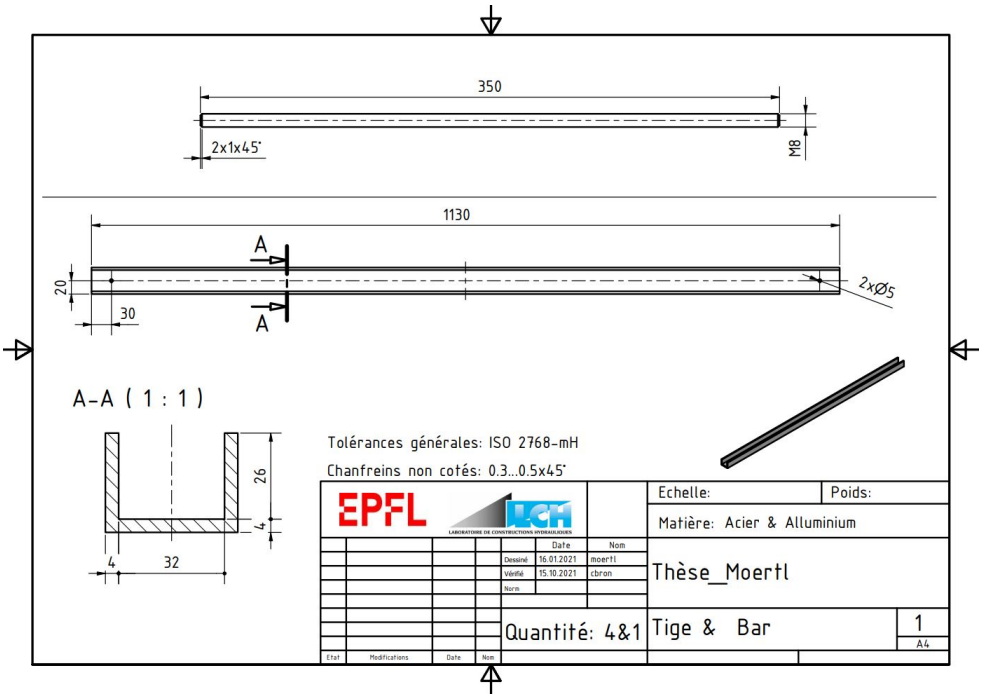

FIGURE A.6 – UVP drawings (2).

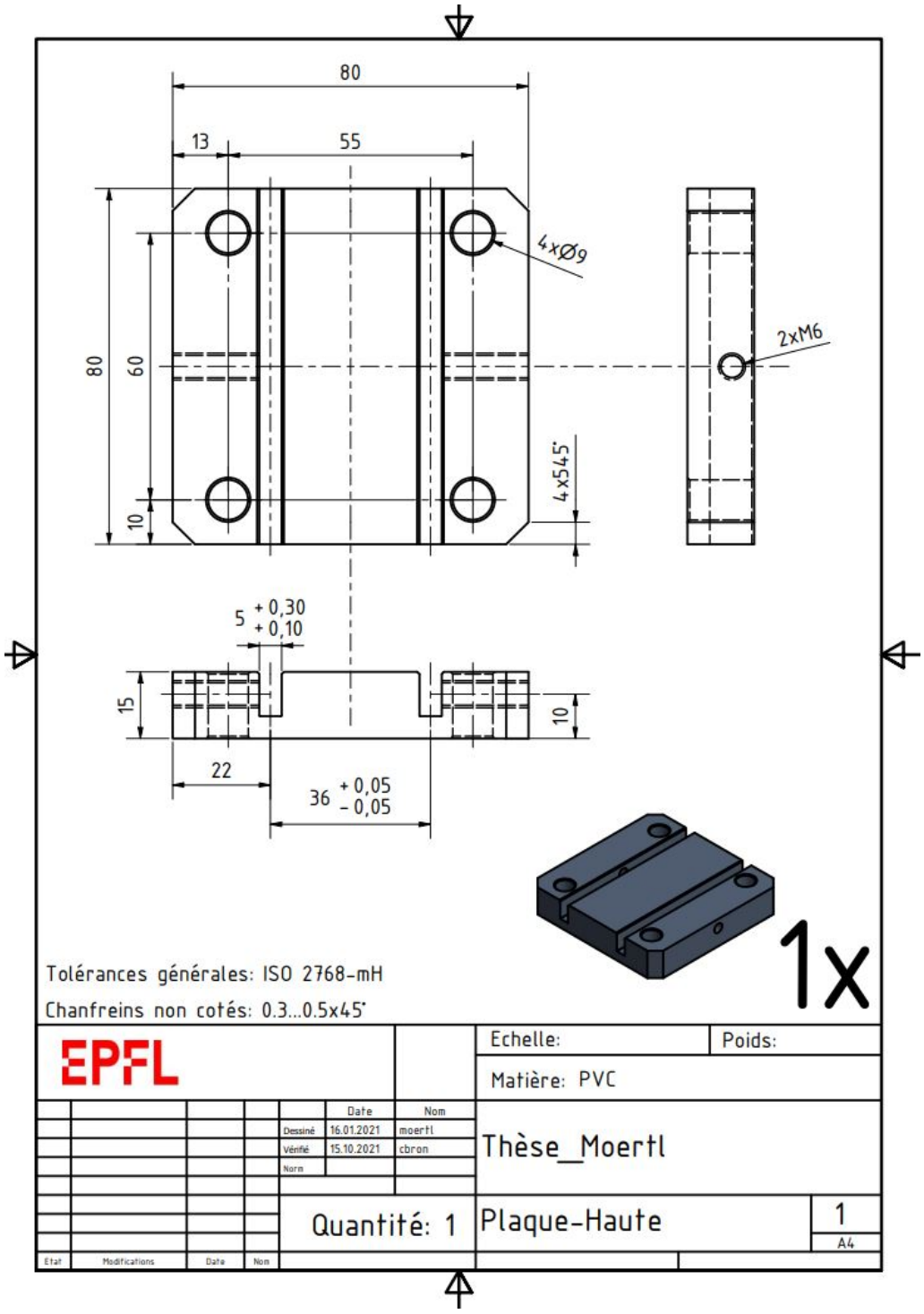

FIGURE A.7 – UVP drawings (3).

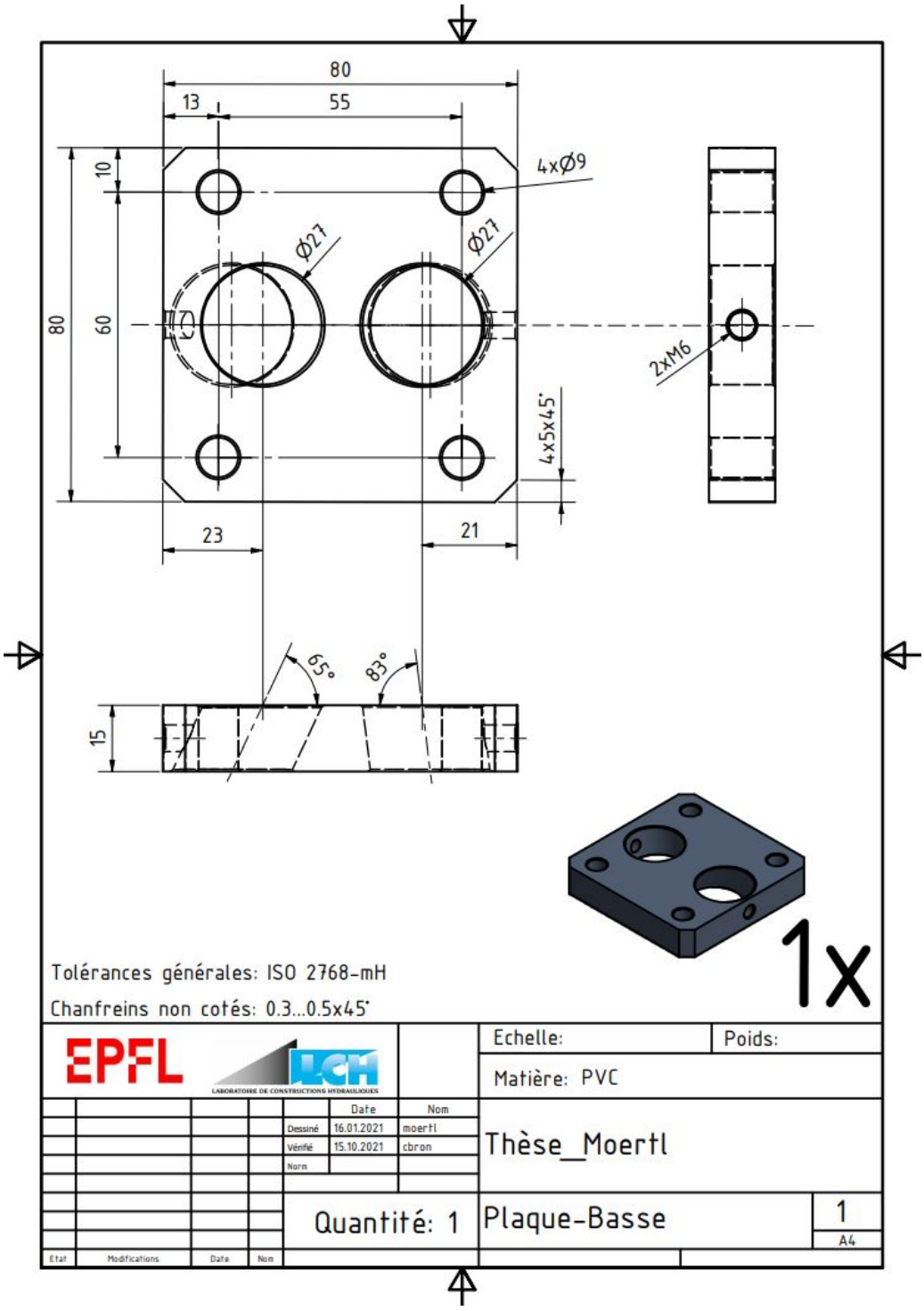

FIGURE A.8 – UVP drawings (4).

A.5 Measurement points

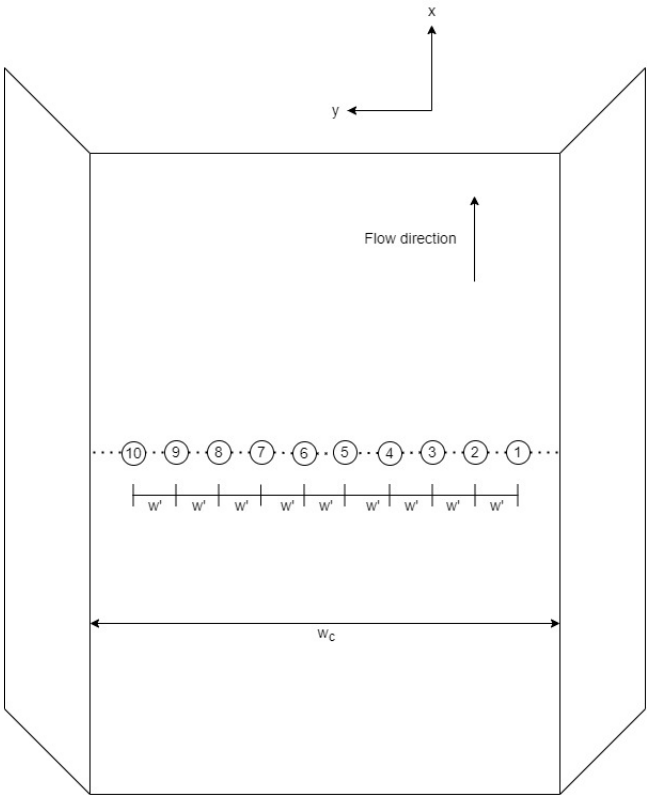

FIGURE A.9 – Schematic representation of measurement points of the horizontal profile, where w_c is the initial channel width and w' is the distance between two measurement points. The black arrow shows the flow direction.

A.6 Parameters used for UVP measurements

Parameter	Description	Value	Unit
Emission frequency	Frequency of the ultrasonic wave sent into the medium	2.00	MHz
Pulse repetition frequency	Repetition frequency of ultrasonic pulse	2000.0	Hz
Expected minimal velocity	Start value for the velocity range	-0.10	m/s
Sample number	Number of pulses to calculate an instantaneous profile	128	-
Profile number per block	Number of profiles to calculate an average	5	-
Position of first cell	Distance to the transducer's surface	7.55	mm
Distance between cells	Distance between two successive cells	1.84	mm
Cell size	Thickness of the measurement cell along acoustic axis	1.84	mm
Cell number	Number of cells in the profile	90	-

Table A.2 – Parameters used for the experiments on the physical model.

Information	Description	Value	Unit
Max. available depth	Max. observable depth when considering the PRF	0.37	m
Measuring window depth	Position of last cell along transducer beam	0.17	m
Max. measurable velocity	Upper limit projected on transducers' axes	0.64	m/s
Measurement block duration	Average profiles stored in files	0.32	s
Sampling rate	Number of samples per second	1.73	Hz

Table A.3 – Displays information for the experiments on the physical model.

A.7 Measured depths

Flow rate [L/s]	**Water depth without roughness [m]**	**Water depth with roughness [m]**
20	0.052	0.060
40	0.078	0.088
60	0.095	0.116
80	0.115	0.139

TABLE A.4 – Measured depth for different flow rates.

A.8 Vertical velocity profiles

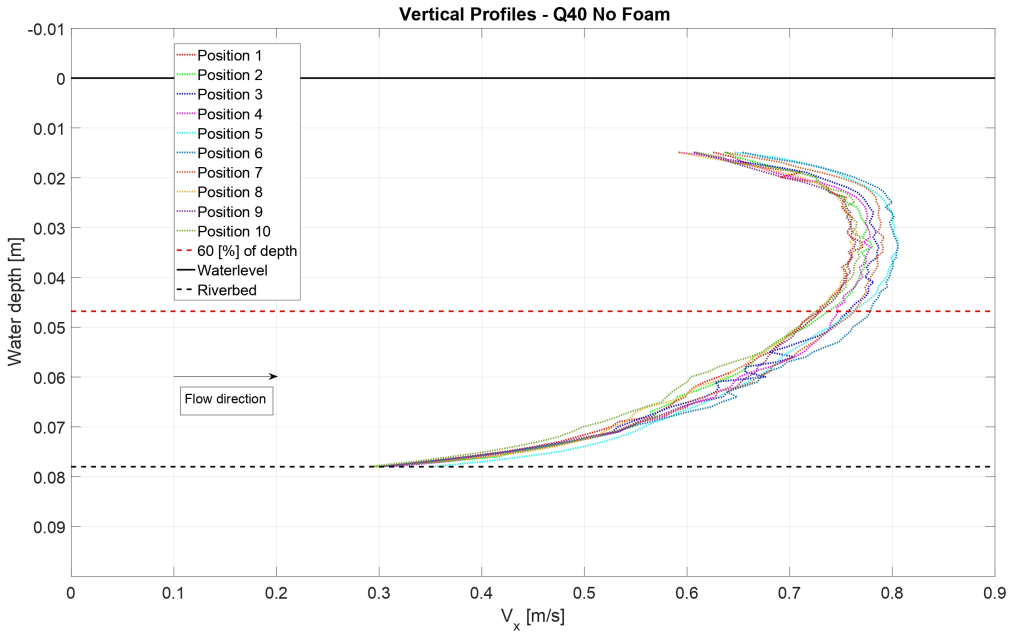

FIGURE A.10 – Vertical profiles for a flow rate of 40 [L/s] at the ten measurement points without foam.

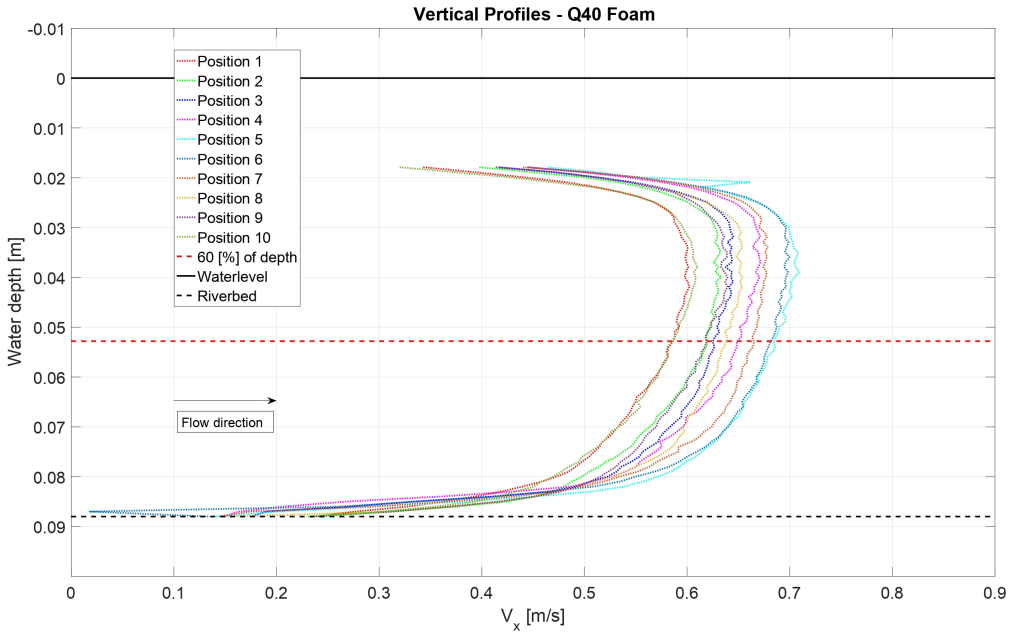

FIGURE A.11 – Vertical profiles for a flow rate of 40 [L/s] at the ten measurement points with foam.

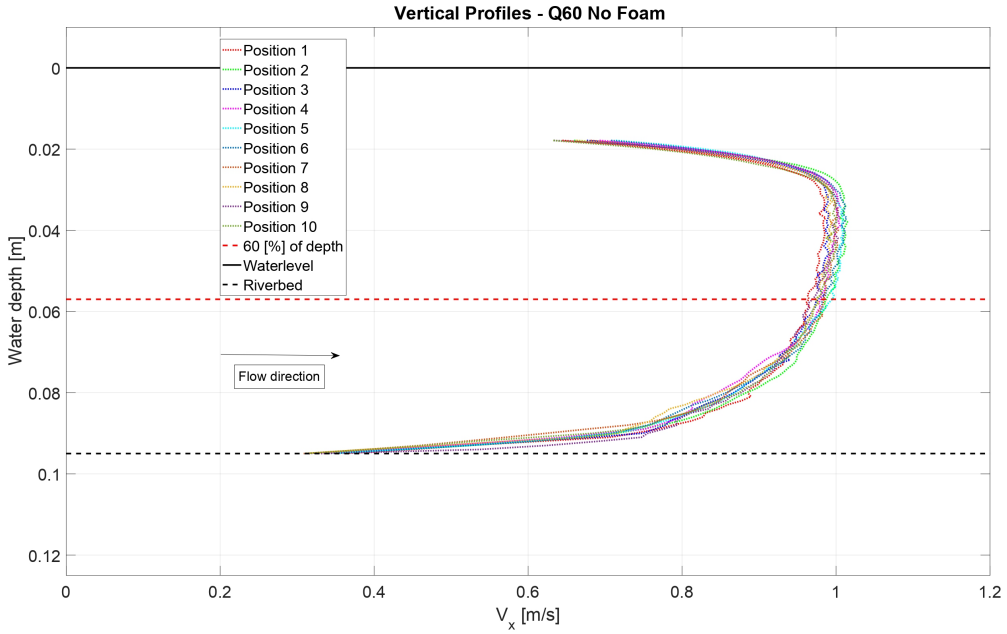

FIGURE A.12 – Vertical profiles for a flow rate of 60 [L/s] at the ten measurement points without foam.

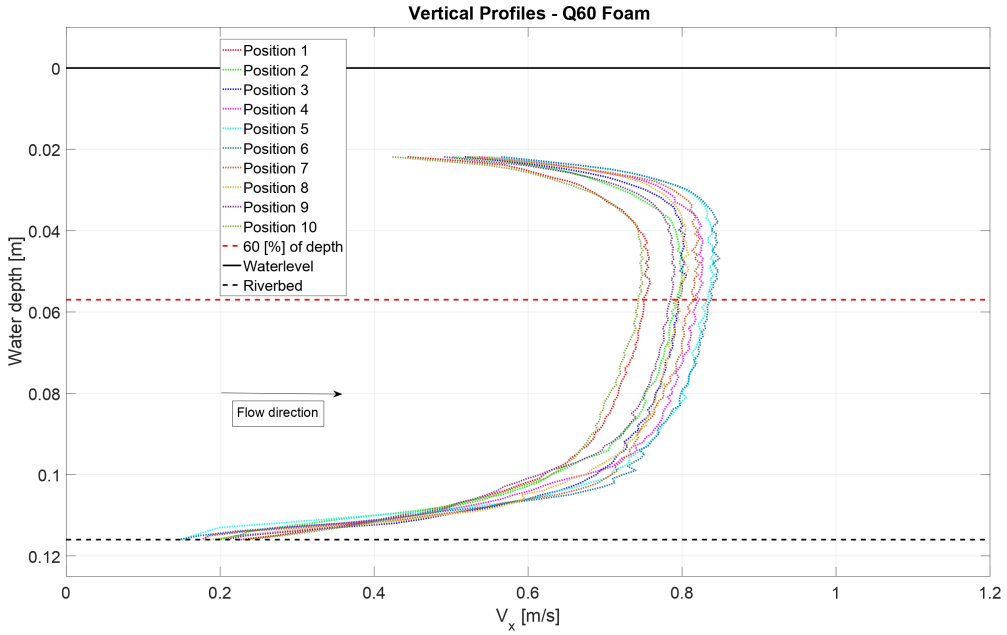

FIGURE A.13 – Vertical profiles for a flow rate of 60 [L/s] at the ten measurement points with foam.

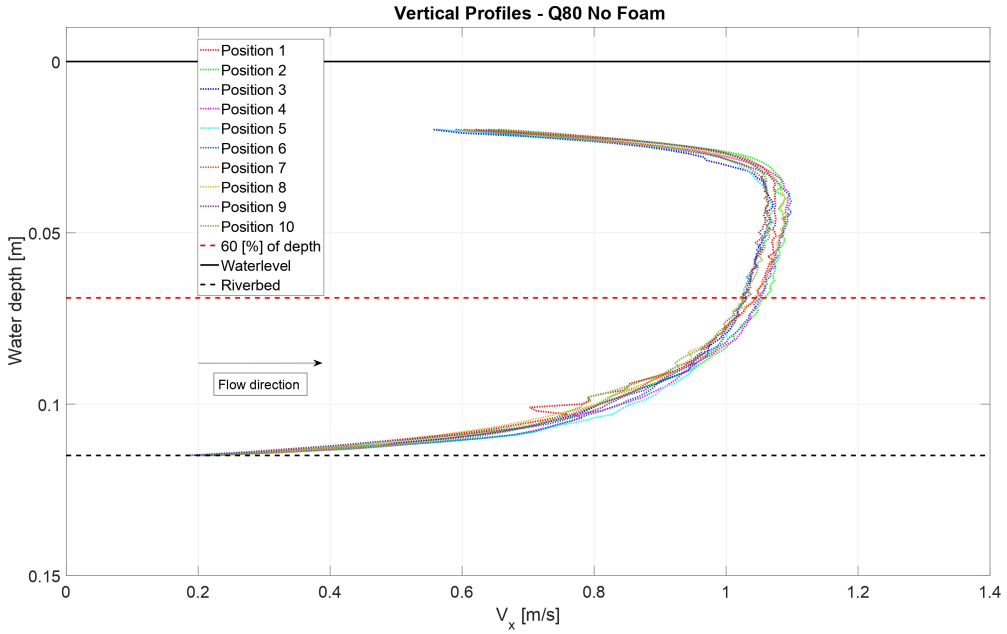

FIGURE A.14 – Vertical profiles for a flow rate of 80 [L/s] at the ten measurement points without foam.

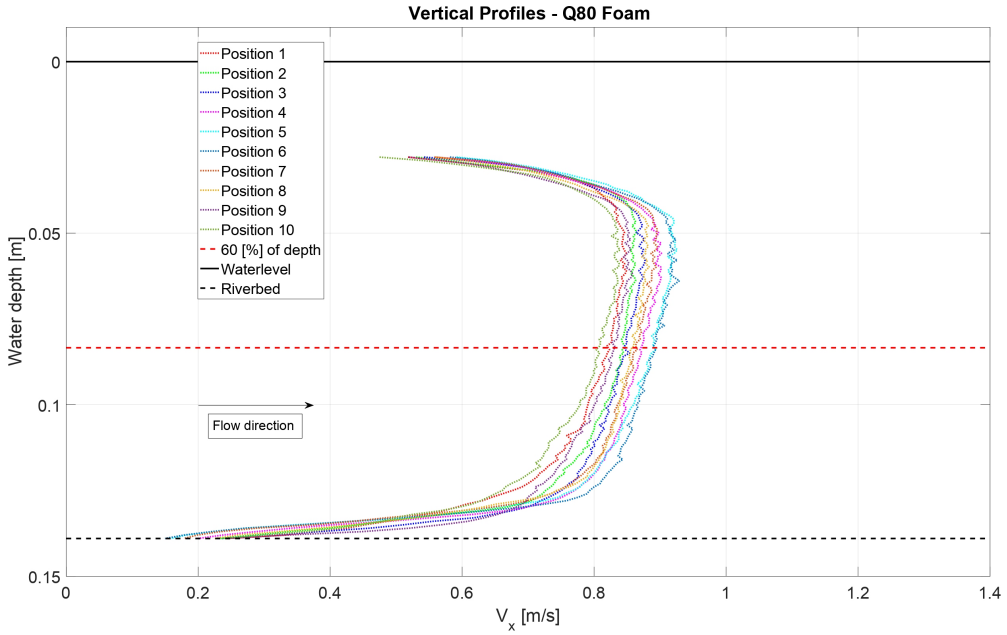

FIGURE A.15 – Vertical profiles for a flow rate of 80 [L/s] at the ten measurement points with foam.

A.9 Average velocities obtained

Position	$\mathbf{V_{UVP,no}}$ **[m/s]**	$\mathbf{V_{micro,no}}$ **[m/s]**	$\mathbf{V_{de,no}}$ **[m/s]**	$\mathbf{V_{UVP,rgh}}$ **[m/s]**
1	0.73	0.75	0.82	0.58
2	0.74	0.77	0.82	0.62
3	0.76	0.76	0.82	0.63
4	0.75	0.78	0.82	0.65
5	0.76	0.75	0.82	0.69
6	0.78	0.77	0.82	0.68
7	0.76	0.79	0.82	0.66
8	0.73	0.76	0.82	0.64
9	0.73	0.75	0.82	0.62
10	0.73	0.74	0.82	0.59

TABLE A.5 – Average velocities obtained at the ten measurement points using UVP technology without added bank roughness, a micro-propeller without added bank roughness, the derived values without added bank roughness and UVP technology with added bank roughness, for $Q = 40$ [L/s].

Position	$\mathbf{V_{UVP,no}}$ **[m/s]**	$\mathbf{V_{micro,no}}$ **[m/s]**	$\mathbf{V_{de,no}}$ **[m/s]**	$\mathbf{V_{UVP,rgh}}$ **[m/s]**
1	0.96	0.95	0.98	0.74
2	0.99	0.96	0.98	0.78
3	0.98	0.95	0.98	0.78
4	0.98	0.97	0.98	0.81
5	0.99	0.96	0.98	0.82
6	0.98	0.97	0.98	0.82
7	0.98	0.99	0.98	0.80
8	0.98	0.96	0.98	0.78
9	0.97	0.97	0.98	0.77
10	0.98	0.95	0.98	0.73

TABLE A.6 – Average velocities obtained at the ten measurement points using UVP technology without added bank roughness, a micro-propeller without added bank roughness, the derived values without added bank roughness and UVP technology with added bank roughness, for $Q = 60$ [L/s].

Position	$\mathbf{V_{UVP,no}}$ **[m/s]**	$\mathbf{V_{micro,no}}$ **[m/s]**	$\mathbf{V_{de,no}}$ **[m/s]**	$\mathbf{V_{UVP,rgh}}$ **[m/s]**
1	1.04	1.06	1.05	0.82
2	1.06	1.05	1.05	0.84
3	1.03	1.07	1.05	0.85
4	1.05	1.04	1.05	0.87
5	1.03	1.05	1.05	0.89
6	1.05	1.08	1.05	0.89
7	1.03	1.06	1.05	0.86
8	1.04	1.05	1.05	0.86
9	1.03	1.07	1.05	0.83
10	1.03	1.06	1.05	0.81

TABLE A.7 – Average velocities obtained at the ten measurement points using UVP technology without added bank roughness, a micro-propeller without added bank roughness, the derived values without added bank roughness and UVP technology with added bank roughness, for $Q = 80$ [L/s].

B Numerical Model

B.1 Configurations studied

The top views presented in this section correspond in descending order to the following scenarios : *Initial26* (1), *Initial18* (2), *Initial22* (3), *Initial25* (4), *Foam28* (5), *Foam36* (6), *Foam38* (7) and *Foam39* (8).

Initial26

Initial18

Initial22

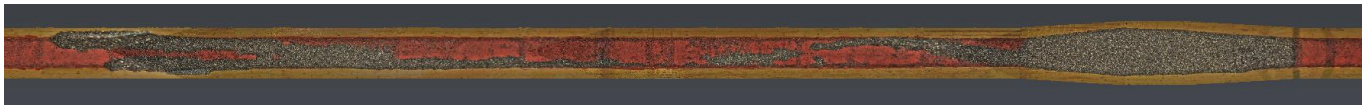

Initial25

Foam28

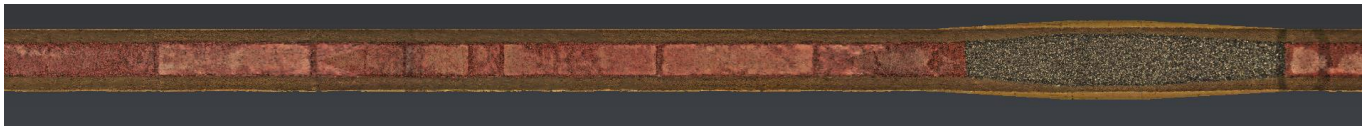

Foam36

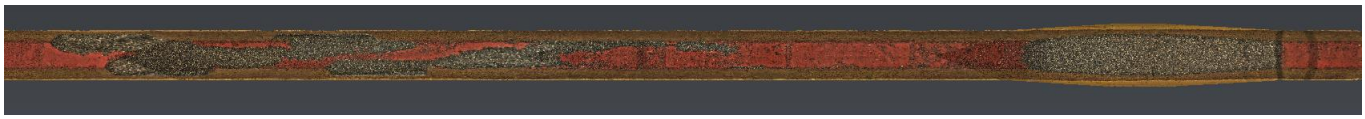

Foam38

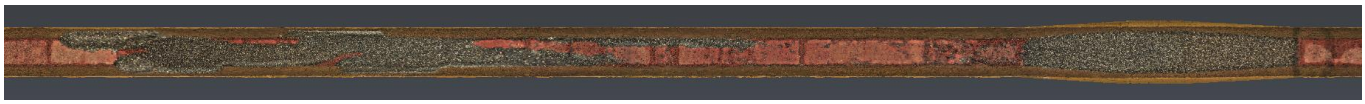

Foam39

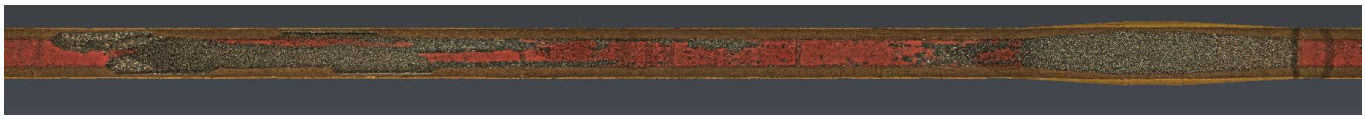

B.2 Cross sections for HMID

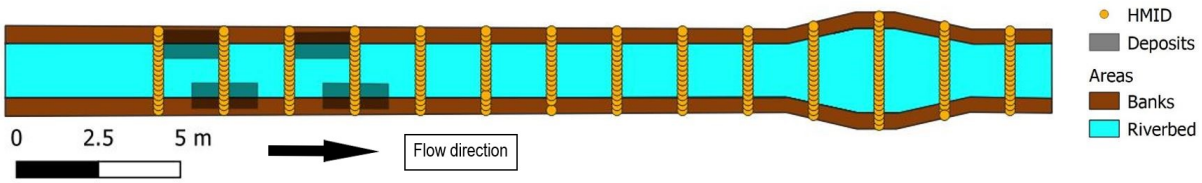

FIGURE B.1 – Cross sections considered to calculate the HMID. The orange dots correspond to the points of measurement, the transparent rectangles corresponds to the deposits, the blue area corresponds to the riverbed and the brown areas correspond to the banks.

B.3 Manning's roughness table

Valeurs du coefficient n de Manning

Nature des surfaces	Etats des parois			
	Parfait	Bon	Assez bon	Mauvais
A) Canaux artificiels				
Ciment lissé	0,01	0,011	0,012	0,013
Mortier de ciment	0,011	0,012	0,013	0,015
Aqueducs en bois raboté	0,01	0,012	0,013	0,014
Aqueducs en bois non raboté	0,011	0,013	0,014	0,015
Canaux revêtus de béton	0,012	0,014	0,016	0,018
Moëllons bruts	0,017	0,02	0,025	0,03
Pierres sèches	0,025	0,03	0.033	0.035
Moëllons dressés	0.013	0.014	0.015	0.017
Aqueducs métalliques à section demi-circulaire lisse	0.011	0.012	0.013	0.015
Aqueducs métalliques à section demi-circulaire plissée	0.0225	0.025	0.0275	0.030
Canaux en terre droits et uniformes	0.017	0.020	0.0225	0.025
Canaux avec pierres, lisses et uniformes	0.025	0.030	0.033	0.035
Canaux avec pierres, rugueux et irréguliers	0.035	0.040	0.045	-
Canaux en terre à larges méandres	0.0225	0.025	0.0275	0.030
Canaux en terre dragués	0.025	0.0275	0.030	0.033
Canaux à fond en terre, côtés avec pierres	0.028	0.030	0.033	0.035
B) Cours d'eau naturels				
1) Propres, rives en ligne droite	0.025	0.0275	0.030	0.033
2) Idem 1 avec quelques herbes et pierres	0.030	0.033	0.035	0.040
3) Avec méandres, avec quelques étangs et endroits peu profonds, propres	0.035	0.040	0.045	0.050
4) Idem 3, l'eau à l'étiage, pente et sections plus faibles	0.040	0.045	0.050	0.055
5) Idem 3, avec quelques herbes et pierres	0.033	0.035	0.040	0.045
6) Idem 4, avec pierres	0.045	0.050	0.055	0.060
7) Zones à eau coulant lentement avec herbes ou fosses très profondes	0.050	0.060	0.070	0.080
8) Zones avec beaucoup de mauvaises herbes	0.075	0.100	0.125	0.150

FIGURE B.2 – Manning's roughness table [46].

B.4 Comparison of water depths and velocities - bed

Measurement point	1	2	3	4	5	6	7	8	9	10
h [m] – Physical Model	0.052	0.052	0.052	0.052	0.052	0.052	0.052	0.052	0.052	0.052
h [m] – k_{30}	0.065	0.065	0.065	0.063	0.060	0.061	0.062	0.062	0.064	0.062
h [m] – k_{40}	0.056	0.056	0.055	0.053	0.050	0.052	0.052	0.053	0.055	0.053
h [m] – k_{50}	0.049	0.048	0.048	0.045	0.043	0.044	0.046	0.046	0.049	0.047

TABLE B.1 – Water depths at $Q = 20$ [L/s] for the ten measurement points.

Measurement point	1	2	3	4	5	6	7	8	9	10
h [m] – Physical Model	0.078	0.078	0.078	0.078	0.078	0.078	0.078	0.078	0.078	0.078
h [m] – k_{30}	0.098	0.098	0.098	0.097	0.093	0.094	0.095	0.095	0.098	0.096
h [m] – k_{40}	0.081	0.081	0.081	0.079	0.076	0.077	0.078	0.079	0.081	0.079
h [m] – k_{50}	0.072	0.070	0.070	0.066	0.064	0.066	0.068	0.069	0.071	0.070

TABLE B.2 – Water depths at $Q = 40$ [L/s] for the ten measurement points.

Measurement point	1	2	3	4	5	6	7	8	9	10
h [m] – Physical Model	0.095	0.095	0.095	0.095	0.095	0.095	0.095	0.095	0.095	0.095
h [m] – k_{30}	0.124	0.124	0.123	0.122	0.118	0.120	0.120	0.121	0.123	0.121
h [m] – k_{40}	0.099	0.098	0.098	0.096	0.093	0.094	0.095	0.095	0.098	0.096
h [m] – k_{50}	0.086	0.083	0.083	0.079	0.078	0.080	0.082	0.084	0.086	0.085

TABLE B.3 – Water depths at $Q = 60$ [L/s] for the ten measurement points.

Measurement point	1	2	3	4	5	6	7	8	9	10
h [m] – Physical Model	0.115	0.115	0.115	0.115	0.115	0.115	0.115	0.115	0.115	0.115
h [m] – k_{30}	0.156	0.156	0.156	0.155	0.151	0.152	0.153	0.153	0.155	0.153
h [m] – k_{40}	0.123	0.123	0.122	0.120	0.117	0.118	0.119	0.120	0.122	0.120
h [m] – k_{50}	0.105	0.103	0.103	0.099	0.098	0.099	0.101	0.102	0.104	0.103

TABLE B.4 – Water depths at $Q = 80$ [L/s] for the ten measurement points.

Measurement point	1	2	3	4	5	6	7	8	9	10
v [m/s] – Physical Model	0.63	0.63	0.63	0.63	0.63	0.62	0.63	0.63	0.63	0.63
v [m/s] – $\mathbf{k_{30}}$	0.51	0.53	0.53	0.55	0.55	0.55	0.54	0.54	0.53	0.51
v [m/s] – $\mathbf{k_{40}}$	0.58	0.61	0.61	0.64	0.63	0.63	0.62	0.61	0.59	0.57
v [m/s] – $\mathbf{k_{50}}$	0.63	0.69	0.69	0.74	0.72	0.72	0.70	0.69	0.67	0.63

TABLE B.5 – Velocities at $Q = 20$ [L/s] for the ten measurement points.

Measurement point	1	2	3	4	5	6	7	8	9	10
v [m/s] – Physical Model	0.73	0.74	0.76	0.75	0.76	0.78	0.76	0.73	0.73	0.73
v [m/s] – $\mathbf{k_{30}}$	0.63	0.66	0.66	0.68	0.67	0.67	0.67	0.67	0.65	0.62
v [m/s] – $\mathbf{k_{40}}$	0.75	0.79	0.79	0.82	0.81	0.81	0.80	0.79	0.77	0.73
v [m/s] – $\mathbf{k_{50}}$	0.83	0.89	0.90	0.94	0.92	0.91	0.89	0.87	0.85	0.79

TABLE B.6 – Velocities at $Q = 40$ [L/s] for the ten measurement points.

Measurement point	1	2	3	4	5	6	7	8	9	10
v [m/s] – Physical Model	0.96	0.99	0.98	0.98	0.99	0.98	0.98	0.98	0.97	0.98
v [m/s] – $\mathbf{k_{30}}$	0.74	0.76	0.76	0.78	0.78	0.78	0.77	0.77	0.76	0.74
v [m/s] – $\mathbf{k_{40}}$	0.91	0.95	0.95	0.97	0.97	0.97	0.96	0.95	0.94	0.90
v [m/s] – $\mathbf{k_{50}}$	1.01	1.09	1.10	1.13	1.12	1.11	1.08	1.07	1.05	0.98

TABLE B.7 – Velocities at $Q = 60$ [L/s] for the ten measurement points.

Measurement point	1	2	3	4	5	6	7	8	9	10
v [m/s] – Physical Model	1.04	1.06	1.03	1.05	1.03	1.05	1.03	1.04	1.03	1.03
v [m/s] – $\mathbf{k_{30}}$	0.83	0.84	0.85	0.85	0.86	0.86	0.85	0.85	0.85	0.83
v [m/s] – $\mathbf{k_{40}}$	1.03	1.06	1.06	1.08	1.08	1.08	1.07	1.06	1.05	1.02
v [m/s] – $\mathbf{k_{50}}$	1.16	1.22	1.23	1.27	1.25	1.25	1.23	1.22	1.20	1.15

TABLE B.8 – Velocities at $Q = 80$ [L/s] for the ten measurement points.

B.5 Comparison of velocities - banks

Measurement point	1	2	3	4	5	6	7	8	9	10
v [m/s] – Physical Model	0.45	0.50	0.51	0.53	0.55	0.55	0.54	0.52	0.50	0.45
v [m/s] – k_{20}	0.41	0.45	0.47	0.48	0.49	0.50	0.49	0.47	0.46	0.42
v [m/s] – k_{25}	0.46	0.50	0.52	0.54	0.55	0.55	0.54	0.53	0.52	0.47
v [m/s] – k_{30}	0.53	0.56	0.58	0.59	0.60	0.60	0.57	0.57	0.55	0.52

TABLE B.9 – Velocities at $Q = 20$ [L/s] for the ten measurement points.

Measurement point	1	2	3	4	5	6	7	8	9	10
v [m/s] – Physical Model	0.58	0.62	0.63	0.65	0.69	0.68	0.66	0.64	0.62	0.59
v [m/s] – k_{20}	0.50	0.53	0.55	0.56	0.59	0.58	0.57	0.57	0.54	0.51
v [m/s] – k_{25}	0.61	0.64	0.66	0.67	0.69	0.70	0.68	0.65	0.63	0.59
v [m/s] – k_{30}	0.65	0.69	0.71	0.73	0.74	0.74	0.73	0.71	0.70	0.67

TABLE B.10 – Velocities at $Q = 40$ [L/s] for the ten measurement points.

Measurement point	1	2	3	4	5	6	7	8	9	10
v [m/s] – Physical Model	0.74	0.78	0.78	0.81	0.82	0.82	0.80	0.78	0.77	0.73
v [m/s] – k_{20}	0.65	0.67	0.67	0.68	0.70	0.69	0.69	0.67	0.66	0.64
v [m/s] – k_{25}	0.77	0.79	0.80	0.82	0.83	0.82	0.80	0.80	0.78	0.75
v [m/s] – k_{30}	0.83	0.84	0.86	0.86	0.87	0.88	0.87	0.85	0.84	0.82

TABLE B.11 – Velocities at $Q = 60$ [L/s] for the ten measurement points.

Measurement point	1	2	3	4	5	6	7	8	9	10
v [m/s] – Physical Model	0.82	0.84	0.85	0.87	0.89	0.89	0.86	0.86	0.83	0.81
v [m/s] – k_{20}	0.70	0.72	0.73	0.73	0.75	0.74	0.75	0.73	0.71	0.69
v [m/s] – k_{25}	0.84	0.85	0.86	0.86	0.88	0.88	0.87	0.87	0.84	0.82
v [m/s] – k_{30}	0.87	0.89	0.91	0.91	0.92	0.92	0.90	0.90	0.89	0.87

TABLE B.12 – Velocities at $Q = 80$ [L/s] for the ten measurement points.

B.6 Areas represented and regions of interest

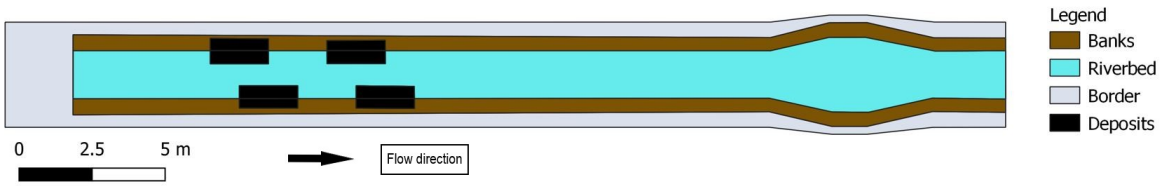

FIGURE B.3 – Areas of the channel represented in the numerical simulations. The grey area corresponds to the entire physical model, the brown areas correspond to the banks, the blue area corresponds to the riverbed and the black rectangles correspond to the sediment deposits.

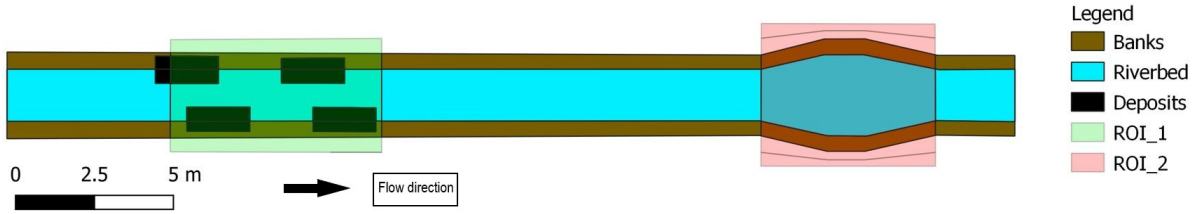

FIGURE B.4 – Location of the two regions of interest. The brown areas correspond to the banks, the blue area corresponds to the riverbed and the black rectangles correspond to the sediment deposits. The green rectangle refers to the upstream region of interest, while the red rectangle refers to the downstream region of interest.

B.7 Velocity profiles - Residual flow

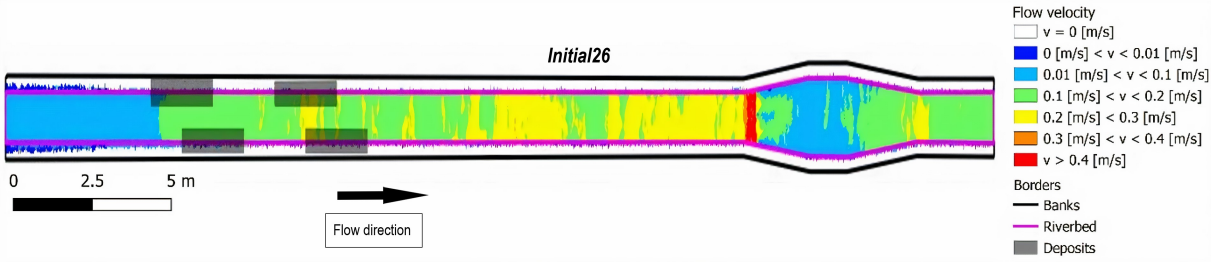

FIGURE B.5 – Velocities for *Initial26* scenario. The velocity values correspond to the colour code shown. The transparent rectangles represent the initial deposit position. These rectangles are only shown to facilitate the interpretation of the results, as no sediment was added in the initial state. The boundary between the riverbed and the banks is shown as a purple line, while the boundary of the mesh is shown as a black line.

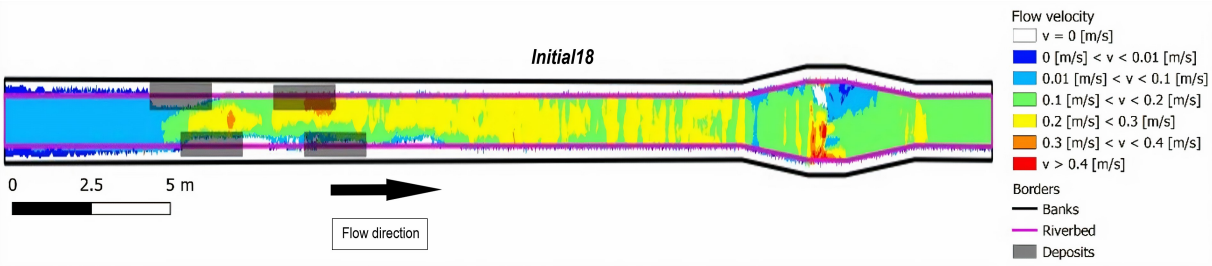

FIGURE B.6 – Velocities for *Initial18* scenario. The velocity values correspond to the colour code shown. The transparent rectangles represent the initial deposit position. The boundary between the riverbed and the banks is shown as a purple line, while the boundary of the mesh is shown as a black line.

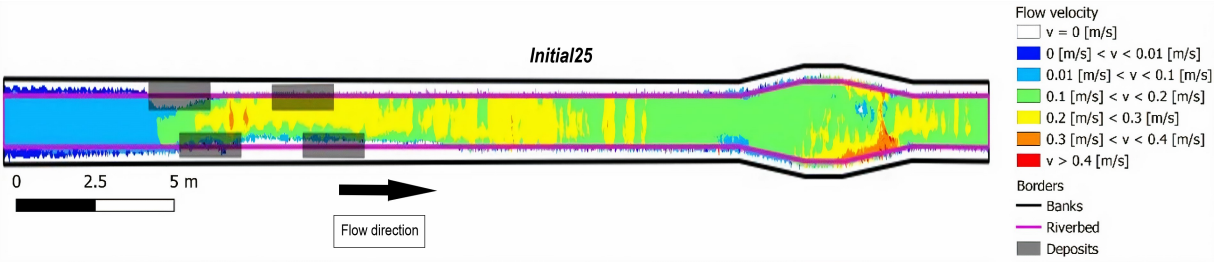

FIGURE B.7 – Velocities for *Initial25* scenario. The velocity values correspond to the colour code shown. The transparent rectangles represent the initial deposit position. The boundary between the riverbed and the banks is shown as a purple line, while the boundary of the mesh is shown as a black line.

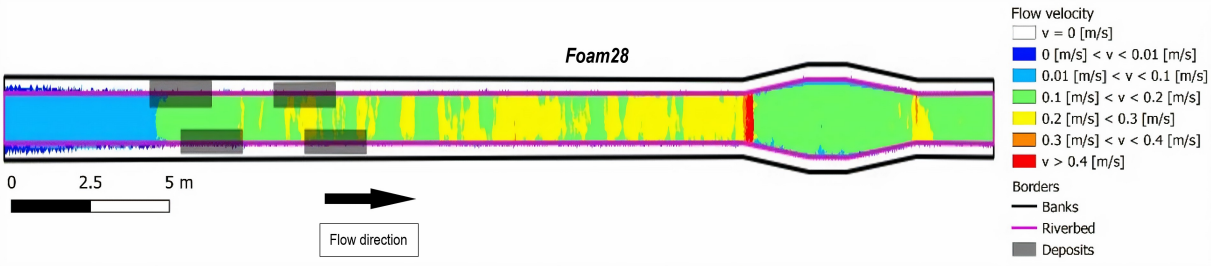

FIGURE B.8 – Velocities for *Foam28* scenario. The velocity values correspond to the colour code shown. The transparent rectangles represent the initial deposit position. These rectangles are only shown to facilitate the interpretation of the results, as no sediment was added in the initial state. The boundary between the riverbed and the banks is shown as a purple line, while the boundary of the mesh is shown as a black line.

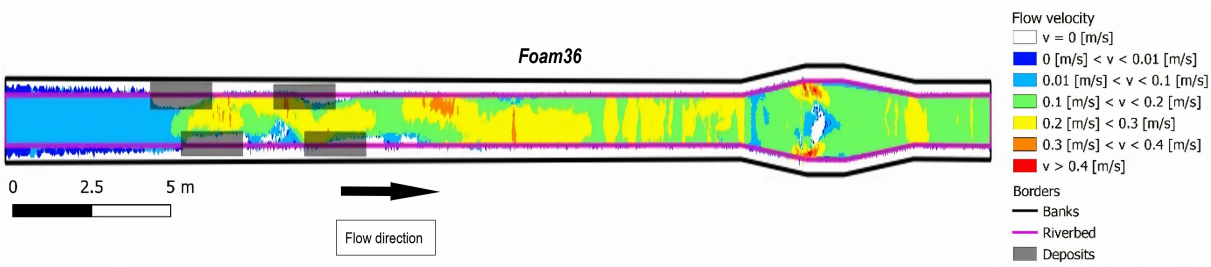

FIGURE B.9 – Velocities for *Foam36* scenario. The velocity values correspond to the colour code shown. The transparent rectangles represent the initial deposit position. The boundary between the riverbed and the banks is shown as a purple line, while the boundary of the mesh is shown as a black line.

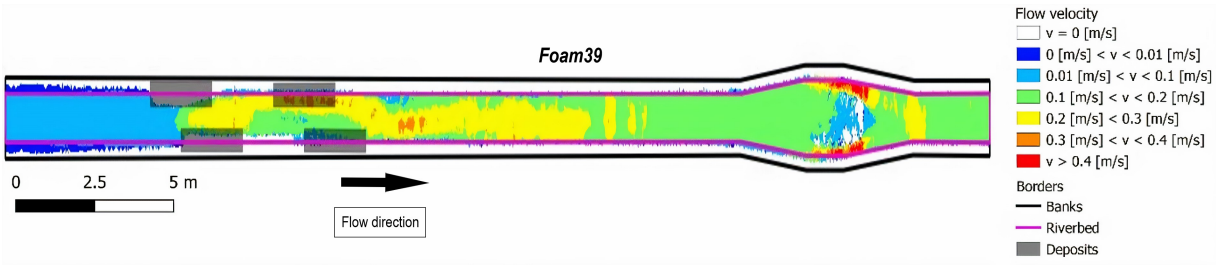

FIGURE B.10 – Velocities for *Foam39* scenario. The velocity values correspond to the colour code shown. The transparent rectangles represent the initial deposit position. The boundary between the riverbed and the banks is shown as a purple line, while the boundary of the mesh is shown as a black line.

B.8 Water depth profiles - Residual flow

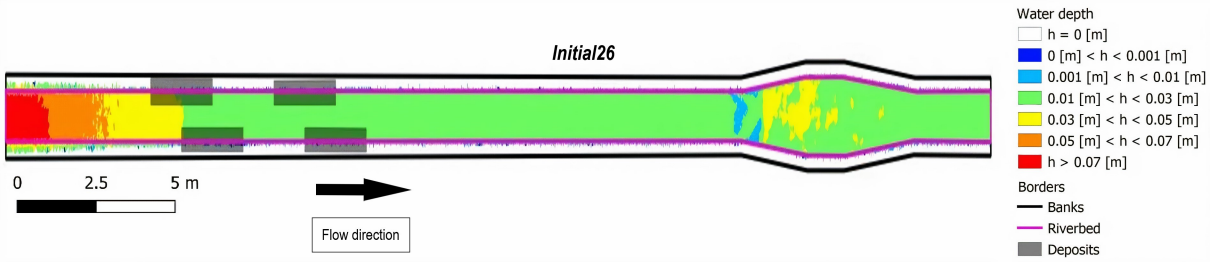

FIGURE B.11 – Water depths for *Initial26* scenario. The water depths correspond to the colour code shown. The transparent rectangles represent the initial deposit position. These rectangles are only shown to facilitate the interpretation of the results, as no sediment was added in the initial state. The boundary between the riverbed and the banks is shown as a purple line, while the boundary of the mesh is shown as a black line.

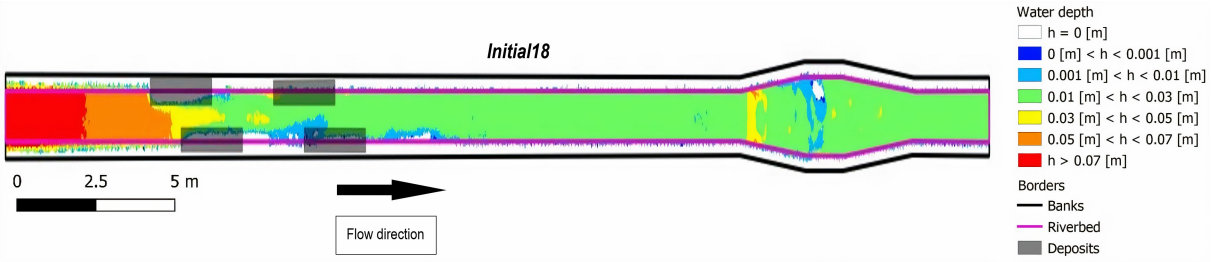

FIGURE B.12 – Water depths for *Initial18* scenario. The water depths correspond to the colour code shown. The transparent rectangles represent the initial deposit position. The boundary between the riverbed and the banks is shown as a purple line, while the boundary of the mesh is shown as a black line.

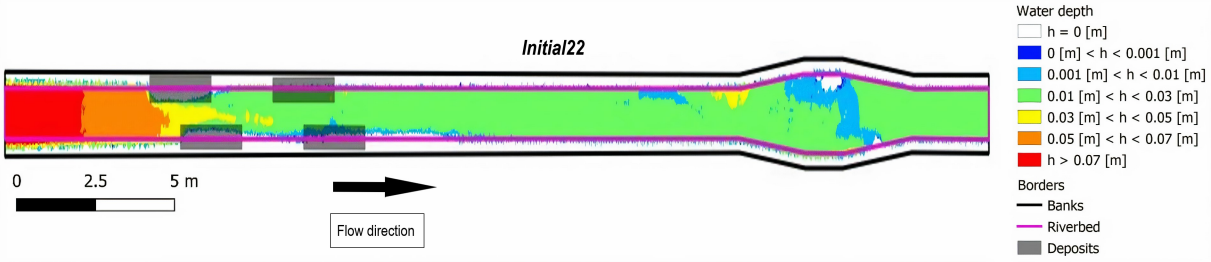

FIGURE B.13 – Water depths for *Initial22* scenario. The water depths correspond to the colour code shown. The transparent rectangles represent the initial deposit position. The boundary between the riverbed and the banks is shown as a purple line, while the boundary of the mesh is shown as a black line.

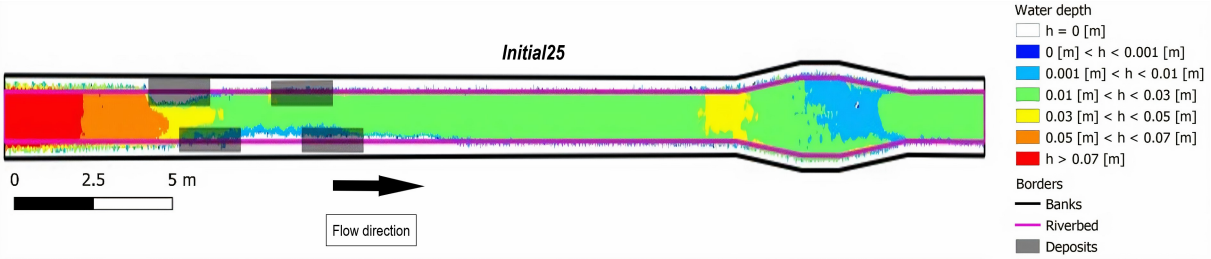

FIGURE B.14 – Water depths for *Initial25* scenario. The water depths correspond to the colour code shown. The transparent rectangles represent the initial deposit position. The boundary between the riverbed and the banks is shown as a purple line, while the boundary of the mesh is shown as a black line.

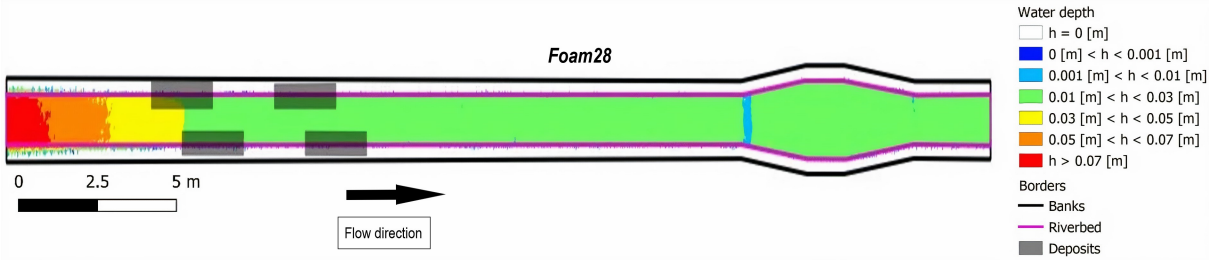

FIGURE B.15 – Water depths for *Foam28* scenario. The water depths correspond to the colour code shown. The transparent rectangles represent the initial deposit position. The boundary between the riverbed and the banks is shown as a purple line, while the boundary of the mesh is shown as a black line.

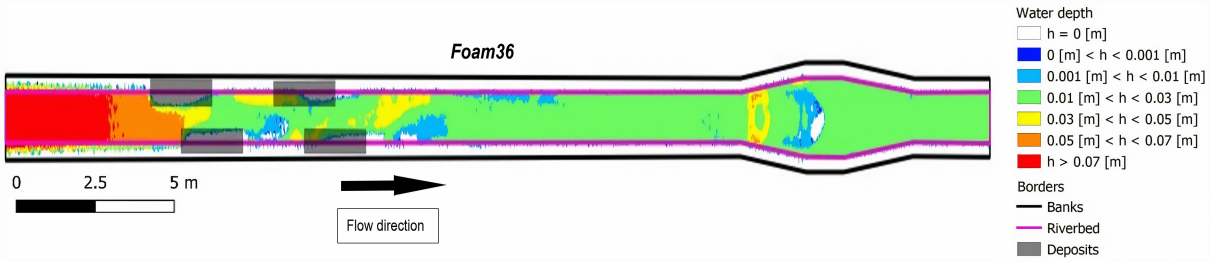

FIGURE B.16 – Water depths for *Foam36* scenario. The water depths correspond to the colour code shown. The transparent rectangles represent the initial deposit position. The boundary between the riverbed and the banks is shown as a purple line, while the boundary of the mesh is shown as a black line.

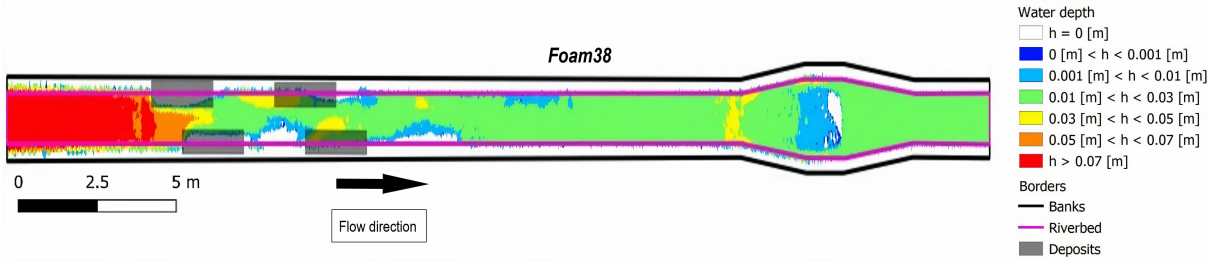

FIGURE B.17 – Water depths for *Foam38* scenario. The water depths correspond to the colour code shown. The transparent rectangles represent the initial deposit position. The boundary between the riverbed and the banks is shown as a purple line, while the boundary of the mesh is shown as a black line.

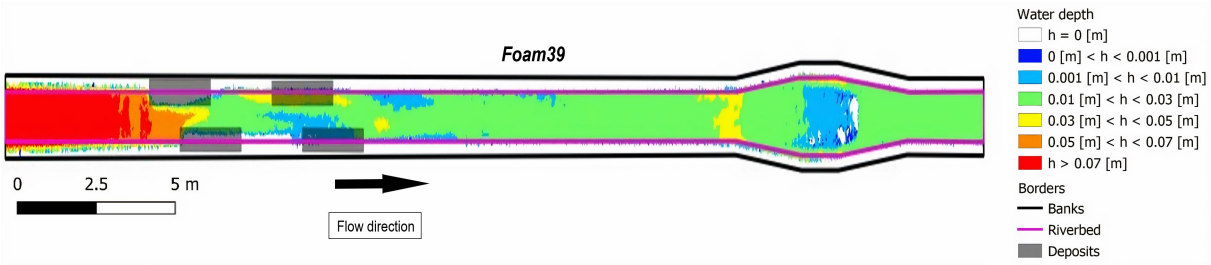

FIGURE B.18 – Water depths for *Foam39* scenario. The water depths correspond to the colour code shown. The transparent rectangles represent the initial deposit position. The boundary between the riverbed and the banks is shown as a purple line, while the boundary of the mesh is shown as a black line.

B.9 Particle size curve

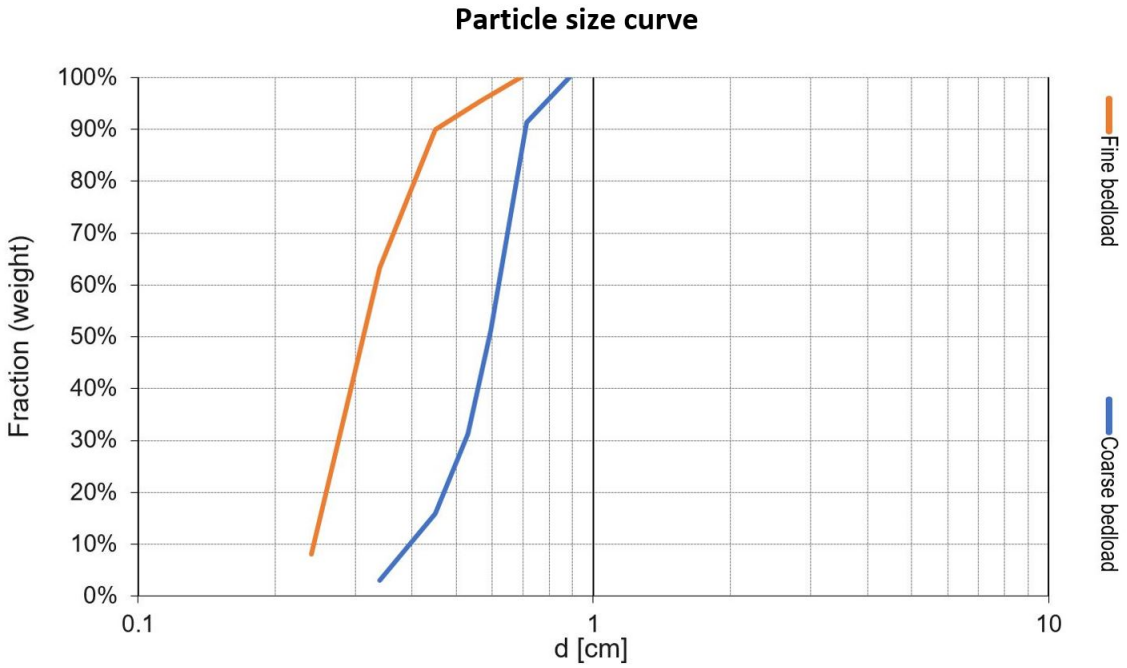

FIGURE B.19 – Particle size curve for fine (orange) and coarse (blue) bedload.

B.10 Shear stresses

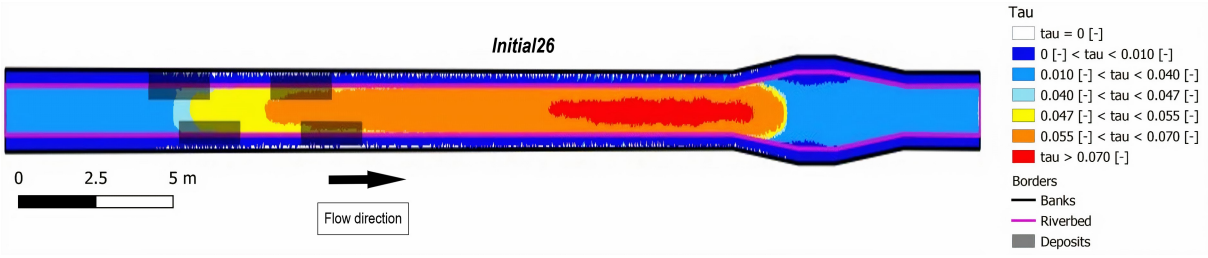

FIGURE B.20 – Shear stress for *Initial26* scenario considering a diameter d_m. The shear stresses correspond to the colour code shown. The transparent rectangles represent the initial deposit position. These rectangles are only shown to facilitate the interpretation of the results, as no sediment was added in the initial state. The boundary between the riverbed and the banks is shown as a purple line, while the boundary of the mesh is shown as a black line.

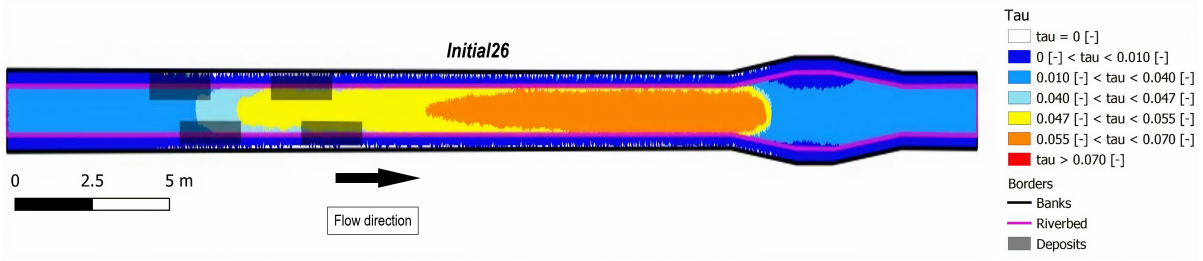

FIGURE B.21 – Shear stress for *Initial26* scenario considering a diameter d_{90}. The shear stresses correspond to the colour code shown. The transparent rectangles represent the initial deposit position. These rectangles are only shown to facilitate the interpretation of the results, as no sediment was added in the initial state. The boundary between the riverbed and the banks is shown as a purple line, while the boundary of the mesh is shown as a black line.

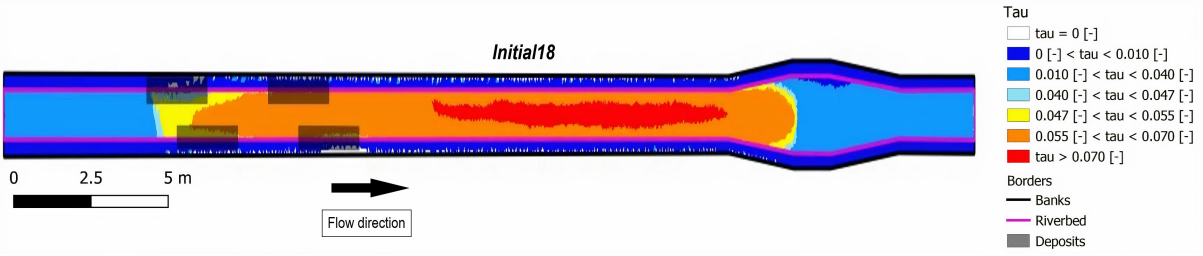

FIGURE B.22 – Shear stress for *Initial18* scenario considering a diameter d_m. The shear stresses correspond to the colour code shown. The transparent rectangles represent the initial deposit position. The boundary between the riverbed and the banks is shown as a purple line, while the boundary of the mesh is shown as a black line.

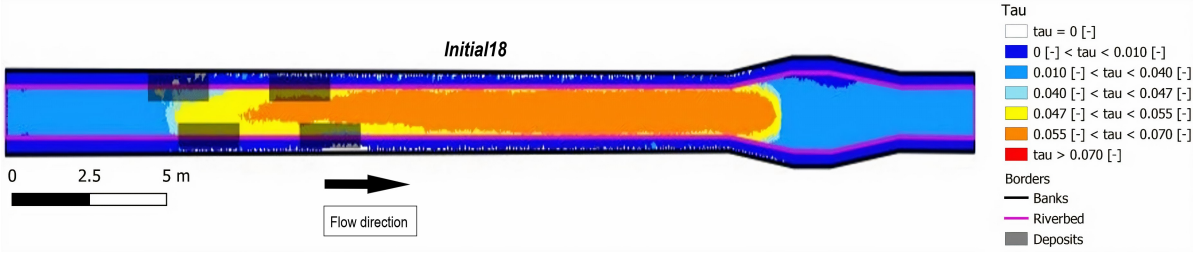

FIGURE B.23 – Shear stress for *Initial18* scenario considering a diameter d_{90}. The shear stresses correspond to the colour code shown. The transparent rectangles represent the initial deposit position. The boundary between the riverbed and the banks is shown as a purple line, while the boundary of the mesh is shown as a black line.

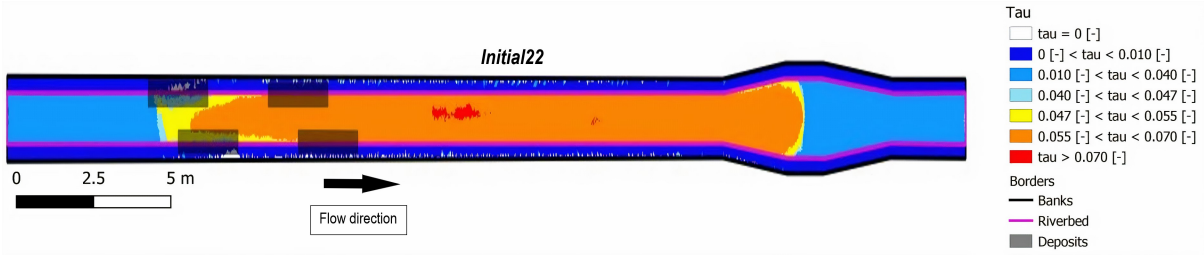

FIGURE B.24 – Shear stress for *Initial22* scenario considering a diameter d_m. The shear stresses correspond to the colour code shown. The transparent rectangles represent the initial deposit position. The boundary between the riverbed and the banks is shown as a purple line, while the boundary of the mesh is shown as a black line.

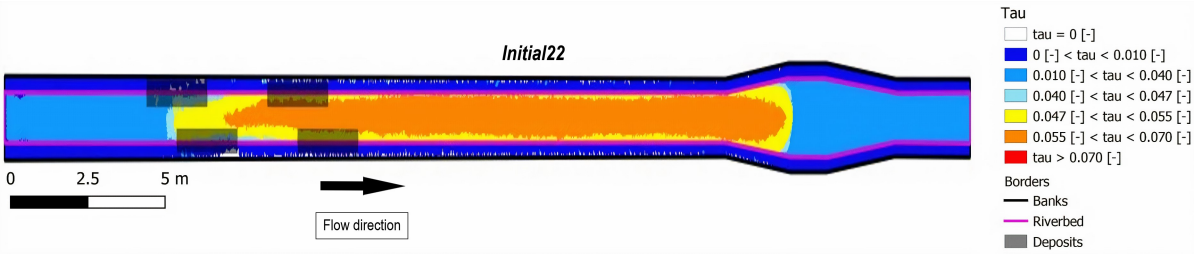

FIGURE B.25 – Shear stress for *Initial22* scenario considering a diameter d_{90}. The shear stresses correspond to the colour code shown. The transparent rectangles represent the initial deposit position. The boundary between the riverbed and the banks is shown as a purple line, while the boundary of the mesh is shown as a black line.

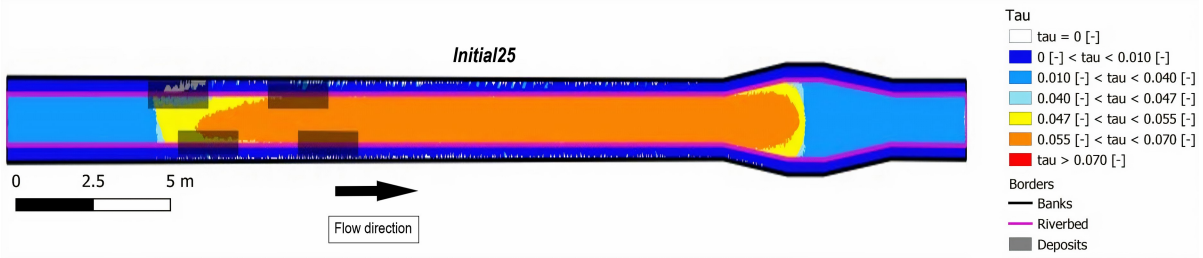

FIGURE B.26 – Shear stress for *Initial25* scenario considering a diameter d_m. The shear stresses correspond to the colour code shown. The transparent rectangles represent the initial deposit position. The boundary between the riverbed and the banks is shown as a purple line, while the boundary of the mesh is shown as a black line.

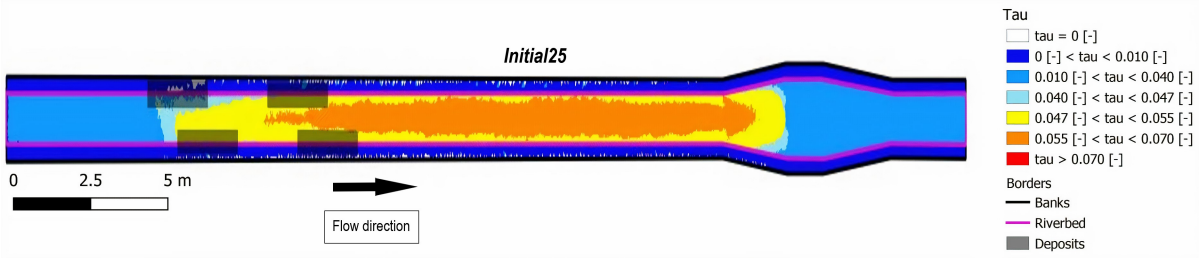

FIGURE B.27 – Shear stress for *Initial25* scenario considering a diameter d_{90}. The shear stresses correspond to the colour code shown. The transparent rectangles represent the initial deposit position. The boundary between the riverbed and the banks is shown as a purple line, while the boundary of the mesh is shown as a black line.

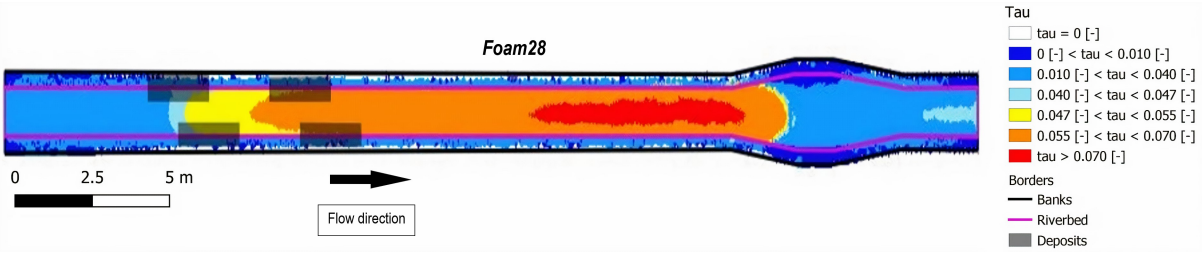

FIGURE B.28 – Shear stress for *Foam28* scenario considering a diameter d_m. The shear stresses correspond to the colour code shown. The transparent rectangles represent the initial deposit position. These rectangles are only shown to facilitate the interpretation of the results, as no sediment was added in the initial state. The boundary between the riverbed and the banks is shown as a purple line, while the boundary of the mesh is shown as a black line.

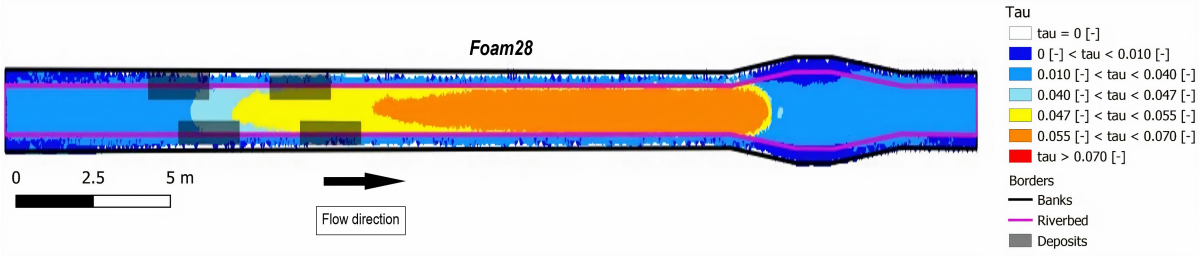

FIGURE B.29 – Shear stress for *Foam28* scenario considering a diameter d_{90}. The shear stresses correspond to the colour code shown. The transparent rectangles represent the initial deposit position. These rectangles are only shown to facilitate the interpretation of the results, as no sediment was added in the initial state. The boundary between the riverbed and the banks is shown as a purple line, while the boundary of the mesh is shown as a black line.

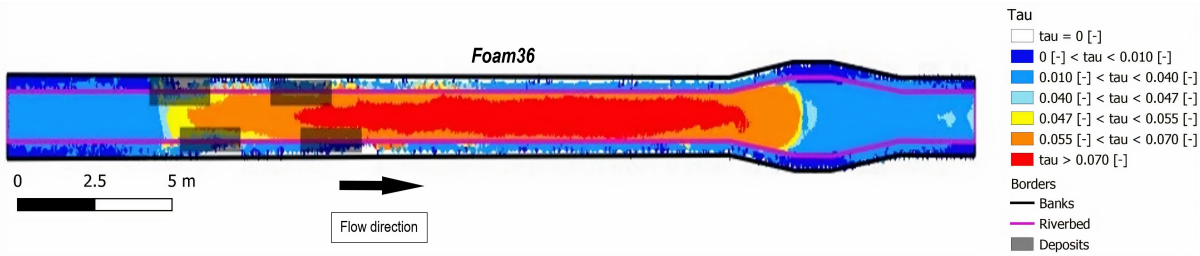

FIGURE B.30 – Shear stress for *Foam36* scenario considering a diameter d_m. The shear stresses correspond to the colour code shown. The transparent rectangles represent the initial deposit position. The boundary between the riverbed and the banks is shown as a purple line, while the boundary of the mesh is shown as a black line.

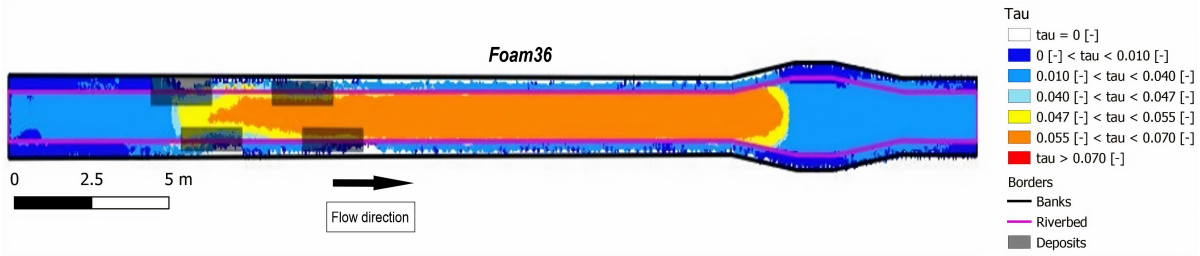

FIGURE B.31 – Shear stress for *Foam36* scenario considering a diameter d_{90}. The shear stresses correspond to the colour code shown. The transparent rectangles represent the initial deposit position. The boundary between the riverbed and the banks is shown as a purple line, while the boundary of the mesh is shown as a black line.

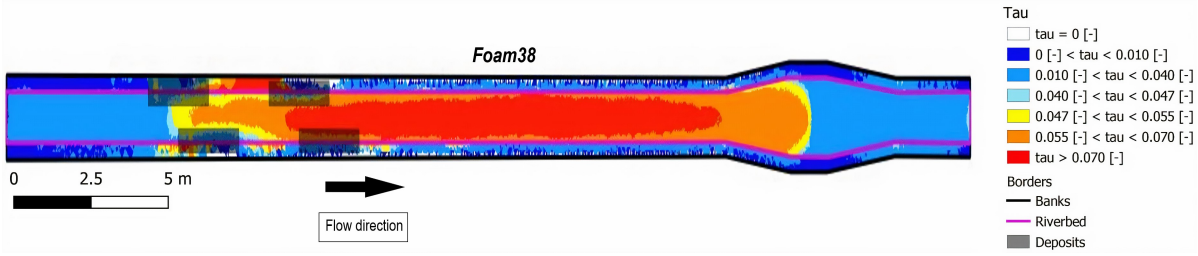

FIGURE B.32 – Shear stress for *Foam38* scenario considering a diameter d_m. The shear stresses correspond to the colour code shown. The transparent rectangles represent the initial deposit position. The boundary between the riverbed and the banks is shown as a purple line, while the boundary of the mesh is shown as a black line.

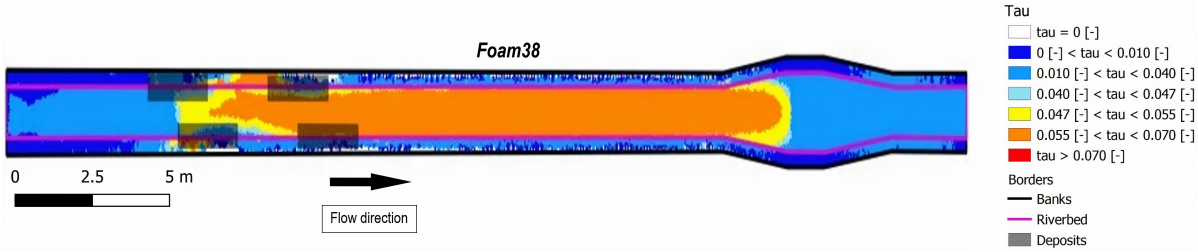

FIGURE B.33 – Shear stress for *Foam38* scenario considering a diameter d_{90}. The shear stresses correspond to the colour code shown. The transparent rectangles represent the initial deposit position. The boundary between the riverbed and the banks is shown as a purple line, while the boundary of the mesh is shown as a black line.

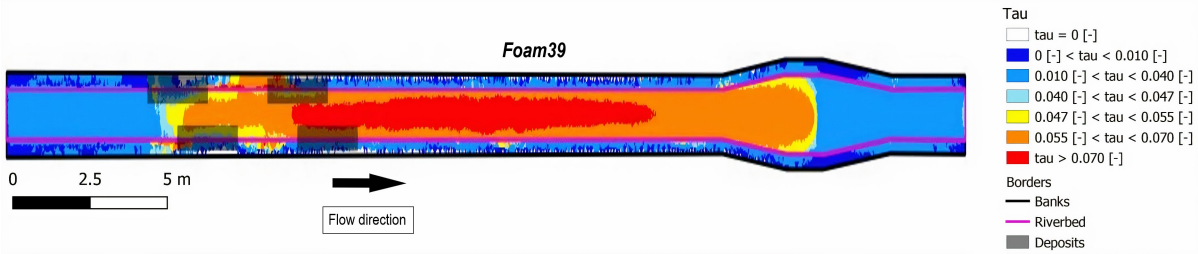

FIGURE B.34 – Shear stress for *Foam39* scenario considering a diameter d_m. The shear stresses correspond to the colour code shown. The transparent rectangles represent the initial deposit position. The boundary between the riverbed and the banks is shown as a purple line, while the boundary of the mesh is shown as a black line.

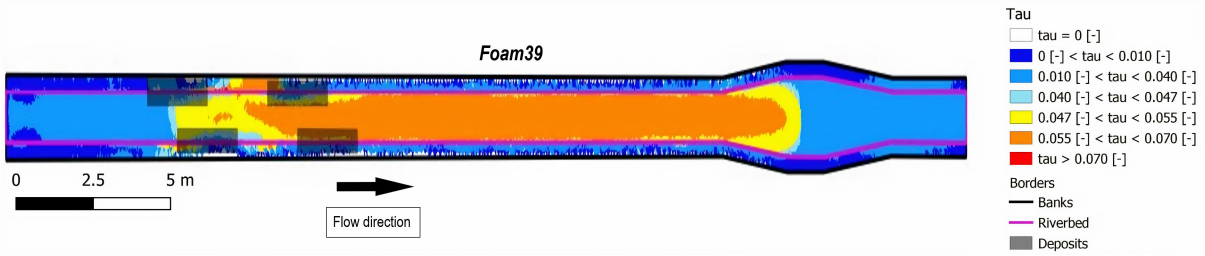

FIGURE B.35 – Shear stress for *Foam39* scenario considering a diameter d_{90}. The shear stresses correspond to the colour code shown. The transparent rectangles represent the initial deposit position. The boundary between the riverbed and the banks is shown as a purple line, while the boundary of the mesh is shown as a black line.

B.11 Velocity profiles - Flood flow

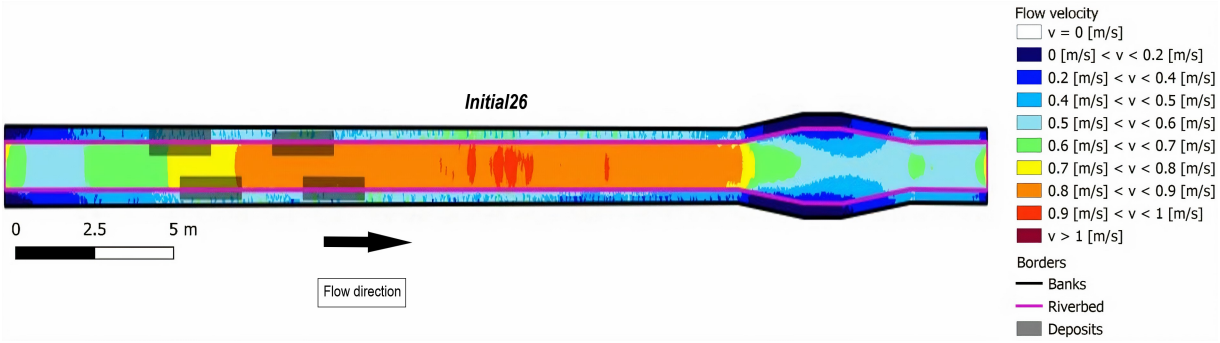

FIGURE B.36 – Velocities for *Initial26* scenario. The velocity values correspond to the colour code shown. The transparent rectangles represent the initial deposit position. These rectangles are only shown to facilitate the interpretation of the results, as no sediment was added in the initial state. The boundary between the riverbed and the banks is shown as a purple line, while the boundary of the mesh is shown as a black line.

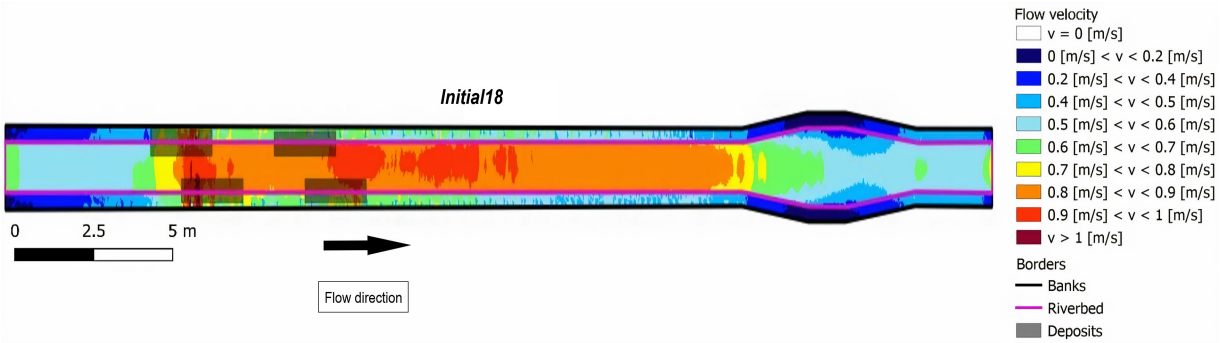

FIGURE B.37 – Velocities for *Initial18* scenario. The velocity values correspond to the colour code shown. The transparent rectangles represent the initial deposit position. The boundary between the riverbed and the banks is shown as a purple line, while the boundary of the mesh is shown as a black line.

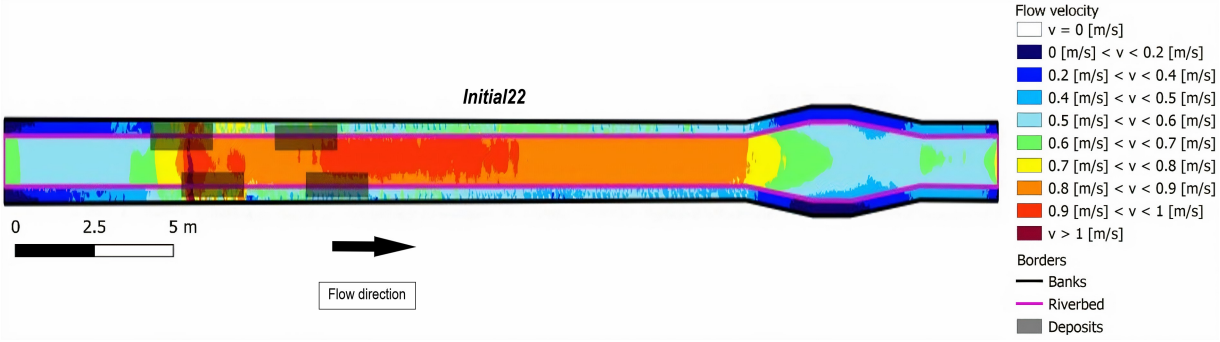

FIGURE B.38 – Velocities for *Initial22* scenario. The velocity values correspond to the colour code shown. The transparent rectangles represent the initial deposit position. The boundary between the riverbed and the banks is shown as a purple line, while the boundary of the mesh is shown as a black line.

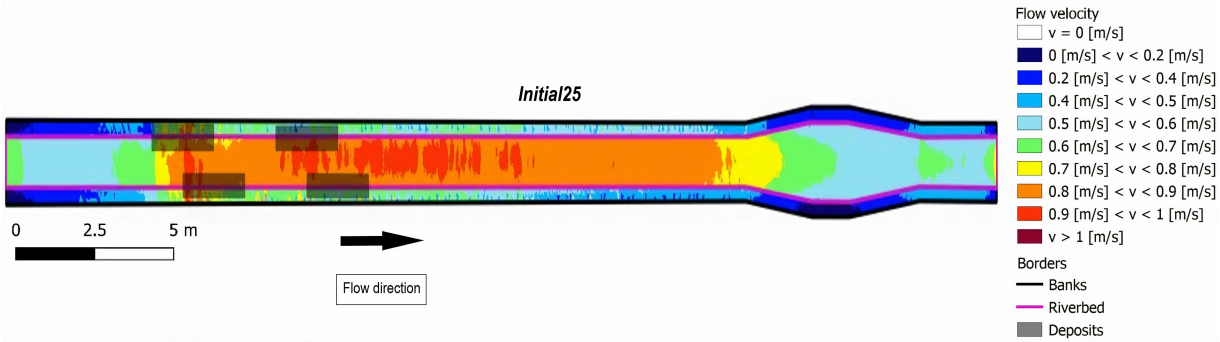

FIGURE B.39 – Velocities for *Initial25* scenario. The velocity values correspond to the colour code shown. The transparent rectangles represent the initial deposit position. The boundary between the riverbed and the banks is shown as a purple line, while the boundary of the mesh is shown as a black line.

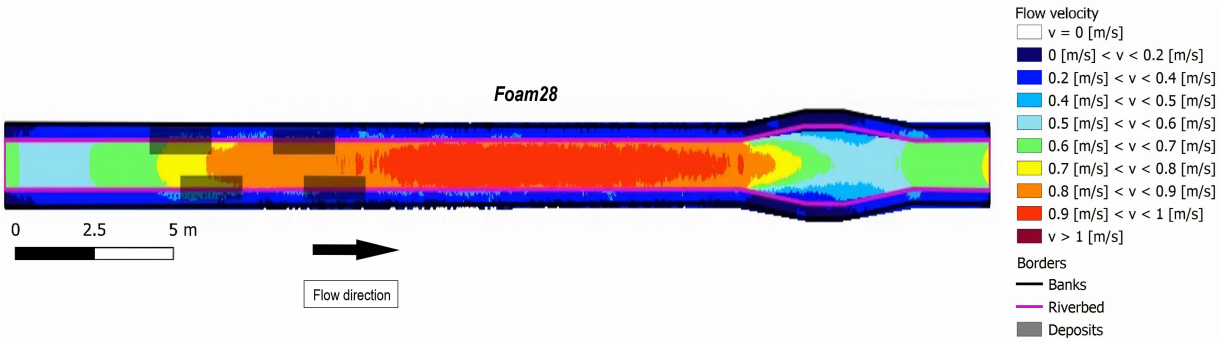

FIGURE B.40 – Velocities for *Foam28* scenario. The velocity values correspond to the colour code shown. The transparent rectangles represent the initial deposit position. These rectangles are only shown to facilitate the interpretation of the results, as no sediment was added in the initial state. The boundary between the riverbed and the banks is shown as a purple line, while the boundary of the mesh is shown as a black line.

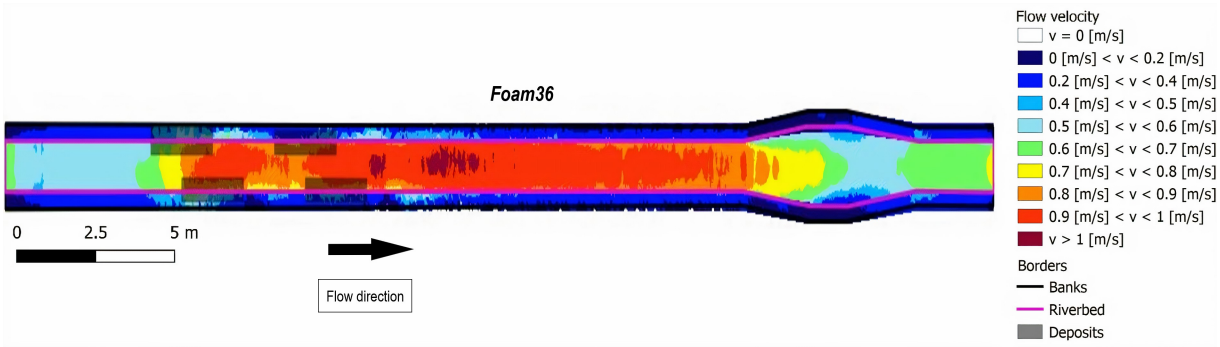

FIGURE B.41 – Velocities for *Foam36* scenario. The velocity values correspond to the colour code shown. The transparent rectangles represent the initial deposit position. The boundary between the riverbed and the banks is shown as a purple line, while the boundary of the mesh is shown as a black line.

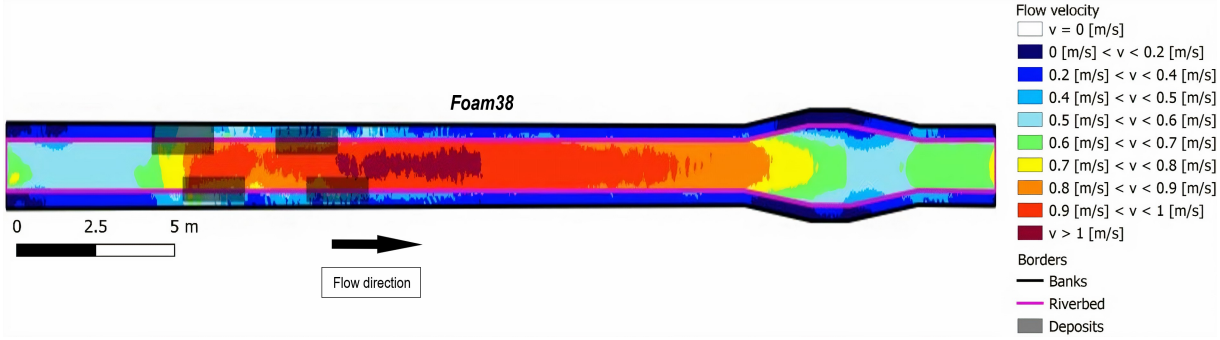

FIGURE B.42 – Velocities for *Foam38* scenario. The velocity values correspond to the colour code shown. The transparent rectangles represent the initial deposit position. The boundary between the riverbed and the banks is shown as a purple line, while the boundary of the mesh is shown as a black line.

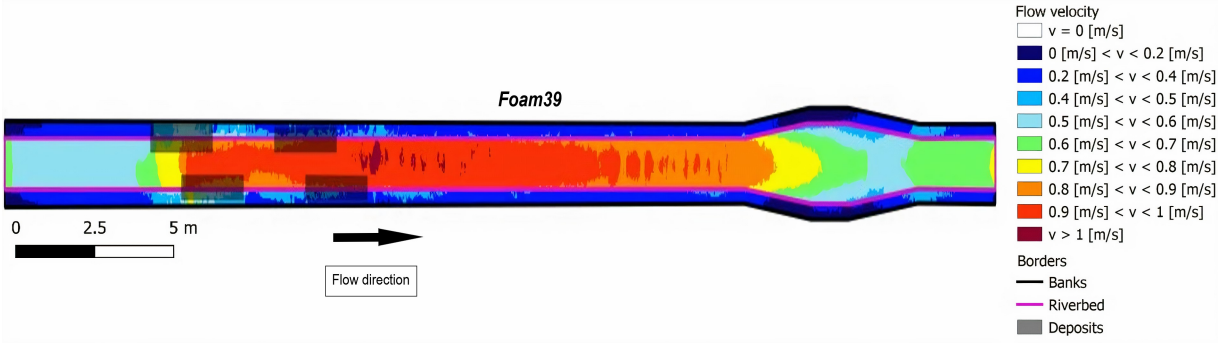

FIGURE B.43 – Velocities for *Foam39* scenario. The velocity values correspond to the colour code shown. The transparent rectangles represent the initial deposit position. The boundary between the riverbed and the banks is shown as a purple line, while the boundary of the mesh is shown as a black line.

B.12 Water height profiles - Flood flow

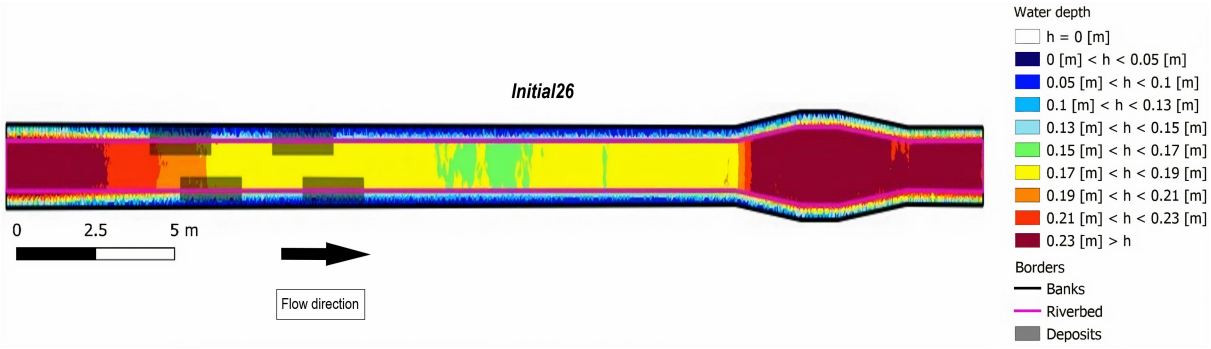

FIGURE B.44 – Water heights for *Initial26* scenario. The water depths correspond to the colour code shown. The transparent rectangles represent the initial deposit position. These rectangles are only shown to facilitate the interpretation of the results, as no sediment was added in the initial state. The boundary between the riverbed and the banks is shown as a purple line, while the boundary of the mesh is shown as a black line.

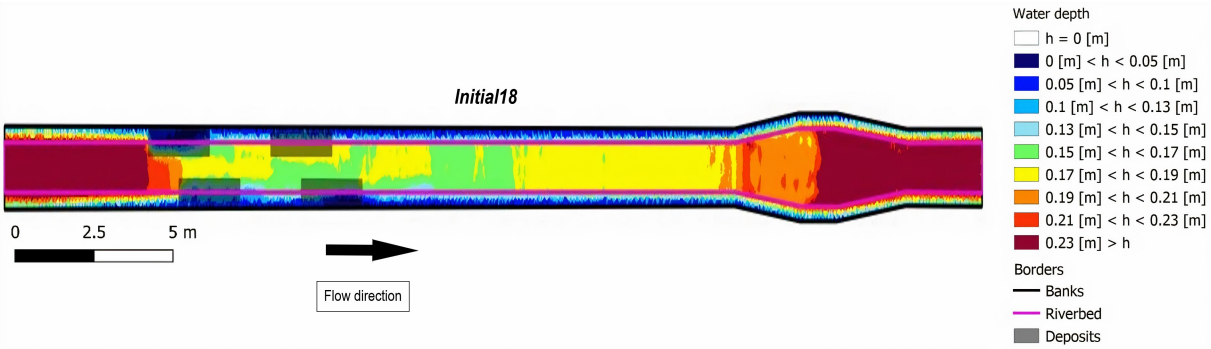

FIGURE B.45 – Water heights for *Initial18* scenario. The water depths correspond to the colour code shown. The transparent rectangles represent the initial deposit position. The boundary between the riverbed and the banks is shown as a purple line, while the boundary of the mesh is shown as a black line.

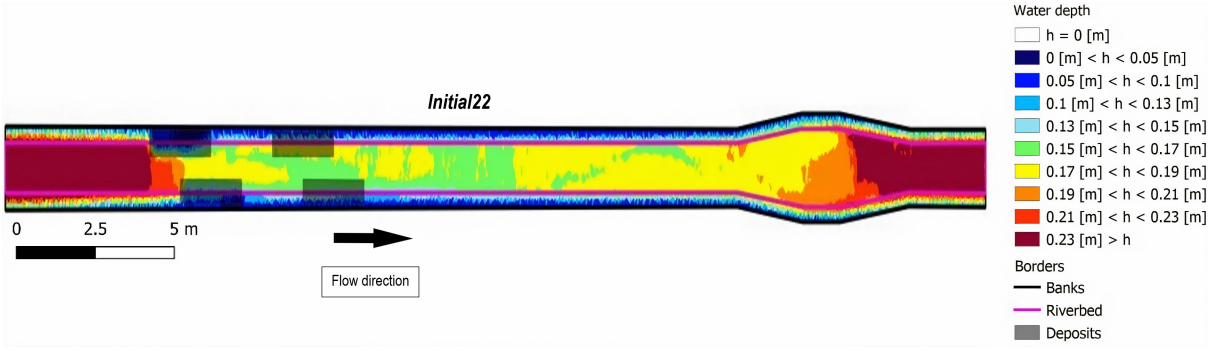

FIGURE B.46 – Water heights for *Initial22* scenario. The water depths correspond to the colour code shown. The transparent rectangles represent the initial deposit position. The boundary between the riverbed and the banks is shown as a purple line, while the boundary of the mesh is shown as a black line.

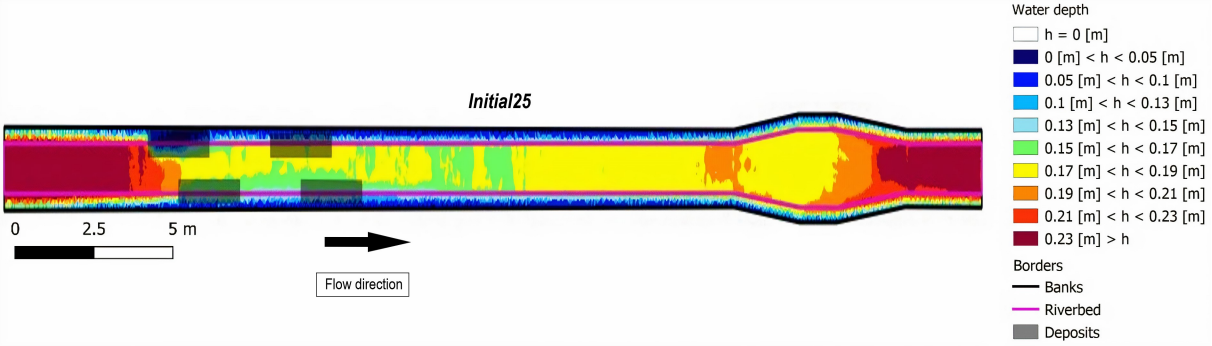

FIGURE B.47 – Water heights for *Initial25* scenario. The water depths correspond to the colour code shown. The transparent rectangles represent the initial deposit position. The boundary between the riverbed and the banks is shown as a purple line, while the boundary of the mesh is shown as a black line.

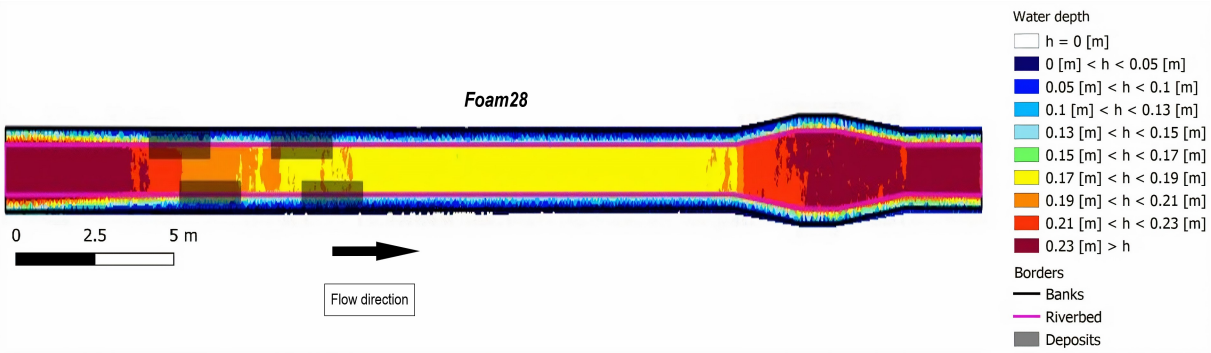

FIGURE B.48 – Water heights for *Foam28* scenario. The water depths correspond to the colour code shown. The transparent rectangles represent the initial deposit position. These rectangles are only shown to facilitate the interpretation of the results, as no sediment was added in the initial state. The boundary between the riverbed and the banks is shown as a purple line, while the boundary of the mesh is shown as a black line.

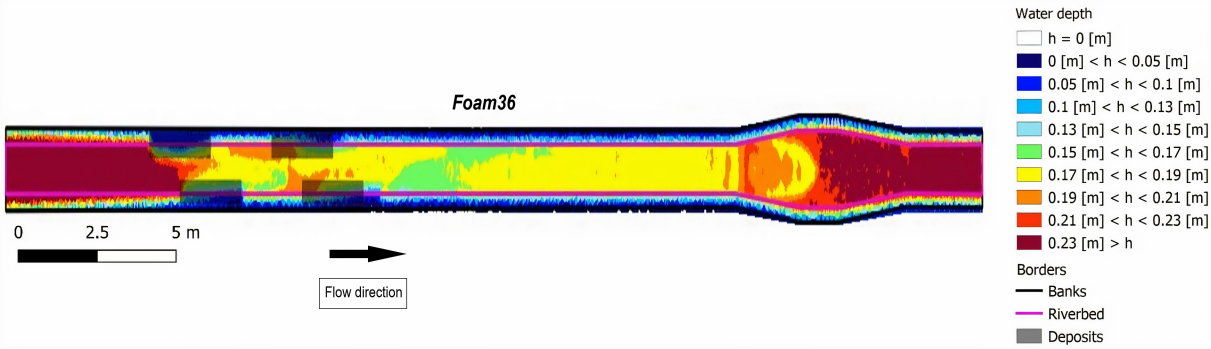

FIGURE B.49 – Water heights for *Foam36* scenario. The water depths correspond to the colour code shown. The transparent rectangles represent the initial deposit position. The boundary between the riverbed and the banks is shown as a purple line, while the boundary of the mesh is shown as a black line.

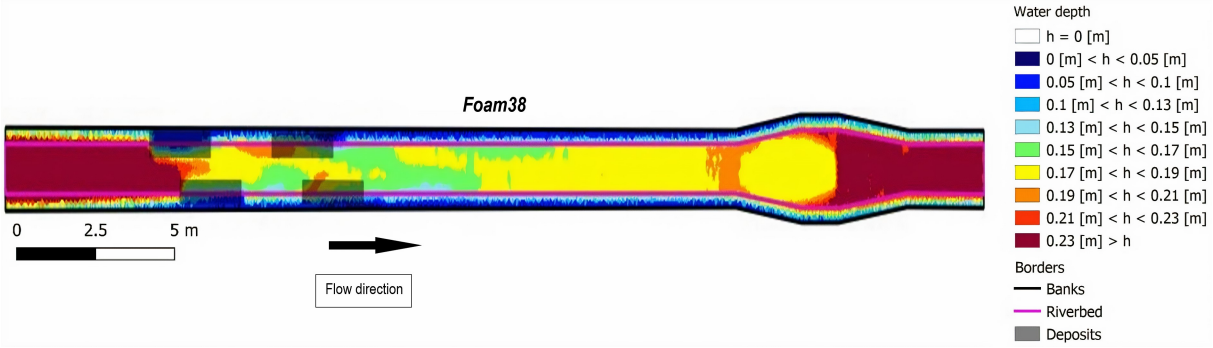

FIGURE B.50 – Water heights for *Foam38* scenario. The water depths correspond to the colour code shown. The transparent rectangles represent the initial deposit position. The boundary between the riverbed and the banks is shown as a purple line, while the boundary of the mesh is shown as a black line.

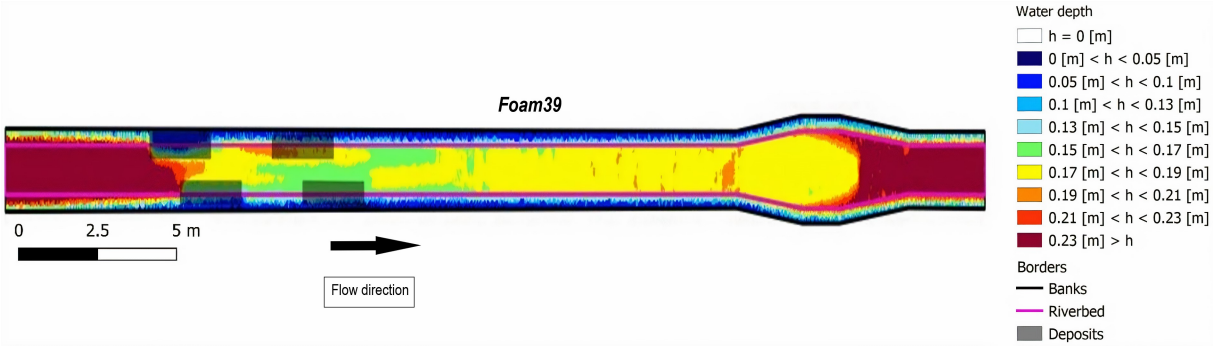

FIGURE B.51 – Water heights for *Foam39* scenario. The water depths correspond to the colour code shown. The transparent rectangles represent the initial deposit position. The boundary between the riverbed and the banks is shown as a purple line, while the boundary of the mesh is shown as a black line.